11-9-2020

A Study of 26Al(p, γ)27Si with the Silicon Array for Branching Ratio Experiments (SABRE)

Erin Courtney Good
Louisiana State University and Agricultural and Mechanical College

A STUDY OF ^{26}Al$(p,\gamma)^{27}$Si WITH THE SILICON ARRAY FOR BRANCHING RATIO EXPERIMENTS (SABRE)

A Dissertation

Submitted to the Graduate Faculty of the
Louisiana State University and
Agricultural and Mechanical College
in partial fulfillment of the
requirements for the degree of
Doctor of Philosophy

in

The Department of Physics & Astronomy

by
Erin Courtney Good
B.S. Physics and B.A. Music, University of Richmond, 2013
December 2020

In memory of Con Beausang, whose passion for teaching and mentorship inspired me to continue studying nuclear physics.

Acknowledgments

First, I must thank my preferred head of state the Queen for being an inspiration to us all (particularly anyone who ever entered my office), and Alexandra Elbakyan, for making scientific literature accessible to everyone.

On the science side, I have to thank all the great people at FSU that helped put together and run the experiment, including Lagy, Powell, Greg, Dave, Ingo, Jason, and Rick. Additionally, I owe a blood debt to the grad students who sat shifts for the experiment's many runs. At FSU, this was Caleb, Chris, Nate, Ken, Ashton, Jesus, Liz, Ben, Eilens, and Eli, while at LSU I have to thank Khang, Rachel, Thomas, Keilah, Ashley, and Alex for the support on the runs. Extra blood debt goes to Gordon for being so helpful and prompt with the eventbuilder code when I had issues, our postdoc Kevin for running the last March experiment when COVID struck and we were trapped in Louisiana, and Sudarsan for going on EVERY SINGLE TRIP TO FSU with me and being a great travel buddy.

At LSU, the fantastic front office staff, particularly Carol, Mimi, Shemeka, Claire, and Paige, were super helpful when I needed anything and a pleasure to talk to. The electronics shop staff, Marcus and the late Brad, as well as the machine shop staff, Vince and Brandon, were absolutely indispensable to the success of the SABRE project.

Many thanks to my committee members, Drs Sheehy, Launey, and Zeitlin for agreeing to read this document and sit through almost an hour of me talking. Many thanks are also owed to my pretend advisors Scott and Jeff for advising me on the many questions I had during my extensive time at LSU. But I couldn't have done this without the sage advice and wisdom of my actual advisor, Catherine, to whom I will be forever grateful for being such a great advisor and wonderful person (and also for reading the draft of this document about 5,000 times).

To all my fellow grad students who I pestered with conversation and dumb puns, thanks for putting up with me (in particular Robert and Grigor because I practically lived in their office pre-COVID, and Graeme who I got to bother without even leaving my desk). To Kelsie for always being down to avoid work by going to get bubble tea every single day. To my fabulous roommates

Karunya and Alexandra during this rough past year, and Rachel and Mrs. Darbs the years before this one, who provided me with bunny paraphernalia and and were always down for snack trips to de-stress. To Ali, who has been a huge support to me during this horrible COVID summer and before with prime tiktoks, OWM stories, and bread-baking tips. To Terra, my homework and gym buddy for this entire time (and fellow professional boat captain), for sending daily cat/plant videos, snarky comments, and monochrome fashion advice my way whether solicited or not.

And to my family, Brian, Deb, Hannah, and Barkley, for always believing in me and being proud, even though none of them have any idea what I'm doing. They're just Good like that.

Table of Contents

Abstract

The observation of the radioisotope ^{26}Al is an indicator of ongoing nucleosynthesis in the Galaxy due to its short lifetime ($t_{1/2} = 7.2 \times 10^5$ yr) on Galactic timescales. It is thought to be synthesized in several different environments in our Galaxy, one of which is in classical novae. Classical novae are stellar explosions that occur on the surface of a white dwarf in a binary system with a main sequence star. The isotopic production resulting from the nucleosynthesis that drives these explosions can be modeled with the input of nuclear reaction rates. In recent years, many of the reactions of importance to classical novae have been directly measured; one of the exceptions to this is the $^{26}\mathrm{Al}^m(p,\gamma)^{27}\mathrm{Si}$ reaction, which is one of the primary destruction mechanisms for ^{26}Al in novae. Because this reaction cannot be directly measured with radioactive ion beam intensities currently available, indirect experimental techniques are required. Here one such technique is discussed, including the installation and commissioning of the Silicon Array for Branching Ratio Experiments (SABRE), that is a vital part of the detector systems of the Super Enge Split-Pole Spectrograph (SE-SPS) at Florida State University. One of the first science runs conducted on this new experimental apparatus was the $^{27}\mathrm{Al}(^3\mathrm{He},t)^{27}\mathrm{Si}^*(p)^{26}\mathrm{Al}^{g,m}$ reaction, which was used to measure the proton branching ratios of states in ^{27}Si of interest to the $^{26}\mathrm{Al}^{g,m}(p,\gamma)^{27}\mathrm{Si}$ reactions. SABRE was able to detect proton decay branching ratios from resonance energies 200-400 keV lower than previously measured. This thesis will discuss this measurement and the commissioning of SABRE, which performs as expected. This will be followed by a discussion of the measurement of the branching ratios to the isomer state, the calculation of the $^{26}\mathrm{Al}^m(p,\gamma)^{27}\mathrm{Si}$ reaction rate based on the results, and the effects this rate has on the synthesis of ^{26}Al in classical novae.

1 Motivation

At the inception of the Universe, the Big Bang occurred and all matter was extremely hot and dense. Within the first twenty minutes, after the quarks had cooled and combined into the very first protons and neutrons, primordial nucleosynthesis created elements up to atomic mass seven. This resulted in a very large amount of hydrogen (specifically ^{1}H), about twenty-five percent ^{4}He and much smaller amounts of beryllium, lithium, and other hydrogen and helium isotopes. Approximately 100 million years later, the first stars formed and the rest of the elements began to be created in different stellar processes.

There are a wide variety of stellar phenomena where nucleosynthesis occurs throughout our Universe; however, some sites are better understood than others. For example, we have a good understanding of the nuclear processes transpiring in main sequence stars of varying masses, especially those like our sun, but these processes are often more difficult to discern in more complex stellar environments such as interacting binary systems, where two stellar objects are orbiting and interacting with each other. When one of the objects in a binary fills its Roche lobe (the surface of gravitational equilibrium between the two objects) and starts spilling mass onto the other as a donor, the activity on the surface of the mass-accreting partner star can become an epicenter of interesting nucleosynthesis leading to the creation of heavier elements.

Classical novae occur in binary systems of a typically main sequence star and a white dwarf. Main sequence stars are in the same stage of evolution as our sun, in which they burn hydrogen, helium, and then heavier elements depending on their intial mass [1]. White dwarfs are the final products of the stellar evolution of stars less than ten solar masses; they too were once main sequence stars. After a star leaves the main sequence, it becomes a red giant before it begins to burn its helium, resulting in a core of helium surrounded by a hydrogen shell burning via the Carbon-Nitrogen-Oxygen (CNO) cycle, shown in Fig. 1.1. The red giant's initial mass determines the elemental contents of the future white dwarf as higher mass stars can produce heavier elements. Lower mass stars fuse helium to create carbon and oxygen, but their temperatures are too low to sustain carbon burning, resulting in a carbon-oxygen core (leading to a CO white dwarf). Con-

versely, higher mass red giants (still below ten solar masses) are able to achieve carbon-burning temperatures but not neon-burning temperatures, resulting in residual neon and magnesium in the core as well as oxygen (leading to ONe white dwarfs). As it burns heavier and heavier elements, the red giant expands, the core gets hotter, and the star gets larger and more luminous. The star is then called an asymptotic giant branch star, which burns hotter but loses mass quickly in stellar winds that develop. The stellar winds gradually remove the outer layers of the star to expose the core, leaving the core of heavier elements after the outer layers are blown off. As the last nuclear burning occurs in the star, it creates a high temperature that ionizes the removed shell of the star to create a planetary nebula. After this expulsion of outer material, only the compact internal core remains, its mass supported only by electron degeneracy pressure as it is no longer fusing material and thus has no internal energy source. The star has then become a white dwarf: a very compact object with a mass up to 1.4 solar masses (the Chandrasekhar limit) and a radius comparable to that of the Earth.

Prior to a classical nova, the white dwarf accretes mass (consisting primarily of hydrogen) from the main sequence star. Accretion onto the white dwarf's surface, and the subsequent rise in the temperature, leads to thermonuclear runaway, which drives the nova explosion. The white dwarf in this binary system has an accretion rate of $10^{-10} - 10^{-9} M_{\odot}/\mathrm{yr}$ ($M_{\odot}$ being one solar mass) and peak outburst temperatures on the order of 10^8 K; the explosion itself ejects roughly $10^{-4} - 10^{-5} M_{\odot}$, which is how some of the elements in the Universe are created and dispersed [3]. This outburst lasts anywhere from several days to years, with more intense outbursts being shorter in duration. In contrast to other violent explosions like supernovae, classical novae's binary systems survive intact and continue accreting mass after the outburst. It is suspected that most or all novae are recurrent on timescales too long to be observed (thousands to hundreds of thousands of years); however, there are some rare recurrent novae that have been observed with shorter recurrence timescales of decades [4].

Thermonuclear runaway is where the nuclear processes of interest occur. Reactions in novae are thought to create proton-rich nuclei up to mass 40, or calcium, via reaction networks like those

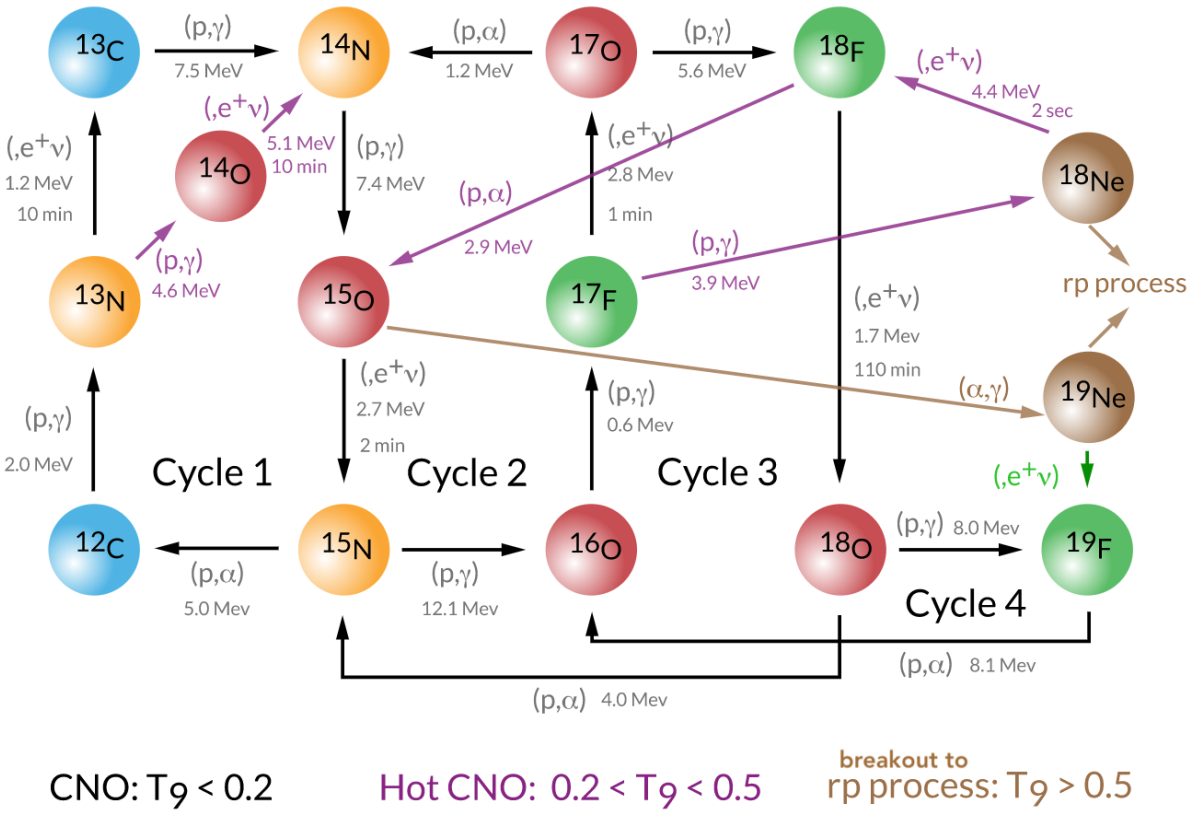

Figure 1.1. A diagram showing the different types of CNO cycles, the temperatures at which they occur, and the reactions involved [2]. The colors of the nuclei correspond to the different elements involved; for example, all oxygen isotopes in the diagram are red. Notice that the hot CNO cycle produces neon isotopes, which requires hotter temperatures. The rp-process (rapid proton capture) shown on the left side of the chart occurs during hydrogen-rich explosive nucleosynthesis and does not occur during the stable burning of a main-sequence star. This is the cycle a red giant star, the progenitor to a white dwarf, undergoes to create heavier elements in its core.

shown in Figs. 1.2 or 1.3 [3]. However, the type of white dwarf participating in the nova greatly impacts the different isotopes it is able to synthesize during the outburst. As mass builds up on the white dwarf, ONe dwarfs are found to sustain larger envelopes than CO white dwarfs due to less ^{12}C content in the envelope when thermonuclear runaway occurs. Thus, ONe novae are able to sustain larger masses, which creates higher burning temperatures ($T_9 = 0.1 - 0.4$ GK) and more violent explosions [5]. Because of these higher temperatures, ONe novae are the novae which produce heavier elements up to mass 40. For example, ^{26}Al, the subject of this thesis, is produced only in ONe novae (see Fig. 1.2). Additionally, the synthesis of elements from silicon to calcium

is restricted to ONe novae as well [5].

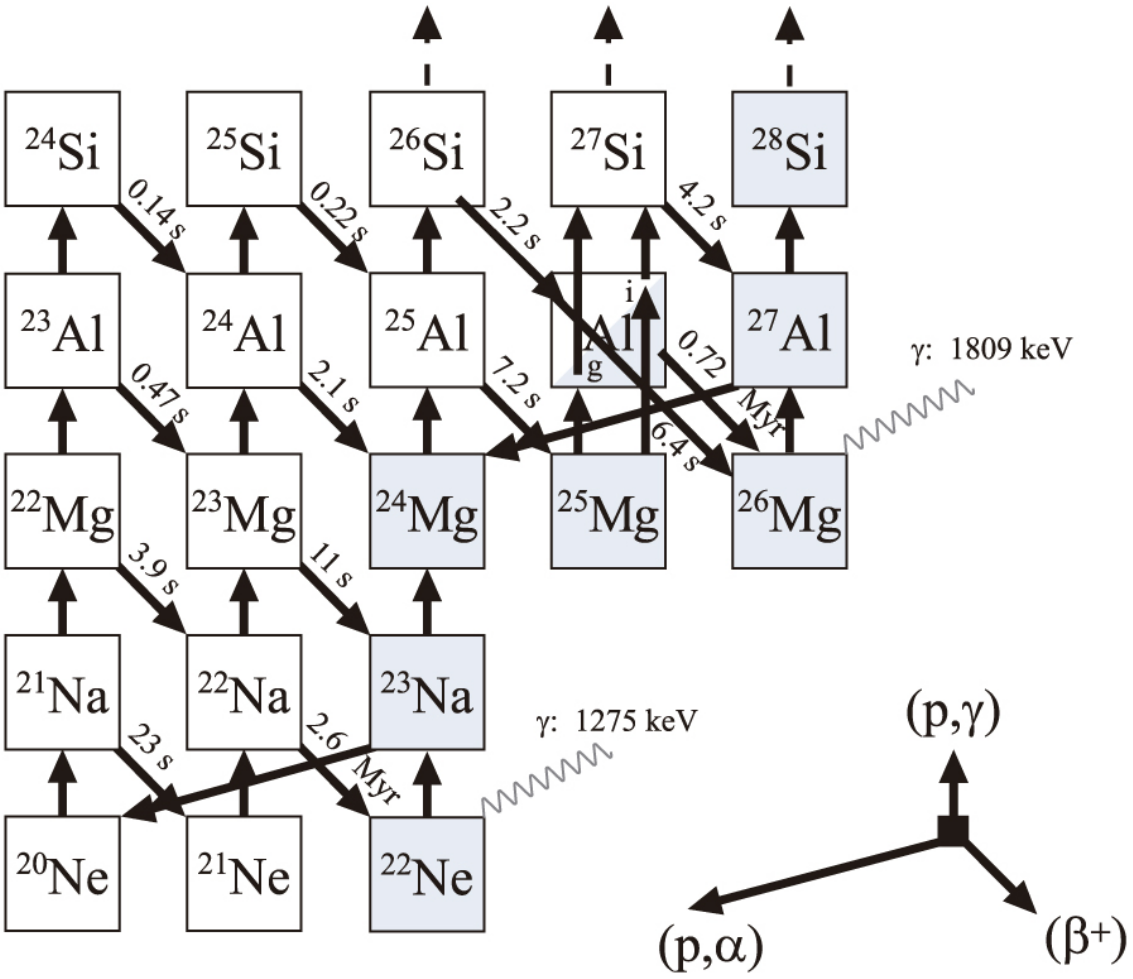

Figure 1.2. A portion of the chart of the nuclides illustrating the nuclear reactions in the neon and aluminum regions that occur in nova nucleosynthesis, reproduced from [6]. The half-life of each β^+ decay is labeled, as well as the 1.809-MeV gamma ray emitted in the MgAl cycle observed via space-based telescopes. While the 1.275-MeV gamma ray from the decay of ^{22}Na is also included here, it has yet to be observed in any space-based missions. Isotopes shaded grey are stable.

Nucleosynthesis in both CO and ONe novae proceeds up the nuclear chart primarily through a series of (p, γ) reactions followed by β^+ decays back to stability, as shown in Figs. 1.2 and 1.3. These reactions also compete against the (p, α) reactions that can occur, which close specific reaction cycles in the nuclear chart and eventually halt the nuclear network entirely at masses

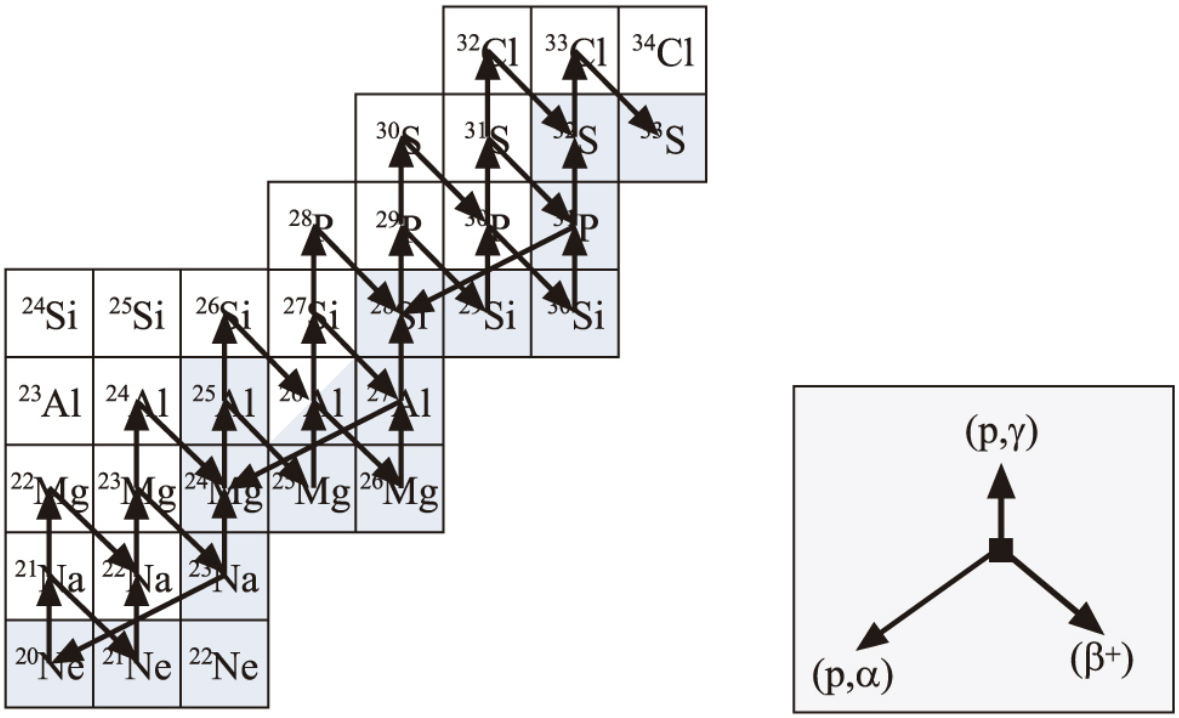

Figure 1.3. A portion of the chart of the nuclides illustrating a subset of nuclear reactions that occur in ONe novae to create heavier elements, reproduced from [6]. Similarly to Fig. 1.2, isotopes shaded grey are stable.

around $A = 40$.

While we are reasonably confident of which nuclear reactions occur in novae, the final abundances of nuclei created in novae are not fully understood due to the lack of concrete knowledge of some of the reaction rates needed to accurately model the processes occurring during thermonuclear runaway. By performing sensitivity studies on nuclear network models that currently exist, one can determine which reaction rates affect the final isotope yields the most when varied within their experimental or theoretical uncertainties, thus determining which reaction rates are the highest priority for experimentalists to measure. By solidifying the rate of the nuclear reactions that occur in classical novae through experimental measurements, these events can be better modeled and understood.

1.1 Sensitivity Studies for Classical Nova Nucleosynthesis

Sensitivity studies are an important component of nuclear astrophysics research as they guide experimentalists to study particular reactions. By modeling a classical nova's thermodynamic and nuclear processes, a relatively accurate picture of a nova's final nuclear abundances and energy generation during its explosion can be determined, which can be compared with astrophysical observations as a way of checking the model's accuracy. In a sensitivity study, the nuclear reactions that go into the model are individually varied within current experimental or theoretical uncertainties. By comparing changes in the final abundances or energy produced, one can pinpoint which reactions cause the largest changes in these outputs, and therefore are of the highest priority to be measured.

A study by Iliadis *et al.* from 2002 [7] is the most recent complete sensitivity study on reactions important to nova nucleosynthesis. In this study, reaction rates were varied within their uncertainties to determine which reactions were most influential in the nuclear network; a table of results showing the impact on various isotopic abundances is given in Fig. 1.4. One of these reactions with a rate that has not yet been measured is the $^{26}\mathrm{Al}^{m}(p,\gamma)^{27}\mathrm{Si}$ reaction. Because of its relation to the production of ^{26}Al, it is interesting for a number of reasons discussed in later sections.

1.2 ^{26}Al Production in Classical Novae

The isotope ^{26}Al is somewhat unique because it is a nucleus with two long-lived states: an isomeric state at 228 keV in addition to the ground state, as seen in Fig. 1.5. The ground state and isomer of ^{26}Al (denoted by $^{26}\mathrm{Al}^{\mathrm{g}}$ and $^{26}\mathrm{Al}^{m}$, respectively) have very different properties, and as such the isomer often must be treated as a separate isotope. The isomer has a spin-parity of 0^+ while the ground state's spin-parity is 5^+, and this large distance in spins means the states are extremely unlikely to interact directly through electromagnetic transitions (this holds true for nova temperatures, although at high temperatures, $T_9 > 0.4$ GK, they can communicate via thermal excitations of higher lying states). Additionally, the isomer has a half-life of 6.63 seconds while the ground state's half-life is $7.2x10^5$ years. Lastly, as seen in Fig. 1.5, the ground state decays through the first-excited state of ^{26}Mg, which decays via emission of a 1.809-MeV gamma ray,

INFLUENCE OF REACTION-RATE VARIATIONS ON ISOTOPIC ABUNDANCES IN NOVA NUCLEOSYNTHESIS[a]

Reaction-Rate Variation[b]	Isotopic Abundance Change[c]
CO Nova Models	
$^{17}O(p,\gamma)^{18}F$.....	^{18}F
$^{17}O(p,\alpha)^{14}N$.....	^{17}O, ^{18}F
$^{18}F(p,\alpha)^{15}O$	^{18}F
$^{22}Ne(p,\gamma)^{23}Na$	^{22}Ne, ^{23}Na, ^{24}Mg, ^{25}Mg, ^{26}Al
$^{23}Na(p,\gamma)^{24}Mg$.....	^{24}Mg
$^{26}Mg(p,\gamma)^{27}Al$.....	^{26}Mg
$^{26}Al^{g}(p,\gamma)^{27}Si$.....	^{26}Al
ONe Nova Models	
$^{17}O(p,\gamma)^{18}F$.....	^{17}O, ^{18}F
$^{17}O(p,\alpha)^{14}N$.....	^{17}O, ^{18}F
$^{17}F(p,\gamma)^{18}Ne$.....	^{17}O, ^{18}F
$^{18}F(p,\alpha)^{15}O$	^{16}O, ^{17}O, ^{18}F
$^{21}Na(p,\gamma)^{22}Mg$.....	^{21}Ne, ^{22}Na, ^{22}Ne
$^{22}Ne(p,\gamma)^{23}Na$	^{22}Ne
$^{23}Na(p,\gamma)^{24}Mg$.....	^{20}Ne, ^{21}Ne, ^{22}Na, ^{23}Na, ^{24}Mg, ^{25}Mg, ^{26}Mg, ^{26}Al, ^{27}Al
$^{23}Mg(p,\gamma)^{24}Al$.....	^{20}Ne, ^{21}Ne, ^{22}Na, ^{23}Na, ^{24}Mg
$^{26}Mg(p,\gamma)^{27}Al$.....	^{26}Mg
$^{26}Al^{g}(p,\gamma)^{27}Si$.....	^{26}Al
$^{26}Al^{m}(p,\gamma)^{27}Si$.....	^{26}Mg
$^{29}Si(p,\gamma)^{30}P$.....	^{29}Si
$^{30}P(p,\gamma)^{31}S$.....	^{30}Si, ^{32}S, ^{33}S, ^{34}S, ^{35}Cl, ^{37}Cl, ^{36}Ar, ^{37}Ar, ^{38}Ar
$^{33}S(p,\gamma)^{34}Cl$	^{33}S, ^{34}S, ^{35}Cl, ^{36}Ar
$^{33}Cl(p,\gamma)^{34}Ar$	^{33}S
$^{34}S(p,\gamma)^{35}Cl$	^{34}S, ^{35}Cl, ^{36}Ar
$^{34}Cl(p,\gamma)^{35}Ar$	^{34}S
$^{37}Ar(p,\gamma)^{38}K$.....	^{37}Cl, ^{37}Ar, ^{38}Ar
$^{38}K(p,\gamma)^{39}Ca$	^{38}Ar

Figure 1.4. Reaction rates that impact various isotopic abundances, reproduced from [7]. [a]The table provides only a qualitative overview for some of their results. [b]Only those reactions are listed that have a significant influence on isotopic abundances in at least one of the nova models considered in this work. [c]Only those isotopes are listed whose abundances change by more than a factor of two 2 as a result of varying the corresponding reaction rates within their adopted uncertainties.

while the isomer state decays directly to the ground state of ^{26}Mg and thus emits no gamma ray. The production and observation of ^{26}Al is of interest to the fields of astrophysics and nuclear astrophysics because the ground state's half-life is quite short on galactic timescales, meaning that its observation can give clues about ongoing nucleosynthesis in our Galaxy.

Evidence of ^{26}Al production in our Galaxy was first seen in presolar grains from the Allende meteorite that fell in 1969, studied by Lee *et al.* in Ref. [8]. Their study of Mg isotopic anomalies

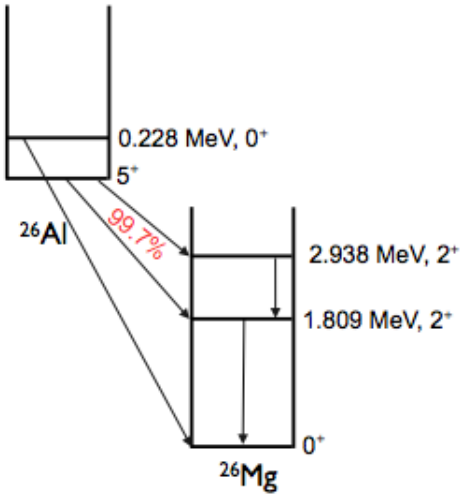

Figure 1.5. Energy-level diagram of states of interest in ^{26}Al and ^{26}Mg showing the β^+ decay of ^{26}Al to its daughter, ^{26}Mg. Note that the ground and isomer (0.228 MeV) states of ^{26}Al have different decay paths; specifically, the isomer state decays directly to the ground state of ^{26}Mg and does not emit the 1.809-MeV gamma ray. The J^π values of states are also shown.

in these meteorite grains revealed higher isotopic abundance ratios of ^{26}Mg/^{24}Mg than that of any other species of Mg, indicating an enrichment of ^{26}Mg in the grains of up to 10%. Because ^{26}Mg is the daughter nucleus produced in the decay of both the ground and isomer states of ^{26}Al, the ^{26}Mg enrichment was indicative of the presence of ^{26}Al that had decayed in-situ to create this surplus. After careful analysis, it was concluded that for the excesses observed, the ^{26}Al had to have been present in the grains when they were formed as opposed to an enhancement of ^{26}Mg through other means. This would imply that ^{26}Al was present in the solar system when it formed, indicating that a major nucleosynthesis event could have occurred just before or during the solar system's formation [8]. In addition to these first presolar grains, many other SiC presolar grains exhibit the same unique ^{26}Al enhancements, particularly in ^{26}Al/^{27}Al ratios plotted against ^{12}C/^{13}C ratios [9], as shown in Fig. 1.6. More recent studies and comparisons of presolar grains have used nitrogen and neon isotopic ratios to identify that CO novae create much higher ^{14}N/^{15}N ratios and much lower ^{20}Ne/^{22}Ne ratios than ONe novae [10, 11].

A number of astronomical observations contributed evidence of ^{26}Al production as well. Since the idea of stellar nucleosynthesis was first formalized [12], there have been predictions of which

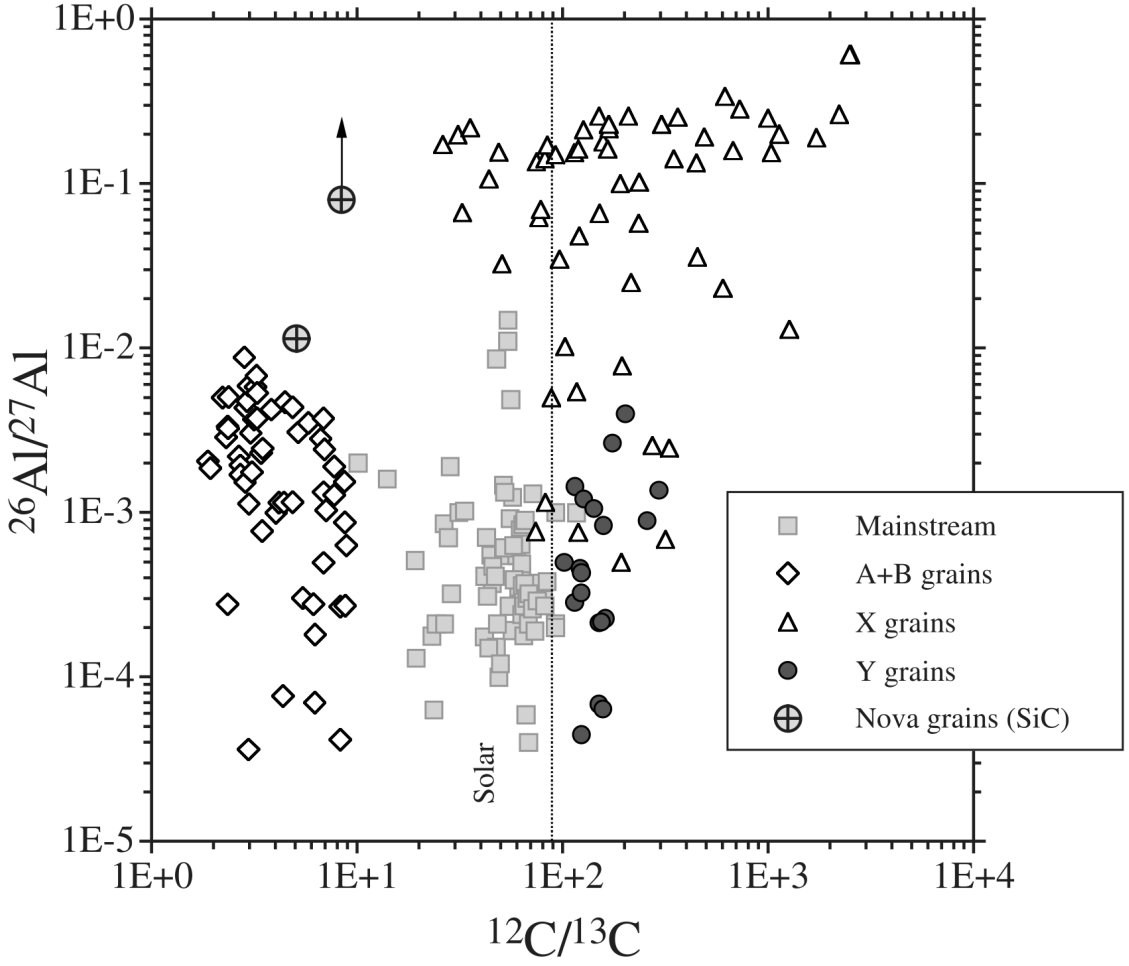

Figure 1.6. Aluminum and carbon isotopic ratios of nova candidate grains compared with those of SiC grains of different populations (see legend for details). Silicon carbide grains have been classified into several populations (X, Y, A+B) based on their C, N, and Si isotopic ratios. Error bars are smaller than the symbols. Nova grains have different aluminum isotopic ratios than grains of other origins. Reproduced from [9].

radioisotopes might have decay signatures that could be observed in space. One of the strongest contenders was the 1.809-MeV gamma ray from the $^{26}Al^{g}$ decay to the first-excited state of ^{26}Mg, shown in Fig. 1.5. The first observation of this gamma-ray line can be seen in Fig. 1.7, an observation made by the High Energy Astronomy Observatory 3 (HEAO-3)'s array of germanium detectors [13]. The emission was shown to be coming from the Galactic center. A later observation of this gamma-ray line in an all-sky map by the Imaging Compton Telescope (COMPTEL) confirmed that ^{26}Al production was occurring regularly along the galactic plane, making it a common

phenomenon throughout the galactic plane [14]. The INTErnational Gamma-Ray Astrophysics Laboratory (INTEGRAL) mission further confirmed that this production was occurring throughout the galactic plane and not in foreground sources by using the Doppler shift of this gamma-ray line to observe the rotation of the Galaxy's spiral arms, shown in Fig. 1.8. This latest observation from INTEGRAL also estimated a steady-state mass of $2.8 \pm 0.8\ M_{\odot}$ of ^{26}Al being produced in the Galaxy [15].

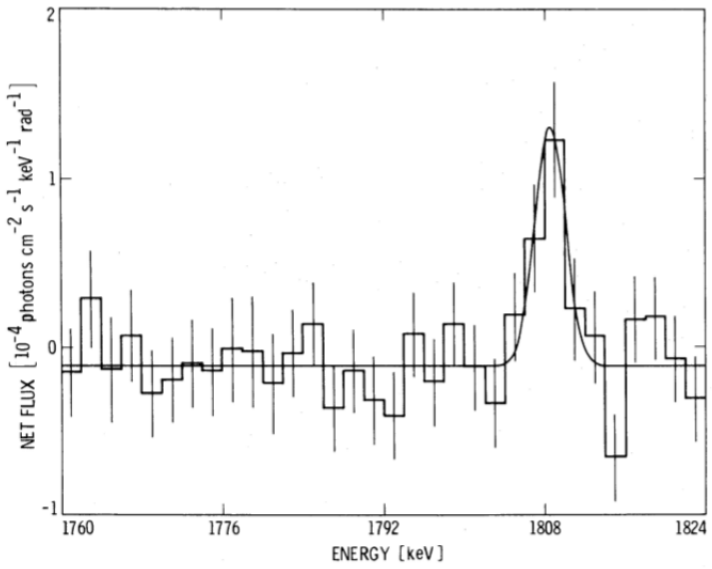

Figure 1.7. Net gamma ray flux from the HEAO-3 mission showing a peak at 1.809 MeV, taken in the fall of 1979. This is the energy of the gamma ray that comes from the decay of the ^{26}Al ground state to ^{26}Mg. Reproduced from [13].

Classical novae are one of several ^{26}Al production sites in our Galaxy, where up to 30% of the element may be produced [17]. Although other sites like Asymptotic Giant Branch (AGB) stars, Wolf-Rayet stars, and supernovae are expected to have higher yields of ^{26}Al in smaller, highly productive regions, lower mass classical novae make an important contribution to the smoother background production observed in the Galaxy [18].

As discussed above, classical novae are a type of cataclysmic stellar event that are defined as having only one observed outburst; they occur in binary systems composed of a white dwarf accreting mass from a secondary donor star. For optimal ^{26}Al production, the accretor is typically an

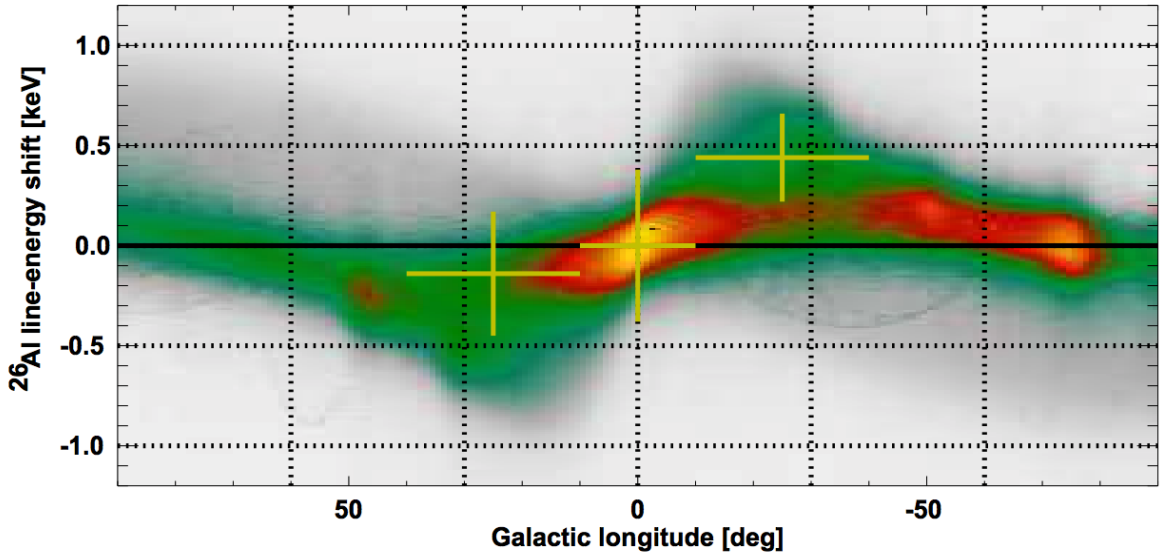

Figure 1.8. Doppler shifts of the 1.809-MeV gamma-ray line from the decay of $^{26}Al^{g}$ observed by the INTEGRAL mission showing the rotation of the Galaxy's spiral arms. Color map gives intensity of gamma rays observed. Reproduced from [16].

ONe white dwarf because peak temperatures in CO novae are not usually hot enough to produce heavier nuclei such as ^{26}Al [18]; additionally, less massive ONe white dwarfs correspond to higher overall yields of the isotope [19]. As the white dwarf continues to accrete, the collected material builds up on the white dwarf's surface until the nuclear reactions drive a thermonuclear runaway that reaches at peak temperatures between 0.1-0.4 GK, causing the outburst and a flurry of nucleosynthesis whose products—nuclei as heavy as ^{40}Ca—are ejected into the interstellar medium [20]. Galactic radioisotope tracers like ^{26}Al and the proposed ^{22}Na, both γ-ray emitters, are part of this chain of heavier elements produced and are of interest as an observational constraint on astrophysical models.

1.3 Measuring Reaction Rates Indirectly

As discussed above, the determination of reaction rates is crucial to the understanding of many astrophysical processes. The ideal situation is to conduct an experiment to measure the cross section of the desired reaction directly, which, when combined with particle densities and velocity, determines the reaction rate. While this is by far the most straightforward approach, some of the

(p, γ) reactions listed in Fig. 1.4 cannot be determined in this way due to various experimental constraints. A primary impediment to performing direct reactions in this region is a lack of radioactive ion beams produced at high enough intensities to acquire a statistically significant measurement in a reasonable time period. These radioactive ion beams are essential to directly measure reactions on unstable isotopes as targets of these isotopes cannot be produced because they typically have too short a lifetime. Even when a high-intensity radioactive ion beam can be produced (on the order of 10^{10} particles per second), many of the cross sections needed are so small that a direct measurement would take months or longer, which is prohibitive.

Before discussing how to measure reaction rates indirectly, it is crucial to have a good understanding of how stellar reaction rates are quantified and calculated. In classical novae, reactions are primarily charged-particle induced, meaning that the nuclei and particles involved are charged particles that interact via the Coulomb force with a potential

$$V_C(r) = \frac{Z_A Z_B e^2}{r} \tag{1.1}$$

where Z_i indicates the charge, or proton number, of the interacting nuclei and r is the distance between them. At a distance r close to the size of the nuclear radius, this repulsive potential V_C is akin to a barrier that the charged particles cannot cross, called the Coulomb barrier. Classically, charged particles cannot cross this barrier unless their relative energy is greater than V_C. For example, in ONe classical novae, where the peak temperature of the explosion is around 0.4 GK, we find the energy of the nuclei in the explosion to have a kinetic energy of $E = kT \approx 35$ keV. The Coulomb barrier for the ^{26}Al + p reaction has an energy of $V_C \approx 4.26$ MeV, so classically the ^{26}Al(p, γ) reaction studied in this work could not occur at this temperature. However, there is a probability of quantum mechanical tunneling through this barrier, and thus a finite probability of nuclear reactions occurring at energies below the Coulomb barrier. Things would be quite cold, dark, and hydrogen-rich if this were not the case.

To calculate the probability that Particle A could penetrate the Coulomb barrier of Particle B

and react, we take the ratio of the probability that Particle A can be found within the nuclear radius R_n of the Particle B over the probability that the Particle A can be found within the Coulomb radius R_C of Particle B:

$$P = \frac{\Psi(R_n)}{\Psi(R_c)} \tag{1.2}$$

At low energies like those seen in stellar explosions, $E << V_C$, and this probability can be approximated by the expression

$$P = \exp(-2\pi\eta) \qquad \text{where} \qquad \eta = \frac{Z_A Z_B e^2}{\hbar v} \tag{1.3}$$

is known as the Sommerfeld parameter [21]. This probability is sometimes called the Gamow factor.

At stellar energies much lower than the Coulomb barrier, the nuclear cross section is proportional to this probability as tunneling is roughly proportional to Eq. 1.3. Additionally, the cross section is also related to the de Broglie wavelength [21] via:

$$\sigma(E) \propto \pi\lambda\!\!\!^{-2} \propto \frac{1}{E} \tag{1.4}$$

Note that neither Eq. 1.3 nor Eq. 1.4 contain any explicit nuclear terms. Thus, when the two equations are combined:

$$\sigma(E) = \frac{1}{E}\exp(-2\pi\eta)S(E) \tag{1.5}$$

$S(E)$ describes the explicitly nuclear effects in the cross section. This term is referred to as the astrophysical S-factor.

This gives a basic expression for the nuclear cross section, but it needs to be related to the reaction rate in stellar phenomena. Imagine a star with particles A and B that will interact with N_A or N_B particles per volume, respectively, and relative velocity v. If the particles A are at rest and the particles B are moving, the problem can be simplified into A as the target nucleus and B as the projectile in the reaction. If the target nuclei A have a cross section of $\sigma(v)$ for a single reaction

with B, then the total reaction probability in the target can be represented as $P = N_A\sigma(v)$. The beam of particles B affects the cross section because of its total flux, which can be represented as $J = N_B v$. One can then multiply P and J to get the total reaction rate (i.e. the number of reactions per time per unit volume):

$$r = N_A N_B v\sigma(v) \tag{1.6}$$

In a stellar gas, the velocity of the particles is a distribution $\phi(v)$ that can be normalized to one over all velocities:

$$\int_0^\infty \phi(v)dv = 1. \tag{1.7}$$

By folding together the velocity distribution of Eq. 1.7 and the cross section product $v\sigma(v)$ of Eq. 1.6, the reaction rate averaged over the velocity distribution gives the reaction rate per particle pair [21]:

$$\langle\sigma v\rangle = \int_0^\infty \phi(v)v\sigma(v)dv. \tag{1.8}$$

In stellar environments, the gas is non-degenerate and in thermal equilibrium, and thus can be described via a Maxwell-Boltzmann velocity distribution [21]:

$$\phi(v) = 4\pi v^2 \left(\frac{m}{2\pi kT}\right)^{3/2} \exp\left(-\frac{mv^2}{2kT}\right) \tag{1.9}$$

where v is the relative velocity between particles of the gas, m is the mass of the nucleus of interest, T is the temperature of the gas (or star), and k is the Boltzmann constant.

Plugging the velocity distribution for a pair of interacting nuclei in a stellar environment (Eq. 1.9) into the reaction rate per particle pair of Eq. 1.8, gives the reaction rate per particle pair in a stellar environment:

$$\langle\sigma v\rangle = \int_0^\infty 4\pi v^2 \left(\frac{\mu}{2\pi kT}\right)^{3/2} \exp\left(-\frac{\mu v^2}{2kT}\right)\sigma(v)vdv \qquad \text{where} \qquad \mu = \frac{m_A m_B}{(m_A + m_B)} \tag{1.10}$$

is the reduced mass and v is the relative velocity.

Transforming this into an energy-centered equation by using the relationship between the center-of-mass energy and velocity, $E = 1/2\mu v^2$, gives

$$\langle \sigma v \rangle = \left(\frac{8}{\pi\mu}\right)^{1/2} \frac{1}{(kT)^{3/2}} \int_0^\infty \sigma(E) E \exp\left(-\frac{E}{kT}\right) dE. \tag{1.11}$$

Finally, to get the reaction rate per particle pair for charged-particle reactions, Eq. 1.5 is substituted into the above equation for $\sigma(E)$:

$$\langle \sigma v \rangle = \left(\frac{8}{\pi\mu}\right)^{1/2} \frac{1}{(kT)^{3/2}} \int_0^\infty S(E) \exp\left(-\frac{E}{kT} - \frac{b}{E^{1/2}}\right) dE \qquad \text{where} \qquad b = \frac{(2\mu)^{1/2}\pi e^2 Z_A Z_B}{\hbar}. \tag{1.12}$$

This general reaction rate equation's physical meaning can be seen in the two exponential terms. The left term comes from the Maxwell-Boltzmann distribution of the particles in the gas, whereas the right term comes exclusively from the calculation of tunneling through the Coulomb barrier. The combination of these two terms leads to a peak in the energy distribution about a characteristic energy E_0, also known as the Gamow energy. The Gamow energy can be found by taking the first derivative of the integrand in Eq. 1.12 with respect to energy to find a maximum, which when solved for the energy E gives

$$E_0 = \left\{\left(\frac{\pi k T Z_A Z_B e^2}{\hbar}\right)^2 \frac{\mu}{2}\right\}^{1/3} = 0.1220 \left\{\mu (Z_A Z_B T_9)^2\right\}^{1/3} \text{MeV}. \tag{1.13}$$

The Gamow energy E_0 is the most likely energy for nuclear reactions to occur; a pictorial representation of this can be seen in Fig. 1.9.

Equation 1.12 gives the general equation for a charged-particle nuclear reaction rate in a stellar environment; however, many of the (p, γ) reactions of interest in classical novae proceed through narrow, isolated resonances in the residual nucleus. This is reflected in the cross section component of the reaction rate, and especially in the S-factor, which becomes highly variable with respect to energy. While the cross section for a smoothly varying S-factor can be expressed via Eq. 1.5, the

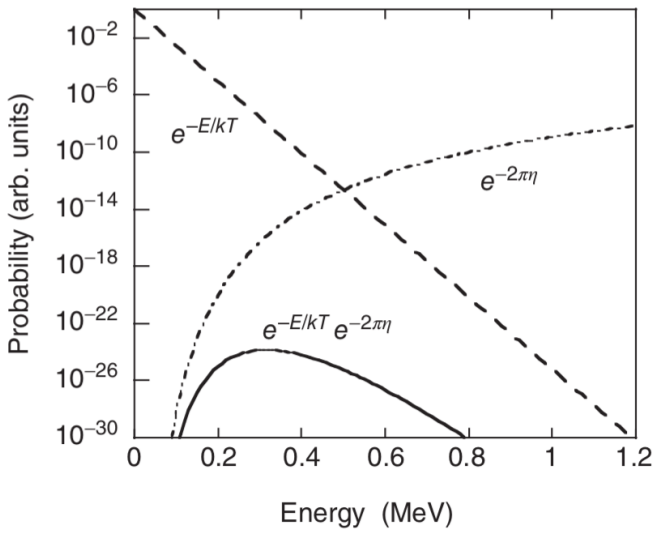

Figure 1.9. A plot of the two exponential terms of Eq. 1.12, showing the Maxwell-Boltzmann contribution (dashed line) and the quantum mechanical tunneling contributions (dashed-dotted line). The product of the two exponentials is shown illustrating the Gamow window (solid line) for the specific reaction $^{12}\mathrm{C}(\alpha,\gamma)^{16}\mathrm{O}$ at $T = 0.2$ GK. Reproduced from Ref. [22].

cross section of a resonance in a nucleus is approximated by the Breit-Wigner formula:

$$\sigma(E) = \frac{\lambda^2}{4\pi}\omega\frac{\Gamma_a\Gamma_b}{(E-E_r)^2 + (\Gamma/2)^2} \tag{1.14}$$

where Γ_i indicate the partial widths of the entrance and exit decay channels from the resonance; for the example of a (p,γ) reaction, the partial widths are Γ_p and Γ_γ. Γ is the total width of the state, E_r is the energy of the narrow resonance, and ω is the spin factor

$$\omega = \frac{(2J_r+1)}{(2J_A+1)(2J_B+1)} \tag{1.15}$$

where J_A and J_B are the spins of the two reacting nuclei (or target and projectile nuclei) while J_r is the spin of the resonance populated. When the resonant cross section $\sigma(E)$ (Eq. 1.14) is inserted

into Eq. 1.11, the reaction rate can be written as:

$$\langle \sigma v \rangle = \left(\frac{8}{\pi\mu}\right)^{1/2} \frac{1}{(kT)^{3/2}} \int_0^\infty \left(\frac{\lambda^2}{4\pi}\omega \frac{\Gamma_a \Gamma_b}{(E-E_r)^2 + (\Gamma/2)^2}\right) E \exp\left(-\frac{E}{kT}\right) dE, \tag{1.16}$$

which simplifies to

$$\langle \sigma v \rangle = \frac{\sqrt{2\pi}\hbar^2 \omega}{(\mu kT)^{3/2}} \int_0^\infty \Gamma_a(E)\Gamma_b(E) \frac{\exp(-E/kT)dE}{(E-E_r)^2 + (\Gamma/2)^2} \tag{1.17}$$

For narrow resonances, the Maxwell-Boltzmann factor $e^{-E/kT}$ and the partial widths Γ_i are roughly constant over the total width of the resonance [22]. This allows them to be replaced by their singular values at $E = E_r$:

$$\langle \sigma v \rangle = \frac{\sqrt{2\pi}\hbar^2 \omega}{(\mu kT)^{3/2}} \Gamma_a(E_r)\Gamma_b(E_r) \int_0^\infty \frac{\exp(-E_r/kT)dE}{(E-E_r)^2 + (\Gamma/2)^2} = \left(\frac{2\pi}{\mu kT}\right)^{3/2} \hbar^2 e^{-E_r/kT} \omega \frac{\Gamma_a \Gamma_b}{\Gamma} \tag{1.18}$$

By expressing the partial widths and omega as one term, $(\omega\gamma)_r$, the so-called resonance strength, the reaction rate for an isolated, narrow resonance can be given as:

$$\langle \sigma v \rangle = \left(\frac{2\pi}{\mu kT}\right)^{3/2} \hbar^2 e^{-E_r/kT} (\omega\gamma)_r. \tag{1.19}$$

The total reaction rate for all nuclei interacting requires multiplication by Avogadro's number on both sides, while the total reaction rate for a given temperature requires a sum over all narrow resonances for that reaction. Folding these two pieces in, the reaction rate for a given temperature is:

$$N_A\langle \sigma v \rangle = N_A \left(\frac{2\pi}{\mu kT}\right)^{3/2} \hbar^2 \sum_r e^{-E_r/kT} (\omega\gamma)_r. \tag{1.20}$$

Substituting numerical values for constants gives the simpler known form:

$$N_A\langle \sigma v \rangle = \frac{1.5399 \times 10^{11}}{(\mu T_9)^{3/2}} \sum_r (\omega\gamma)_r \; e^{-11.605 E_r/T_9} \qquad \left[\frac{\mathrm{cm}^3}{\mathrm{mol} \cdot \mathrm{s}}\right] \tag{1.21}$$

where μ is the reduced mass of the two initial reaction products in atomic mass units (amu), T_9 is the temperature of the astrophysical environment in GK, E_r is the resonance energy in MeV, and $(\omega\gamma)_r$ is the resonance strength in MeV, given by:

$$(\omega\gamma)_r = \frac{(2J_r + 1)}{(2J_A + 1)(2J_B + 1)} \frac{\Gamma_a \Gamma_b}{\Gamma} \tag{1.22}$$

By measuring the widths Γ_i, the angular momenta J_i, and the energies E_r of the resonances of interest found in this equation using indirect measurements, the reaction rate can be calculated. A number of experimental techniques can be used to measure the resonance energies, or excited states above the particle separation threshold, of the compound nucleus of interest. Angular distributions can yield information on the J_i of the resonance, while branching ratio measurements give Γ_a/Γ as a simple percentage; one then only needs a value for Γ_b, the partial width of the second decay type. For a charged particle, the partial width Γ_b can be calculated via $\Gamma_b = C^2 S \Gamma_{sp}$, where C is the isospin Clebsch-Gordon coefficient, S is the spectroscopic factor (an experimentally determined value), and Γ_{sp} is the single particle width (a theoretically calculated value). In the case that Γ_b is a gamma partial width, this value can be determined through lifetime measurements of the state ($\Gamma = \hbar/2\tau$), a Weisskopf estimate, or theoretical calculations.

Indirect reaction measurements are often the only feasible method of determining reaction rates when limitations to direct measurements arise, but they require different experimental techniques. The next chapter details the development of an experimental setup designed specifically to obtain the quantities relevant to determining reaction rates of astrophysical interest via indirect measurements, in addition to measurements important to nuclear structure that will not be discussed here. The setup was used to measure the properties of states in ^{27}Si to determine the ^{26}Al$(p,\gamma)^{27}$Si reaction to better understand the nucleosynthesis of ^{26}Al in classical novae.

1.4 The ^{26}Al$^{g,m}(p,\gamma)^{27}$Si Reaction Rates

Figure 1.10 illustrates a variety of reactions affecting production and destruction of ^{26}Al in classical novae, both for the ground state and the isomer state. A number of (p,γ) reactions and

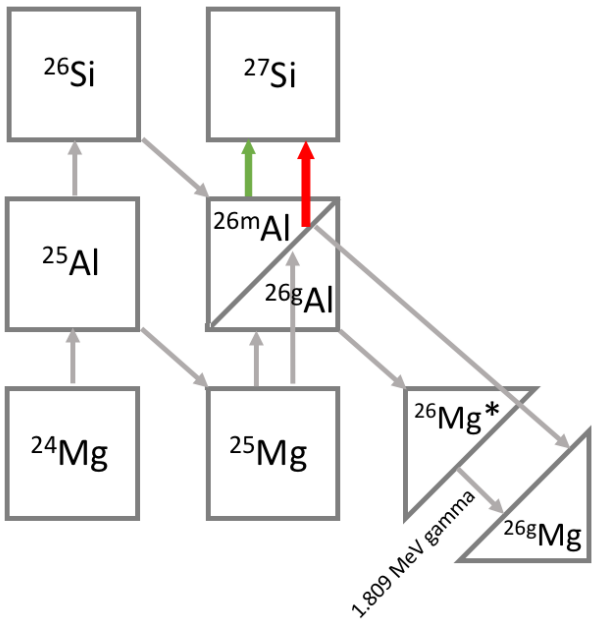

Figure 1.10. Reactions responsible for the production and destruction of ^{26}Al in classical novae. Arrows indicate different reaction paths that occur in classical novae. The destruction of ^{26}Al is shown by the red and green arrows.

β^+ decays contribute to these mechanisms. From the diagram, one sees that the $^{26}\mathrm{Al}^{g}(p,\gamma)^{27}\mathrm{Si}$ and $^{26}\mathrm{Al}^{m}(p,\gamma)^{27}\mathrm{Si}$ reaction rates both play a role in the destruction of ^{26}Al; the latter is one of the only reactions important to ^{26}Al in novae that has not yet been fully measured directly. However, as these are important reactions for both presolar grain and space-based gamma observations, they have been previously studied in a variety of ways.

The $^{26}\mathrm{Al}^{g}(p,\gamma)^{27}\mathrm{Si}$ reaction has been studied indirectly most recently by A. Kankainen *et al.* in 2016 [23] by studying spectroscopic factors and resonance strengths in ^{27}Si with gamma spectroscopy via the $^{26}\mathrm{Al}(d,n)^{27}\mathrm{Si}$ reaction. This reaction was used to determine proton partial widths and J^{π} values in states of resonance energies at 276 keV and below of interest primarily for sites of ^{26}Al production other than classical novae. This was primarily studied to verify that shell model predictions matched measured characteristics of the resonances for use in other studies. The $^{26}\mathrm{Al}^{g}(p,\gamma)^{27}\mathrm{Si}$ reaction was also recently studied by S.D. Pain *et al.* in 2015 [24], by examining proton resonances in ^{27}Si through mirror states in ^{27}Al populated via the $^{26}\mathrm{Al}^{g}(d,p)^{27}\mathrm{Al}$ reaction,

particularly those within 1 MeV of the proton threshold of ^{27}Al, corresponding to states in the same region in ^{27}Si. These indirect studies were aimed at resonances important for lower temperature nucleosynthesis of ^{26}Al^{g} in AGB and Wolf Rayet stars, and concluded that the 127-keV resonance would dominate the rate in these sites. The 184-keV resonance that dominates the ^{26}Al$^{g}(p,\gamma)^{27}$Si reaction rate at nova temperatures has been directly measured by Ruiz *et al.* in 2006 [25]. A direct measurement is the gold standard, but because of the difficulty of creating radioactive ion beams of high enough intensity, it is often difficult to achieve. In Ruiz *et al.* [25] the experiment was performed in inverse kinematics with a ^{26}Al^{g} beam on a hydrogen gas target and the ^{27}Si recoils were detected in a silicon detector. They performed the measurement around the 184-keV resonance and an off-resonance run was used for background subtraction. They found the resonance energy to be 184(1) keV with a resonance strength of 35(7) μeV, indicating that novae are a significant secondary source of ^{26}Al^{g} in the Galaxy [25].

While the reaction rate for proton capture on the ground state of ^{26}Al in novae has been constrained by direct measurements, this has not been possible for ^{26}Al$^{m}(p,\gamma)^{27}$Si due to the lack of intense ^{26}Al^{m} beams. The ^{26}Al$^{m}(p,\gamma)^{27}$Si reaction has, however, been studied indirectly using a variety of measurements, with the most recent experiment being a measurement of mirror states in ^{27}Al to constrain the reaction rate by Almaraz-Calderon *et al.* [26]. An ^{26}Al isomeric beam was used to perform a (d, p) reaction to populate these states via the mirror reaction of ^{26}Al$^{m}(p,\gamma)^{27}$Si, and any contributions from ^{26}Al^{g} were subtracted out by using the results from Ref. [24] mentioned in the previous paragraph. They were able to determine upper limits for resonance strengths in low energy states corresponding to excited states in ^{27}Si. In particular, two excited states corresponding to the 7.838 MeV state and the 8.070 MeV state in ^{27}Si are expected to dominate the rate with calculated resonance strengths of 0.03 μeV and 165 meV, respectively. The calculated reaction rate from Ref. [26] is shown in Fig. 1.11, and shows that the 146- and 378-keV resonances contribute differently to the overall isomer reaction rate at different temperatures.

The states in ^{27}Si important to the ^{26}Al$^{m}(p,\gamma)^{27}$Si reaction rate have been studied above the proton threshold (7.463 MeV, or 7.691 MeV for the ^{26}Al^{m} + p threshold) by Lotay *et al.* [28] via

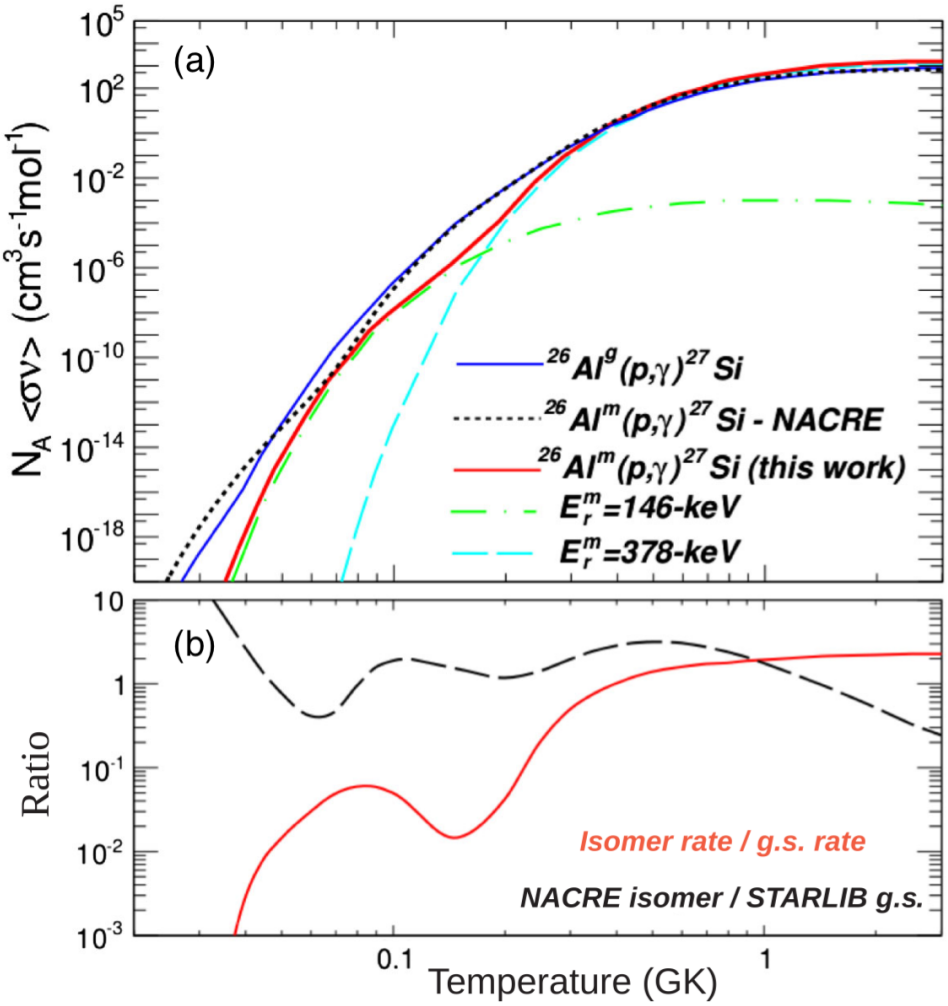

Figure 1.11. (a) Upper limits for the rate of the $^{26}Al^m(p,\gamma)^{27}Si$ reaction in stellar environments as a function of temperature. The isomer (m) rate (Ref. [26]) is shown compared to the ground state (g) and the recommended NACRE rate [27]. (b) Ratios between the experimental isomeric (m) rate (Ref. [26]) and the isomeric (solid line) and ground state rates recommended by the NACRE-STARLIB calculations (dashed line) [27]. Reproduced from Ref. [26].

the study of gamma transitions from ^{27}Si. States in ^{27}Si were populated via the ^{16}O(^{12}C, n)^{27}Si reaction and gamma rays were detected in the Gammasphere array, which is a large angular coverage gamma detector array. This study was the first to find that the states at 7.838 and 8.070 MeV were expected to dominate the isomer reaction rate, and was done by using gamma-ray spectroscopy with angular correlation information to determine the energies and potential spin-parities of states populated in ^{27}Si.

Additionally, ^{27}Si energy levels and proton branching ratios were studied by Deibel *et al.* [29] using YLSA (the Yale Lamp Shade Array) and the same Enge Split-Pole Spectrograph discussed in this work at the Wright Nuclear Structure Laboratory. This work used the ^{27}Al(^{3}He, t)^{27}Si reaction to study energy levels in ^{27}Si and the ^{28}Si(^{3}He, α)^{27}Si*(p)^{26}Al reaction to study both energy levels and proton branching ratios of states in ^{27}Si with excitation energies down to 8.136 MeV, 445 keV above the threshold, but no lower. This study is similar to the experiment performed in this work, but utilizes a different reaction to measure proton branching ratios and achieves lower energy state measurements.

These studies have identified the need for further studies of the reaction rate for the isomer reaction to attempt to further reduce these uncertainties. The resonance energies of states in ^{27}Si are fairly well known from previous studies, but the proton branching ratios are only known down to 8.136 MeV, which is 445 keV above the proton threshold for the isomer state reaction and thus cannot determine the resonance strength of the proposed 146- and 387-keV resonances of importance in that reaction. We utilized a new detector array (described in detail in chapter 2) to measure proton branching ratios Γ_p/Γ in ^{27}Si even closer to the proton threshold in ^{27}Si as an indirect method of further constraining the ^{26}Al^{m}(p, γ)^{27}Si reaction rate.

2 Instrumentation

Currently, the $^{26}\mathrm{Al}^{m}(p,\gamma)^{27}\mathrm{Si}$ reaction rate has many associated uncertainties due to the limitations of indirect experimental measurements and the infeasibility of direct measurements. The following chapter outlines the installation and upgrade of an experimental setup designed to measure proton branching ratios Γ_p/Γ in ^{27}Si close to the proton threshold via the $^{27}\mathrm{Al}(^{3}\mathrm{He},t)^{27}\mathrm{Si}^{*}(p)^{26}\mathrm{Al}^{\mathrm{g},m}$ reaction.

The Enge Split-Pole Spectrograph (SPS) now installed at Florida State University's John D. Fox Accelerator Laboratory was originally located at the Wright Nuclear Structure Laboratory (WNSL) at Yale University, where it played a vital part in many successful experimental campaigns over the several decades it was operational. This setup was dismantled in 2013 after the closure of the WNSL and transported to FSU to start a next-generation experimental program in a new location. A diagram of the previous configuration, which is analogous to the current configuration, can be seen in Fig. 2.1; it included the SPS magnet and camerabox housing, a focal plane detector setup, a target, and a backwards angle Si detector array, YLSA (Yale Lamp Shade Array). Each of these pieces will be discussed in more detail in the following sections.

SPS experiments are typically done with a light-ion beam incident on a heavy target. After the reactions occur in the target, light reaction products move forward into the SPS and are momentum-analyzed based on their magnetic rigidity. The magnetic field, placement of the focal plane detector, angle of the magnet, and opening of the entrance slits to the magnet determine what subset of the reaction products can be detected in the focal plane detector. At the same time, the heavier reaction products (often in an excited state) remain in the target, where they can decay via charged-particle emission provided that their excitation energy (E_x) is greater than the charged-particle separation energy, $E_x > S_{c.p.}$, the amount of energy it takes to remove a specific charged particle from the nucleus. Separation energies are calculated by using the atomic masses of the particles involved, such as this calculation for a proton's separation energy:

$$S_p = [m(A-1,Z-1) + m(1,1) - m(A,Z)]c^2 \tag{2.1}$$

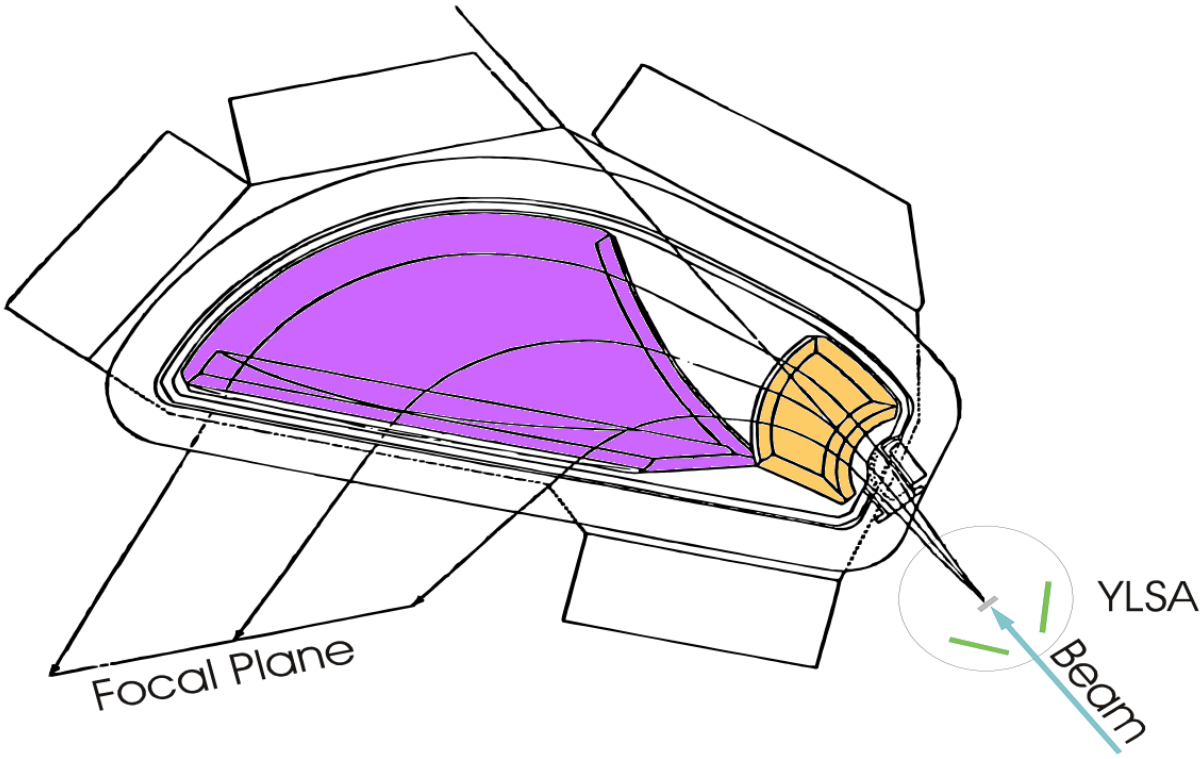

Figure 2.1. Schematic of the SPS setup when it was housed at Yale's Wright Nuclear Structure Laboratory, from Ref. [30]. The two separate, or split, poles are colored in purple and gold. The beam is seen on the bottom right (blue), impinging on the target (light grey line), which is surrounded at backward angles by YLSA (green). Light ions leave the target and follow curved trajectories, shown by the thin black arrows, through the SPS and are detected at the focal plane of the magnet, where a focal plane detector (not shown) sits.

where A and Z indicate the total number of nucleons and the number of protons, respectively, and $m(1,1)$ is the mass of a hydrogen atom. Charged particles emitted in these decays are then detected at backwards angles in YLSA in coincidence with the corresponding light products detected in the focal plane (the Si array is positioned at backward angles to avoid damage by high backgrounds in the detectors due to beam scattering). These Si array and focal plane detector coincidences can then be used to determine quantities like branching ratios and angular momentum transfers of decay products. Additionally, one can calculate the resonance energies populated in the reaction using $E_{resonance} = E_x - S_{cp}$. E_x is the excitation energy of the compound nucleus created and S_{cp} is the charged particle separation energy. E_x is related to the energy of the light-reaction particle measured in the focal plane detector, which is determined by the detected location of the particle

in the focal plane detector; the momentum of the particle mv is specifically related to the magnetic field of the SPS and the position detected on the focal plane detector ρ by $B\rho = mv/Q$, where Q is the charge of the particle. Lastly, one can measure angular distributions of excited states populated in the heavy reaction products by rotating the magnet about the target chamber, allowing J^π (spin-parity) assignments to be made (although this capability was not utilized in the current study).

While the principles behind the new setup at FSU will be the same as the one at Yale, the detector systems have been upgraded. The Enge SPS itself, the target chamber, and the housing for all the parts have remained unchanged. YLSA has received the largest overhaul; it has been redesigned as the Silicon Array for Branching Ratio Experiments, or SABRE, and is complemented with an upgrade from the original conventional electronics to digital electronics. The focal plane detector setup has undergone repairs and there are plans for a redesign underway. The setup is now known at FSU as the Super Enge Split-Pole Spectrograph, or SE-SPS. In the following sections, each component of the experimental setup will be discussed in detail.

2.1 John D. Fox Accelerator Laboratory

No experiment using the SPS can be performed without an ion beam, so the John D. Fox Accelerator Laboratory at FSU, where the SPS is housed and where all the experimental beams are produced, will be briefly discussed. The layout of the laboratory is shown in Fig. 2.2. Starting at the bottom right corner of Fig. 2.2, an ion source injects the isotope of interest into the beamline. The ion source used for beams created from solid materials is an NEC SNICS-II (National Electronics Corporation Source of Negative Ions by Cesium Sputtering) cesium sputter ion source, while beams created from gaseous materials like ^{3}He and ^{4}He utilize the NEC rf-discharge source [31]. These ion sources inject the negatively-charged beam isotopes into the Super-FN tandem van de Graaff accelerator manufactured by the High Voltage Engineering Corporation. This tandem has a terminal voltage of up to +9 MV in the center of its length that attracts the negatively charged ions once injected. These ions then pass through a stripper foil at the center of the terminal that removes electrons (for the lightest beam species, H, He, and Li, it removes all electrons). After the ion is stripped, it becomes positively charged and continues accelerating through the tandem, repelled

by the positively-charged center terminal and attracted toward the grounded end of the tube. This is a clever way to allow more acceleration for voltage, as the particle energy leaving the tandem is approximately given by $E = eV_{tandem}(Z + 1) + E_{injection}$, and results in positively ionized nuclei leaving the tandem with higher energies.

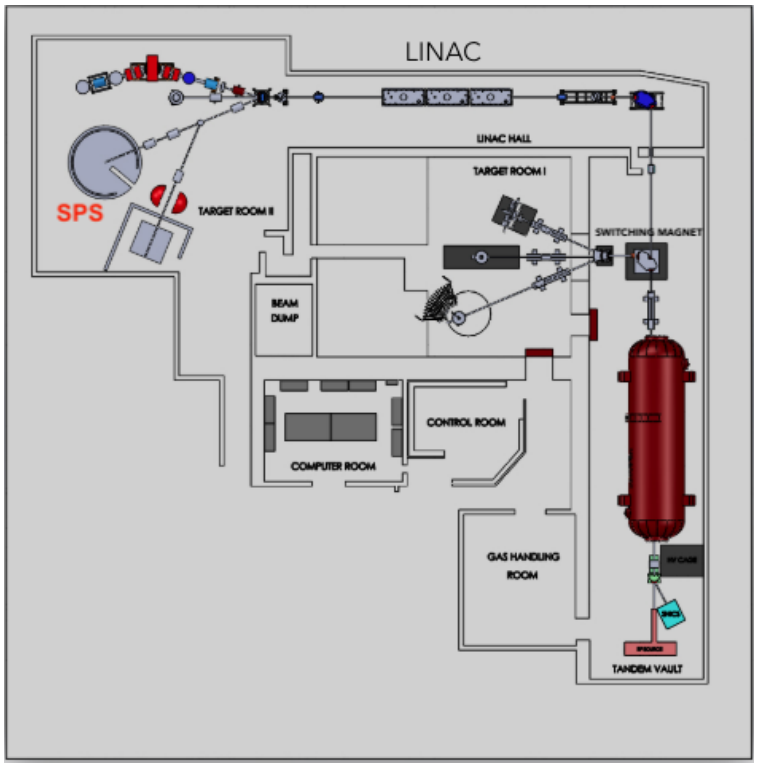

Figure 2.2. A schematic of the John D. Fox Accelerator Laboratory at Florida State University, from [31]. The two sources are shown in the bottom right corner, the red capsule on the right is the tandem van de Graaff accelerator, and the SPS setup is labeled in red at the top left. See text for details.

The beam particles proceed out the tandem and up to the top right corner of Fig. 2.2, where a magnet bends the particles and sends them to the left of Fig. 2.2 until they reach the switching magnet. This magnet directs the particles to the correct beam line, which in this case is the line that leads to the circle labeled “SPS” in Fig. 2.2. There are several other magnets along the beamline that provide focusing of the beam resulting in a focused beam spot at the target on the order of 1-2 mm in diameter.

Beams of greater than 8.7 MeV/u, or 8.7 MeV per nucleon, can be produced from an extra energy boost from the 8 MV linear accelerator, or LINAC. The LINAC at FSU consists of a beam

buncher, which bunches the beam into small timed groups; 12 accelerating resonators, which use radiofrequency oscillations of electric field to accelerate the bunches; and a re-buncher at the end [31]. The LINAC can more than double the beam energy, depending on what type of beam species is chosen [31].

2.2 Enge Split-Pole Spectrograph

The Enge SPS installed at FSU is a magnetic spectrograph comprised of two separate poles surrounded by one coil; the two poles provide second-order double focusing over a broad range of energies [32]. The SPS is the large device in the center of Fig. 2.1; the two poles can also be seen there. It is roughly 35 tons, has a maximum acceptance of 12.8 msr (which is one of the largest of any Enge spectrograph), and has a maximum magnetic field of about 16.3 kG. The range of the radius of curvature ρ, which specifies the minimum and maximum radii of a particle's trajectory bent by the spectrograph, is 51 cm $< \rho <$ 92 cm. Two closely related quantities, the dispersion and the resolving power, are D = $\Delta x/\Delta p$ ~1.96 and $\Delta p/p$ = 1/4290, respectively [33], where x is the position on the focal plane, Δp is the momentum spread (or full width at the base of a peak), and p is the momentum.

Light reaction particles in the SPS follow trajectories governed by the familiar equation $B\rho = mv/Q$, where $B\rho$ is known as the magnetic rigidity (the product of the magnetic field strength and the radius of curvature), $mv = p$ is the momentum of the particle, and Q is the charge of the particle [34]. As particles enter the SPS, they are bent according to their magnetic rigidity; higher rigidity implies higher momentum, and higher rigidity/momentum means a larger radius of curvature in the constant, uniform magnetic field. This magnetic rigidity is determined at the focal plane of the magnet by the focal plane detector where the position along the focal plane, or ρ, is measured; particles are refocused there after being dispersed according to momentum. Interestingly, the high- and low-momentum particles are focused by different sections within the magnet as they travel through the SPS; this is described in detail in Ref. [32].

The SPS was disassembled at the WNSL, as shown in Fig. 2.3, and relocated to FSU in Fall 2013; it was moved into the lab at FSU in August 2016. While in storage, the successful drilling

Figure 2.3. The SPS being moved out of the lab by crane at the WNSL to start its journey to Florida.

Figure 2.4. The freshly poured concrete pedestal at FSU and track that the SPS sits on to rotate about the target chamber.

of a test pile in the lab floor in Fall 2015 was used to determine the final engineering plans for the SPS support pedestal. This was followed by the drilling of 27 support piles to hold up the concrete pedestal, shown in Fig 2.4, that was laid in August 2016 and supports the entire SPS structure. The SPS was placed on the pedestal in January 2017, shown in Fig. 2.5, and the gas handling systems and power for the magnet were installed in Spring and Summer of 2017. The target chamber was installed in Fall 2017 and the beamline was placed during Spring 2018, with the final result shown in Fig. 2.6. During the installation of the SPS beamline, the focal plane detector was installed in the camerabox; this detector will be discussed in the next section. First beam on target was achieved in June of 2018, discussed in more detail in Chapter 3.

2.3 Focal Plane Detector Setup

The focal plane detector shown in Figs. 2.7 and 2.8 is the same focal plane detector that was used at the WNSL; it is placed at the focal plane of the SPS and is a position-sensitive ionization chamber, which is often used in combination with a scintillator bar. The chamber is vacuum tight with entrance and exit windows of 6.35-micron aluminized mylar foil so that it can hold isobutane gas with typical pressures of 70 to 300 Torr; the gas is handled through a system that creates a constant slow flow of gas through the detector but maintains a constant pressure. The gas pressure limits the biasing voltages of the focal plane detector, discussed below, as too much bias and/or

Figure 2.5. The SPS after its installation on the pedestal in Spring 2017. The maroon section covers the magnetic pole pieces, and the large silver section is the camerabox, where the focal plane detector setup is installed.

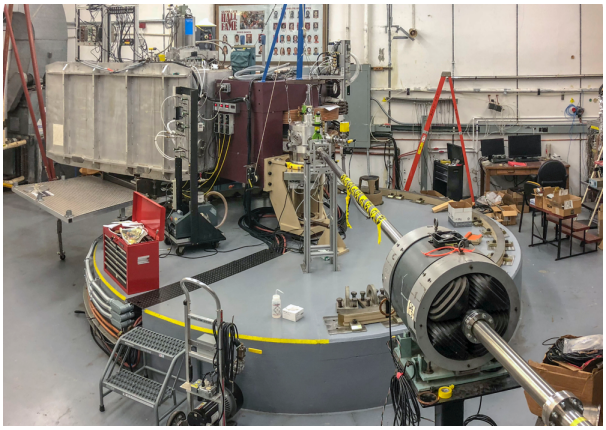

Figure 2.6. The SPS with its target chamber and beamline finally installed, as well as the power, electronics, and cooling systems for the magnet.

too little gas can lead to sparking in the detector and degrade detector performance; a variety of acceptable pressures and voltages are given in Table 2.1.

Table 2.1. Functional biases for a variety of gas pressures in the focal plane detector. These have been used successfully during bench testing or experiments. If sparking occurs, one can turn down the anode wire bias or increase the gas pressure. Gain on the wires and cathode can be adjusted by changing voltages.

Gas pressure (Torr)	Anode wire bias (V)	Cathode plate bias (V)
70	+1050	-550
70	+1050	-500
70	+1035	-550
80	+1150	-550
100	+1250	-600
110	+1320	-620
110	+1200	-600
125	+1425	-650
130	+1360	-725
150	+1500	-700

After the light reaction products are momentum analyzed, they enter the detector from the right of Fig. 2.8, where they proceed to ionize the gas as they move through the drift region. The range of radius of curvatures able to be measured by the focal plane detector corresponds to

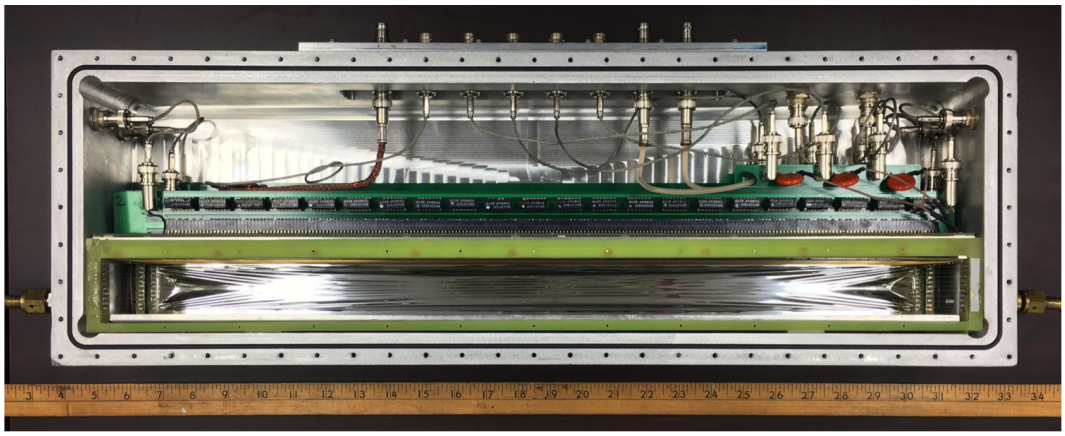

Figure 2.7. A front view of the inside of the focal plane detector with the front of the detector removed. At the bottom left and right the gas in and out lines can be seen; these provide a constant, slow flow of gas through the detector to eliminate contaminants. The entire housing is made of aluminum and has a front and back plate that attach via screws and an o-ring seal, which can be seen here on the front face. The aluminized mylar windows are attached on separate metal plates that attach via screws and an o-ring seal roughly the size of the field-shaping apparatus. The yellow rectangle is the front panel of a printed circuit board housing that contains the field-shaping elements. The vertical panels of these field-shaping elements create a smooth transition from the bias of the cathode plate, on the bottom, to the grounded Frisch grid on the top. The green housing near the top is one of two anode wire and pickup pad assemblies, described in the text.

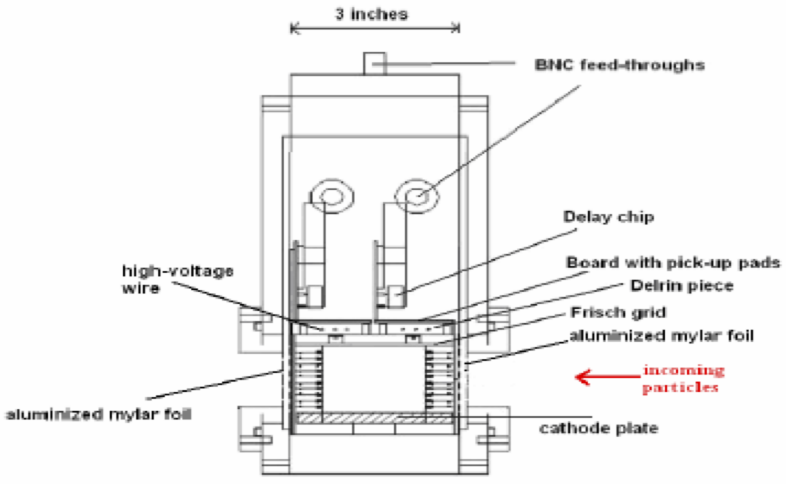

Figure 2.8. Schematic of the focal plane detector (side view) from Ref. [35].

$\Delta\rho$ =17 cm. The drift region inside the detector is a rectangular cuboid volume surrounded by field-shaping elements specifically designed to create as uniform of an electric field as possible within this volume [36]. The field-shaping elements consist of four biased field-shaping wire grids, which make up the sides of the drift region and are biased through a voltage divider to create a uniform field between the grounded Frisch grid on the top and a negatively biased cathode plate on the bottom (typically biased between -500 and -700 V). The electric field created by the field-shaping pieces in the detector guides the ionization electrons upward through the drift region. Above the Frisch grid are identical front and back assemblies of three anode wires each (typically biased between -1300 and -1550 V), with pickup pads connected to delay line chips directly above the wires, shown in Fig. 2.9.

After passing through the Frisch grid, the electrons are accelerated toward the anode wires and induce a signal in the pickup pads directly above the anode wires a the top of the detector. The pickup pads are separated into strips angled at 45° to the sides of the detector, parallel to the particles' trajectories [37]. Each pickup pad is 0.09" wide and 1.4" long (measuring along the slanted direction), with a 0.01" separation between each pad; the pads are shown in Fig. 2.10. The delay line chips that connect to each pad are 50 ns delay chips with a 50 ohm impedance; they each have 10 taps to create a 5 ns delay per tap [36]. There are a total of 440 pickup pads with a 5 ns delay per pad, equating to a nominal total delay of 2.2 μs for the entire active length of the focal plane detector. Signals from the pickup pads travel through these delay line chips to determine the positions of the particles in the detector. The time difference between signal detection at each end of the wire assembly yields particle position [35]. At the same time, the cathode plate attracts the positively charged gas ions to give a measurement of the energy loss of the particle through the detector gas, ΔE.

Lastly, the particles that make it through the detector exit the focal plane detector's rear window and are detected in a plastic scintillator bar that sits behind the focal plane detector; the bar is connected at each end to a photomultiplier tube (PMT) that detects the light created by particles in the scintillator and converts it into an energy pulse. The plastic scintillator detects the residual

energy E of the particles. From these three signals of ΔE, E, and position, 2-D spectra can be created in order to perform particle identification; this will be discussed in detail in later chapters.

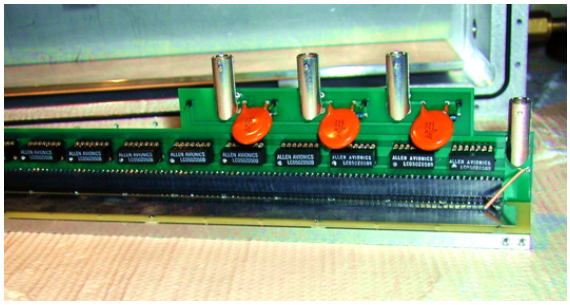

Figure 2.9. The position sensitive apparatus, which contains the anode wires, pickup pads, and delay line chips [36].

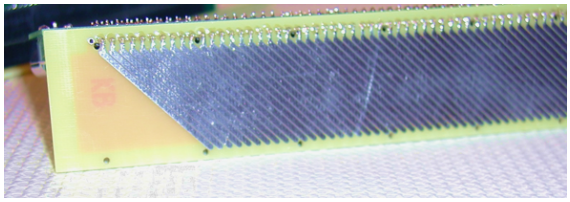

Figure 2.10. A close up of the pickup pads [36].

In Spring 2016, the focal plane detector underwent repairs to improve its functionality; these included repairing some of the field-shaping wires that had broken and polishing the cathode plate in an attempt to smooth out imperfections that caused variations in the ΔE signal as a function of position. Fixing a few broken wires on the Frisch grid was discussed but ultimately dismissed as being more likely to cause harm than good due to the tight spacing of the wires.

In February of 2018, the focal plane detector was installed in the camerabox of the SPS (Fig. 2.11) for the first time since it had been at Yale. It sits on a platform that can be moved up/down, left/right, and rotated, so that the detector can be moved into the focal plane of the magnet for experiments. The scintillator bar, which sits in a groove just behind the focal plane detector, is shown installed in Fig. 2.12. All the signals for each detector are fed out through the roof of the camerabox before they are preamplified and sent to a CAEN v1730 digitizer, described in more detail in Section 2.5.

After installation, the focal plane detector was first tested in April 2018 with a ^{228}Th alpha source placed in the target chamber and the magnet set to 4.889 kGauss (which corresponds to +260 A in the magnet). The resolution achieved was 43-keV FWHM (the full width of the peak at half its maximum) and the spectrum is shown in Fig. 2.13. This was worse than the resolution previously achieved at Yale; however, the thickness of the source and the location of the focal plane

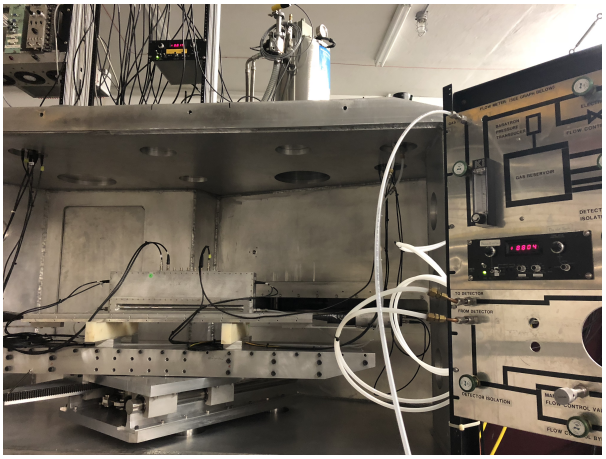

Figure 2.11. The focal plane detector installed in the camerabox, with its gas-handling system shown on the right.

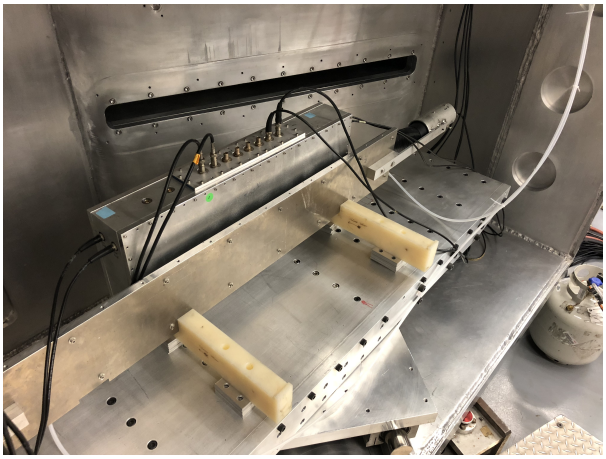

Figure 2.12. The focal plane detector sits in front of the scintillator bar facing the exit of the SPS. The scintillator bar has a photomultiplier tube on each end for detecting the light created by the particles that exit the focal plane detector.

detector (which was not placed at the exact focal plane of the magnet) likely contributed to this less-than-ideal resolution. Typical experimental resolution of the detector in operation at Yale was roughly 30-35 keV [35], and since this first test was taken resolutions as low as 25 keV have been achieved for some experiments. (Resolution depends on both the detector and the experimental parameters, so it will vary depending on what is being measured even if the detector is at its conditions for best resolution).

2.4 SABRE: The Silicon Array for Branching Ratio Experiments

SABRE, a next-generation array of Si charged-particle detectors, was modeled off of the Yale Lamp Shade Array (YLSA) from the SPS experimental setup at Yale's Wright Nuclear Structure Laboratory [30]. The array detects charged particles (e.g. protons) from the decays of excited states populated in heavy reaction products in the target. When particles are detected by YLSA (SABRE) in coincidence with the light reaction products detected at the focal plane, various data about the states populated in the reaction can be obtained: specifically branching ratios and angular momentum transfers of the decays, as described below. YLSA was comprised of a set of five YY1 Si detectors manufactured by Micron Semiconductor Ltd. that were assembled in the shape of a

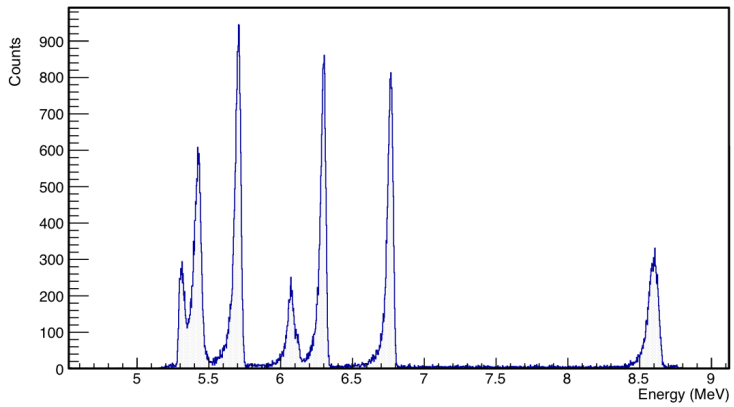

Figure 2.13. Focal plane detector spectrum for a ^{228}Th α source. The seven alpha-decay peaks seen here from left to right have energies of 5.340, 5.423, 5.685, 6.050, 6.288, 6.788, and 8.785 MeV.

five-sided lampshade. This lampshade array was then placed upstream of the target, oriented such that the symmetry axis of the array coincided with the beam axis, with the wider base of the lampshade closest to the target, similar to SABRE, shown in Fig. 2.14. This lampshade design allows for maximum solid angle coverage (roughly 14% of 4π in YLSA [35]) and geometric efficiency, providing the range to measure angular distributions from roughly 131° to 166°.

SABRE will operate in a similar manner to YLSA, and while the original lampshade idea has been retained, it has been reworked with a newer, previously unavailable design of Si detectors. SABRE is comprised of five Micron MMM Si-strip detectors, shown in Fig. 2.15. The new MMM detectors have the advantage of possessing both a larger outer radius and a smaller inner radius compared to the original YY1 models, allowing for more solid angle coverage by each detector. Additionally, the MMM detectors are are segmented into 16 annular strips on the junction side (fronts) and 8 radial strips on the ohmic side (backs), while the YY1s had 16 annular strips on the front and no segmentation on the backs.

Two sets of five MMM detectors with different thicknesses and dead layers were purchased for use with SABRE. The dead layer is the amount of inert material that particles must pass through before reaching the active volume of the Si detector, and thus causes undetected energy loss. The first set of MMMs has a 400-μm thickness type 2 M Si wafer, meaning the detectors have a dead layer of 500-nm (equating to a 90-keV proton-energy threshold to reach the active volume) and “a

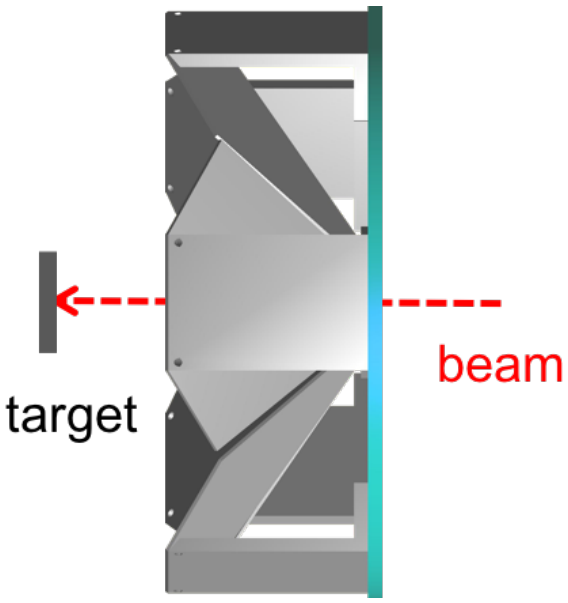

Figure 2.14. A SABRE CAD drawing showing the array's orientation with respect to the beam and target. This is also how the YLSA array was positioned.

continuous metal coverage of standard thickness over the whole active area" [38]. The second set has a 500-μm thickness type 9.5 P/2 M wafer, meaning that on the junction side the detectors have a dead layer of 50 nm (equating to a 10-keV threshold for protons) and "a periphery metal band, typically 30 μm wide, around the edge of the active areas and contact pads for wire bonding. The majority of the active area [is] metal coverage free" [38]. The backs of this second set of detectors are the 2 M scheme described for the first set of detectors, since a thin dead layer is only needed on the front side of the detectors where particles will be entering and makes the set more cost effective. The set of thin dead-layer detectors will be used for experiments where we anticipate very low energy charged-particle emission, as these particles will deposit more of their energy in the active silicon volume due to their lower energy loss in the dead layer.

After modeling several configurations with various detectors, the setup shown in Fig. 2.16 was determined to be the best for maximum solid angle coverage while also adhering to the geometric constraints of the existing target chamber. This new lampshade structure allows for larger geometrical efficiencies: over double those of the old array according to Monte Carlo simulations described in Ref. [30] and adapted for the new SABRE array. (Appendix A contains the details of this sim-

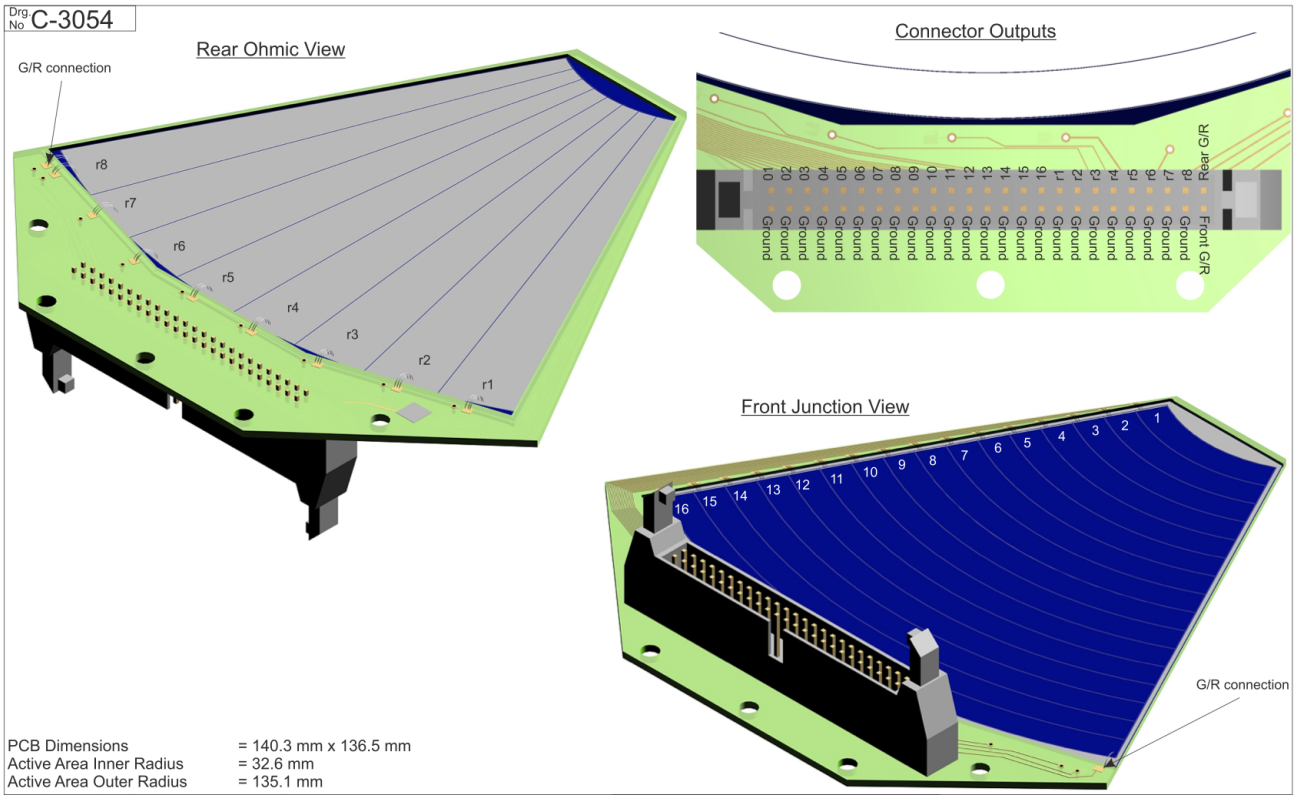

Figure 2.15. Schematic of a Micron Semiconductor Ltd. MMM Si strip detector. The bottom right shows the junction side of the detector, which has 16 annular strips, while the left side shows the ohmic side of the detector, which has eight radially oriented strips. The top right shows the signal pin out scheme for the detector. Reproduced from [39].

ulation while Appendix B is an instruction manual on its use.) These simulations also helped to determine the optimal distance at which the array should be placed from the target for the best geometric efficiency. The simulation describes the geometry of the detectors in relation to the target and the SPS aperture; it also takes the parameters of the simulated reaction of interest as input. It then simulates a specified number of events of the reaction of choice and determines how many decay events are seen in SABRE in coincidence with a hit in the focal plane detector. This then gives a calculated geometric efficiency for the array for a given reaction and subsequent particle decay. For example, the efficiency of a 100% branching ratio, $l = 0$ isotropic alpha decay from the 12.049-MeV state in ^{16}O to the ground state of ^{12}C is simulated to have a geometric efficiency of 30.2(31)% (an explanation of the uncertainty and details of the simulation are discussed in detail in Chapter 3). SABRE also has a larger range than YLSA to measure angular distributions, covering from roughly 105° to 165° in theta.

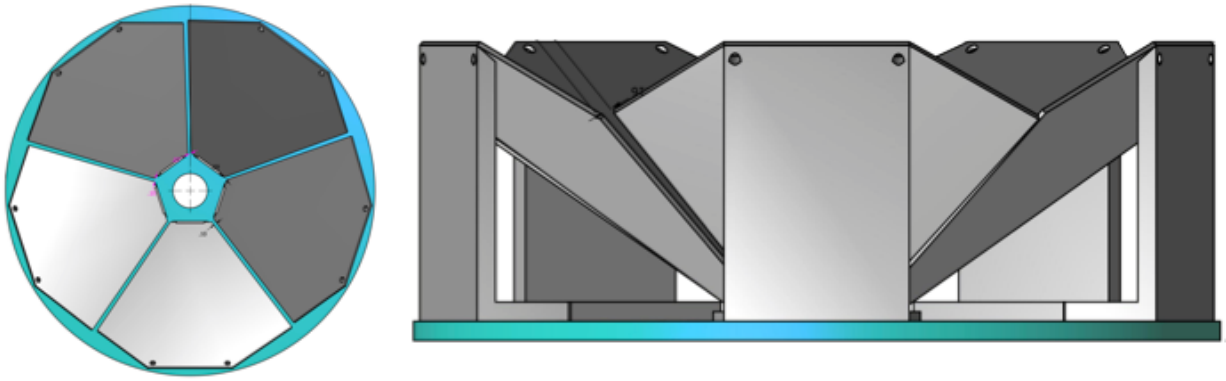

Figure 2.16. Design of SABRE, as rendered in CAD. On the left is a view looking back at the array from the target, and the right shows a side view of the array and mount. On the left, the MMM detectors are grey while the mount is blue. On the right (side view), the mount consists of the blue base and grey L-shaped pieces, while the MMMs are shown in their lampshade configuration.

SABRE and its mount were designed in the Summer of 2015 guided by these Monte Carlo simulations of geometric efficiency, which were completed by the beginning of that September to allow for enough lead time for detector fabrication. The thick dead layer detectors were received in August 2016 and were tested at the end of that September; the initial detector parameters can be seen in Table 2.2. The mount was manufactured in Fall 2016 and tested for fit with the detectors

Table 2.2. Initial test values at +60V bias for the thick dead-layer MMM detectors for SABRE, taken in September 2016. Detector thicknesses are values quoted from Micron Semiconductor, Ltd. Si detectors act as reverse biased p-n junctions, with bias depleting the active detector region; leakage current is the small amount of current that continues through the detectors.

Detector	Thickness	Leakage Current
2954-13	407 μm	0.28 μA
3149-6	419 μm	0.16 μA
3149-15	416 μm	0.16 μA
2954-9	402 μm	0.40 μA
2954-16	404 μm	0.24 μA

Table 2.3. Initial test values at +50V bias for the thin dead-layer MMM detectors for SABRE, taken in July 2019.

Detector	Thickness	Leakage Current
3264-11	503 μm	0.44 μA
3264-13	509 μm	0.40 μA
3264-16	504 μm	0.58 μA
3264-17	502 μm	0.36 μA
3264-18	500 μm	0.56 μA

that December, as seen in Fig. 2.17. After ascertaining the viability of the design assembled with the MMM detectors, SABRE was installed in the target chamber at FSU in October 2018, shown in Fig. 2.18, and tested with an alpha source and conventional electronics. While the main goal of this test was to make sure the array fit in the chamber and to fine tune the mount to be aligned with the beam, we were able to see that the detector array worked with conventional electronics in the final setup, as shown in Fig. 2.19. The thin dead-layer detectors were received in August 2018 and were tested in July of 2019, the results of which are given in Table 2.3.

2.5 Digital Electronics for SABRE and the Focal Plane Detector

One of the goals of the new SPS setup was to have the ability to measure lower particle decay energies in SABRE, which are important for some astrophysical reactions as discussed in Chapter 1. In previous experiments conducted at the WNSL, one of the limiting factors was the use of conventional electronics to process signals coming out of each Si detector in YLSA; the lower energy threshold for a 2008 experiment was 445 keV [29]. Digital electronics have allowed us to measure lower energy signals in the Si detectors down to roughly 190 keV, as discussed in Chapter

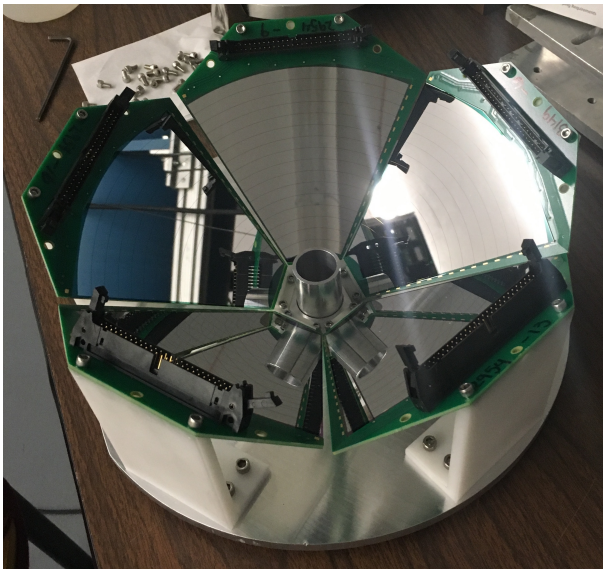

Figure 2.17. Photo of the SABRE mount with all five MMM detectors in place.

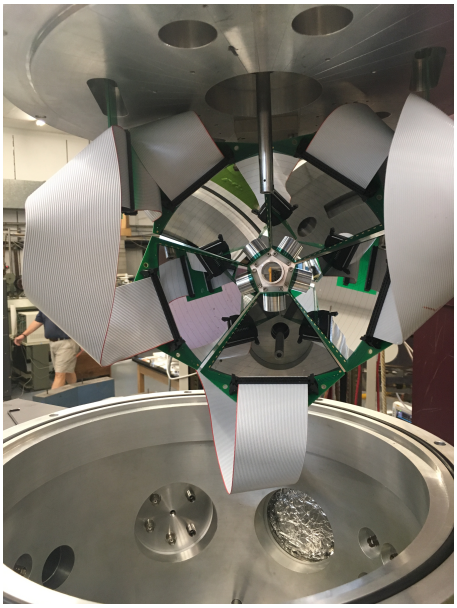

Figure 2.18. Photo of the SABRE array in position, mounted to the target chamber lid with detector cabling in place.

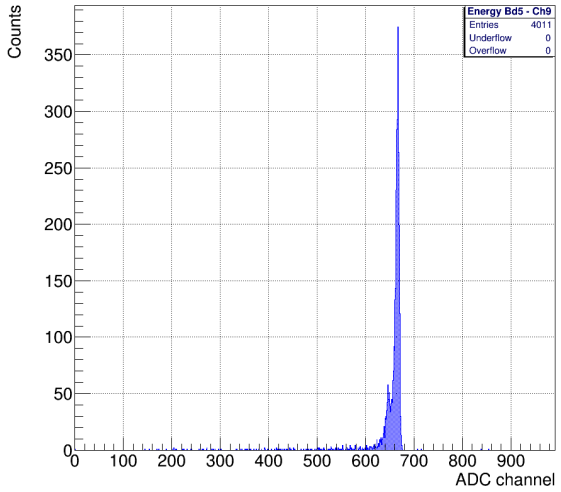

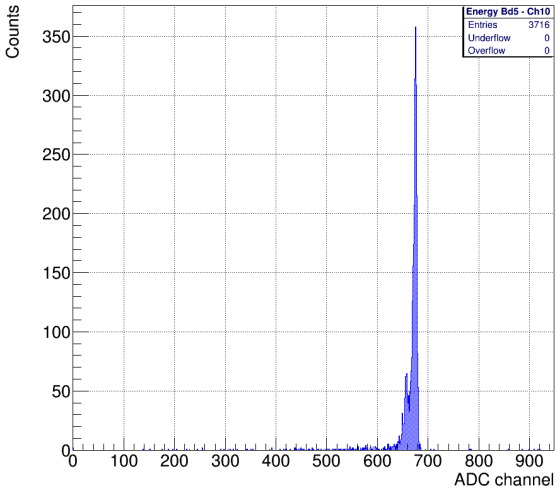

Figure 2.19. Spectra from an alpha test using a ^{241}Am source and conventional electronics in October 2018 after SABRE was installed in the SPS target chamber. Both signals are from the same detector; the left is junction channel 9 and the right is junction channel 10.

3.

In general, there are many advantages to using digital electronics [40]. For example, they have a low dead time during acquisition due to online processing of pulse shapes, leading to higher al-

lowable counting rates. By analyzing pulse shapes in software versus the traditional analog method of processing in the physical modules before storing, time processing signals is saved. Some other advantages of digitizers are that they have a much wider dynamic range than conventional electronics; they allow for better correction of pileup than conventional; and the noise correction is better with digitizers. The major disadvantage is the sheer volume of data collected by digitizers; the raw data rate of our 144 channel setup is around 4 GB for one 5 minute run of beam on target (^{3}He beam on ^{27}Al) with low thresholds. To minimize the recording of noise in the data stream, a good triggering scheme is required to select the relevant waveforms to store, which will be discussed in detail below.

Compared to conventional electronics, digitizers require fewer electronics modules. Whereas a conventional setup (e.g. shown in Fig. 2.20) would take a preamplifier signal, send it through a shaping amplifier, and then into an Analogue-to-Digital Converter (ADC) to be processed into a digital signal before being saved, as well as generating a trigger for the data acquisition system (DAQ), a digitizer processes the waveforms directly from the preamplifier signal output with its firmware. The most basic scheme for digitizer electronics can be seen in Fig. 2.21.

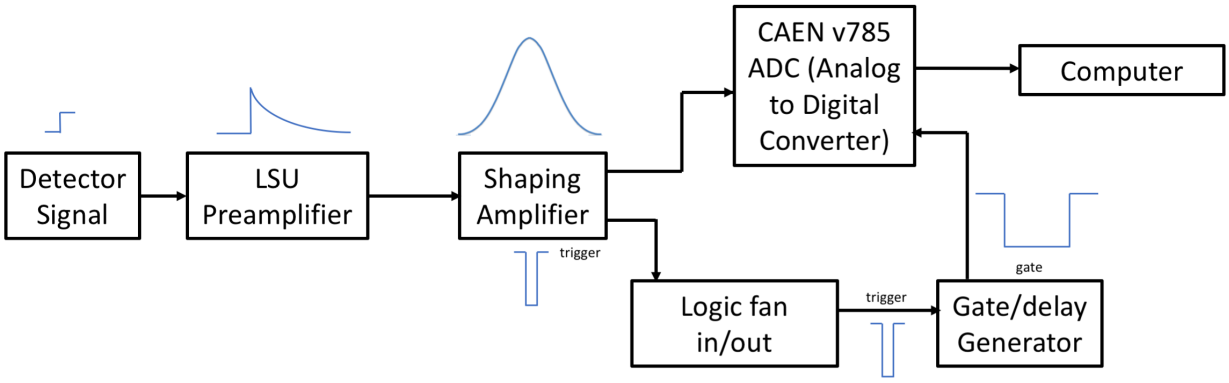

Figure 2.20. A traditional electronics processing scheme for a silicon detector array, with signal shapes shown near modules. The data is transferred from the CAEN ADC to the computer via a VME crate controller that then transfers the data through an ethernet cable.

The SABRE signals are fed out of the target chamber via printed circuit board feedthroughs designed to match LSU-designed preamplifier boxes [41]. The preamplifiers consist of charge-sensitive amplifiers with 27mV/MeV gain and resistive feedback [42]; they amplify the detector

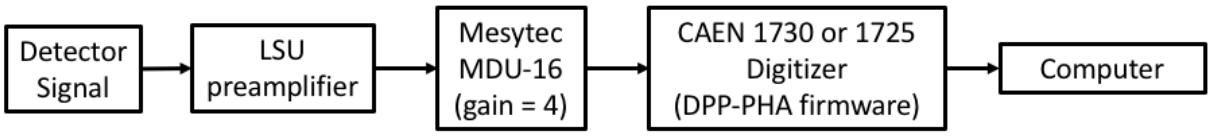

Figure 2.21. A digitizer electronics processing scheme for a silicon detector array. Note that data is transferred directly from the CAEN digitizer to the computer via a fiber optic cable, which also differs from conventional electronics (as described in Fig. 2.20). See text for additional details.

signals and provide voltage to the Si detectors in the array. After preamplification, the signals are processed in Mesytec MDU modules; these are differential linear amplifiers optimized for the output from charge-sensitive amplifiers like those used in the preamps (the preamp output is not, however, differential). The MDUs have an adjustable gain common to all sixteen module channels from 1/8 to 16, and convert ribbon cable inputs to lemo outputs, which makes the conversion to the MCX input required for the CAEN digitizers simpler. Lemo to MCX cables then take these output signals from the MDUs to the inputs of the digitizers.

A mixture of CAEN v1725 and CAEN v1730 modules that utilize CAEN's in-house DPP-PHA (digital pulse processing pulse height analysis) firmware were chosen as the digitizers for SABRE. The digital pulse processing method utilized in CAEN's proprietary DPP-PHA firmware uses a trapezoidal filtering algorithm, which is described in detail in Ref. [43], and works by converting the preamplifier pulse into a trapezoid. The energy of the pulse can be extracted from the height of the trapezoid. By altering different values that parameterize the trapezoid in the PHA firmware, one can achieve the best possible resolution for the resulting energy signals [40, 43]. These include the amount of baseline smoothing, the trapezoidal rise time, the trapezoidal flat-top time, the length of the sampling time (the sample is taken during the flat top with the trapezoid height giving the energy), and the location on the flat top where the sample is taken. These quantities are shown in relation to the signal in Fig. 2.22. Once the DPP-PHA onboard firmware processes a pulse, it records channel number, board number, energy, and timestamp information.

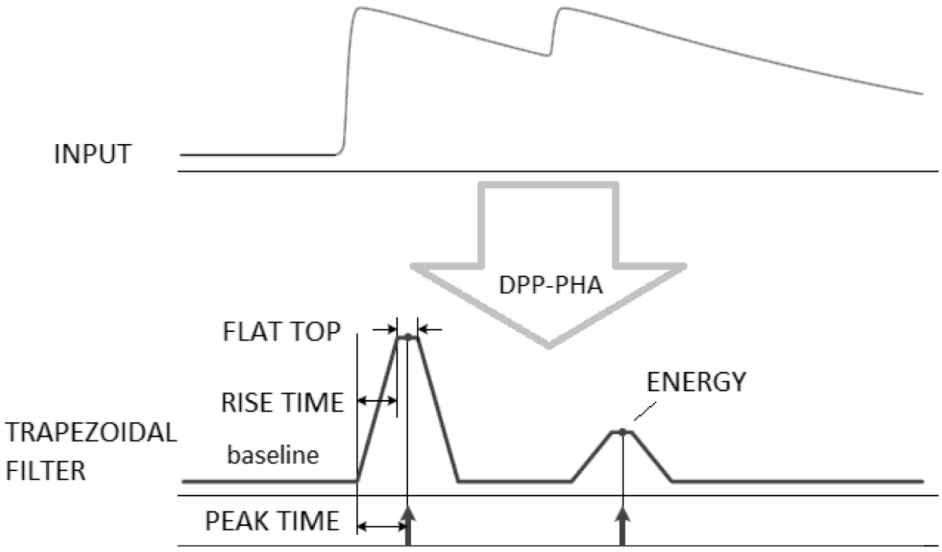

Figure 2.22. Schematic of CAEN's DPP-PHA trapezoidal filtering algorithm. The INPUT line shows an example signal, while the TRAPEZOIDAL FILTER line shows the various filter parameters. Reproduced from [44].

To get the digitizers to save information to our original data acquisition system, the National Superconducting Cyclotron Laboratory Data Acquisition System (NSCLDAQ), a custom package was written by Ron Fox (NSCL, CAEN) to incorporate the CAEN digitizers seamlessly into the NSCLDAQ acquisition process. Ron Fox and Sudarsan Balakrishnan (LSU) spent significant effort to get the two systems to communicate effectively and efficiently. The full NSCLDAQ with digitizers was tested with SABRE in June 2019; aside from some missing components (e.g. too few lemo to MCX cables to get all the signals from the MDUs to the digitizers), it was a successful test. A large portion of the SABRE signals were successfully processed in the NSCLDAQ digitizer setup to create the ^{228}Th alpha decay spectrum in each channel, as shown in Fig. 2.23.

In August of 2019, an attempt was made to test the merging of SABRE's digitizer data ring with the focal plane detector's conventional electronics data ring via the $^{14}\mathrm{N}(d,t)^{13}\mathrm{N}^{*}(p)^{12}\mathrm{C}$ reaction. Unfortunately, NSCLDAQ was unable to handle the data rates encountered during this task, so the problem was circumvented by upgrading the focal plane detector from conventional to digital electronics. That way CAEN's CoMPASS software could be used to process all the data coming in

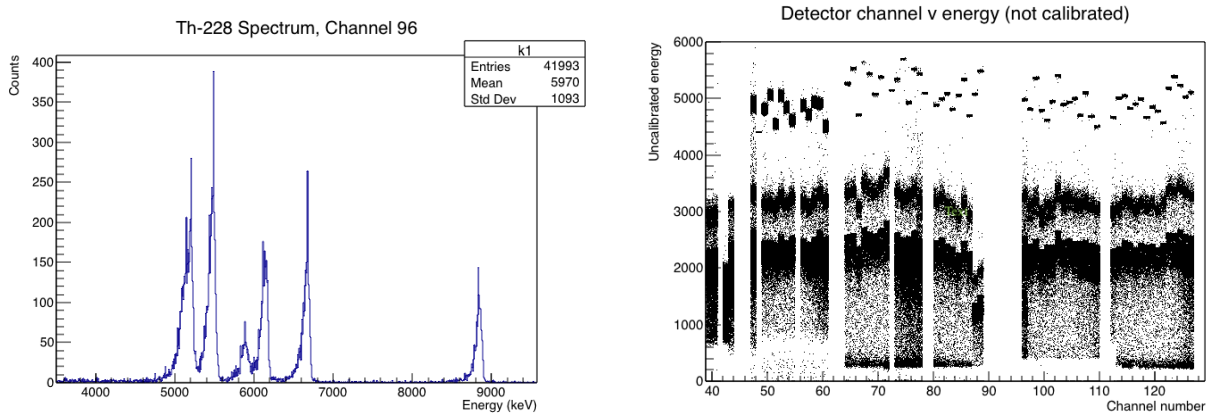

Figure 2.23. Two alpha spectra from a test with a ^{228}Th α source in June 2019 using the full SABRE array and digitizer electronics. The left is an energy calibrated spectrum from a single channel in the SABRE array, read out into NSCLDAQ. The right shows all channels in the SABRE array. The channels are uncalibrated, and therefore there are variations in the recorded energies. Additionally, several cables were missing, resulting in the gaps in the data.

at once with the same system. This also allows for a very straightforward syncing of timestamps between SABRE and focal plane detector events without the merging of two data streams, which is crucial to determine coincidence events between the two detector systems. NSCLDAQ could not be utilized in this configuration as it could not support the high data rates coming in and did not yet support the CAEN firmware needed to digitize the focal plane detector (discussed below).

The focal plane detector's electronics vary from channel to channel, but most signals are preamplified in single channel modules and then all signals are sent to a single CAEN v1730 digitizer. Because of the speed of some of the signals it processes, particularly the scintillator signals, the focal plane detector digitizer utilizes CAEN's proprietary DPP-PSD (digital pulse processing pulse shape discrimination) firmware. (Some signals may be compatible with DPP-PHA firmware, but a board can only support one type of firmware.) DPP-PSD firmware utilizes a digital-charge-integration constant fraction discriminator (CFD) to create long and short timing gates around the signal; it also generates a trigger and a timestamp signal. The short gate is used primarily for pulse shape discrimination between gamma rays and neutrons (as neither are charged particles detectable in the focal plane detector, this feature is not relevant here), while the long gate integrates the pulse and outputs a signal proportional to the total energy collected. A recorded pulse in the

DPP-PSD firmware is saved with short gate, long gate, timing, and board and channel number information. As discussed above, the focal plane detector currently outputs left and right scintillator anode signals from the photomultiplier tubes attached to the scintillator bar, energy signals from the front and rear anode wires in the gas-filled detector, high- and low-rigidity position (or timing) signals from the front and rear anode wire setups, and a cathode signal. The DPP-PSD firmware saves both the timing and energy information from each signal. This provides many more energy loss signals from the focal plane detector than were previously available with conventional electronics as that scheme would have required many more modules to process the additional energy signals. Although there are a variety of different signal shapes and lengths, the variable baseline smoothing, timing adjustments, and different CFD ratios that can be applied to each channel individually allow for satisfactory processing of all types of focal plane detector signals. More detailed information on CAEN's DPP-PSD firmware can be found in Ref. [45].

CAEN's CoMPASS software can run all the digitizers with both types of firmware together, but running successfully with the high rates in SABRE that result from the low thresholds required to detect low energy particle decays requires very specific running conditions, as the digitizers would freeze and stop transmitting data consistently with raw rates above ~10 kHz per channel due to their buffers filling up too quickly. In order to reduce the rate of data that the digitizers process, the following scheme was used. First, the digitizer clocks are synchronized via the TRG OUT-SYNC IN mode; this is a specific way of chaining the digitizers' clocks from the TRG OUT port to the SYNC IN port on each digitizer, shown by the green arrows in Fig. 2.24. This requires an external TTL signal to start a run, which was implemented by pressing the physical start button on a Lecroy 222 NIM Dual Gate and Delay Generator module (this is connected to the parent board, shown by the blue arrow in Fig. 2.24). In CoMPASS, the focal plane digitizer board is set to a "global OR" triggering mode (meaning that each channel can individually trigger itself), while the SABRE digitizers run on a "TRG IN level gate" triggering mode. This means that the recording of SABRE events is triggered once a validation pulse is fed into the physical TRG IN port on the digitizer from an externally generated gate, explained in more detail in the following paragraph. This gate

is created by the scintillator signals at the focal plane, as shown by the purple arrows in Fig. 2.24, via a "mask" applied in the boards' firmware. This mask allows only scintillator signals to trigger from the "TRG OUT" lemo port. Because the SABRE and scintillator events are the fastest events captured in the system, this gate records only meaningful SABRE coincidences.

The SABRE boards must have a "coincidence window" or "TRG_REQ" (trigger requirement) set in the firmware to validate the external trigger. This "TRG_REQ" was set to 496 ns, and allows for an external trigger to validate the event to be recorded if the external trigger comes within this window, shown in Fig. 2.25. Another important implementation is the trigger holdoff (a window of time in which the board is unable to re-trigger after it has initially been triggered to record an event) of 1 μs on the SABRE boards. The trigger holdoff is set to equal twice the length of the "coincidence window" to avoid double coincidences, as suggested in Ref. [46]. An example of how the external gate and trigger holdoff works in relation to SABRE signals for one channel is shown in Fig. 2.25. When this scheme is paired with a pileup rejection algorithm (an option in CoMPASS that must be selected) in the SABRE boards' firmware, it allows the boards to reliably accept raw trigger rates of up to 10 kHz per SABRE channel (or more) while recording only gated events of interest. The threshold on the SABRE boards can be adjusted individually for each channel in CoMPASS to allow lower energy signals, but this does increase raw event rates. Additionally, different beam on target combinations will have higher or lower raw trigger rates (this mostly depends on target Z, target thickness, and beam intensity, but the quality of the beam tune can play a role).

Files are recorded in binary (as opposed to the more processed ROOT files, discussed below) in CoMPASS in order to reduce the load on the RAM of the computer. This data is saved in a simple form, with just the board number, channel number, energy, timestamp, and CoMPASS flag saved for each event. Event building is done in post processing via event timestamp, discussed in more detail in Chapter 4.1.

With the development of SABRE and the CAEN digitizer system's implementation to the detectors of the SPS, a benchmark was needed to ensure the proper functionality of the experimental

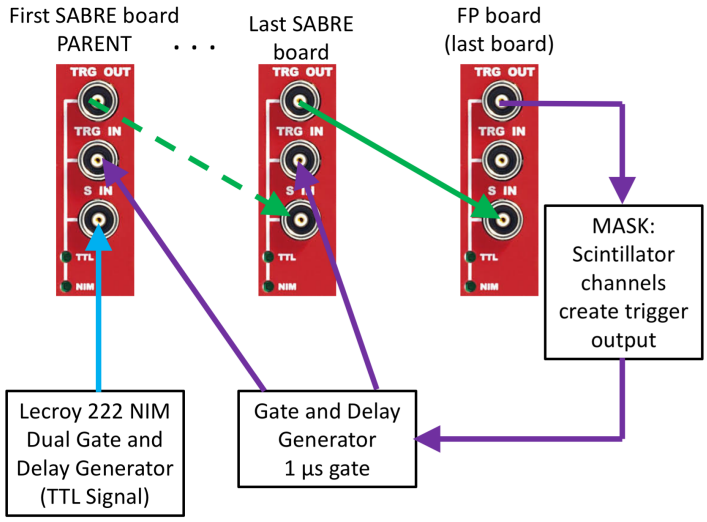

Figure 2.24. Digitizer cabling scheme for the setup described in the text, with the first and last SABRE digitizer boards represented (other boards are inserted where the ellipses are and are cabled similarly) and the focal plane (FP) board being the last in the chain. The green arrows indicate the cabling scheme required to synchronize the run start/stop signal. The blue arrow indicates the input of the external TTL start signal required to start a run in the software. The purple arrows indicate the propagation the external trigger to all the SABRE boards in the setup. Note that the focal plane detector board is last in the chain so that its "TRG OUT" signal can be used for the external triggering. More details in the text.

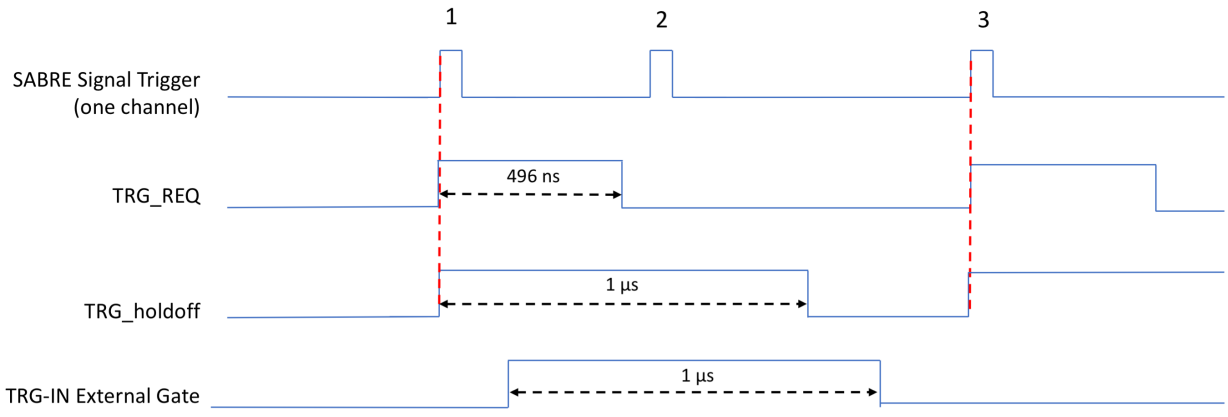

Figure 2.25. Three SABRE signal triggers are shown for one channel (top), with the trigger request (middle top), trigger holdoff (middle bottom), and the external gate (bottom). Signal 1 is recorded as the external gate falls within the trigger request time of the board; a trigger holdoff is also applied. Signal 2 does not get recorded even though it is within the external gate because it occurs during the trigger holdoff for signal 1. Signal 3 does not get recorded due to its trigger request not being validated by an external gate.

equipment. Several experiments were performed to ascertain the performance of the upgraded and newly developed and integrated detectors and electronics, described in the following chapter.

3 Detector Commissioning

To test the performance of the refurbished focal plane detector and new SABRE detector setups, they both underwent commissioning experiments. The reactions performed for these experiments were well-known, previously studied reactions so that the detectors' behaviors could be properly benchmarked.

3.1 Focal Plane Commisioning: Summer 2018

The SPS and focal plane detector setup were commissioned in June of 2018 with the ^{12}C$(d, p)^{13}$C reaction. This involved a deuteron beam of energy 16 MeV impinging on a ^{12}C target that was roughly 200-μg/cm^2 thick, creating excited states of ^{13}C that remained in the target and protons that were momentum-analyzed in the SPS and detected in the focal plane detector. The results of the commissioning can be seen in Fig. 3.1, which shows the ground state and first three excited states of ^{13}C as well as excited states in ^{17}O from the ^{16}O$(d, p)^{17}$O reaction due to oxygen contamination in the target.

The focal plane detector was commissioned with conventional electronics, and did not transition to digital electronics until 2019. The detector had a resolution of about 35 keV during its first runs, comparable to its performance when it was installed at Yale. Resolution of 20 keV was achieved after the implementation of digital electronics.

3.2 SABRE: Fall 2019

To test the capabilities of the fully digitized SABRE system and to ascertain the geometric efficiency of the array, an experiment to measure known α-particle branching ratios of states in ^{16}O via ^{19}F$(p, \alpha)^{16}$O$^*(\alpha)^{12}$C was performed. A 10-MeV beam of protons from the Tandem Van de Graaff accelerator bombarded a 100-μg/cm^2 LiF target on a 20-μg/cm^2 carbon backing. The magnetic field was set to 5.8 kG and the magnet's entrance window was rotated 15° relative to the beam. The aperture of the magnet was open to an acceptance of ±40 mrad in the horizontal direction and full acceptance (±80 mrad) in the vertical direction. The α particles detected in the gas-filled focal plane detector from the (p, α) reaction were used to identify states of interest populated in ^{16}O. Alpha decays from the excited states populated in ^{16}O were detected in the

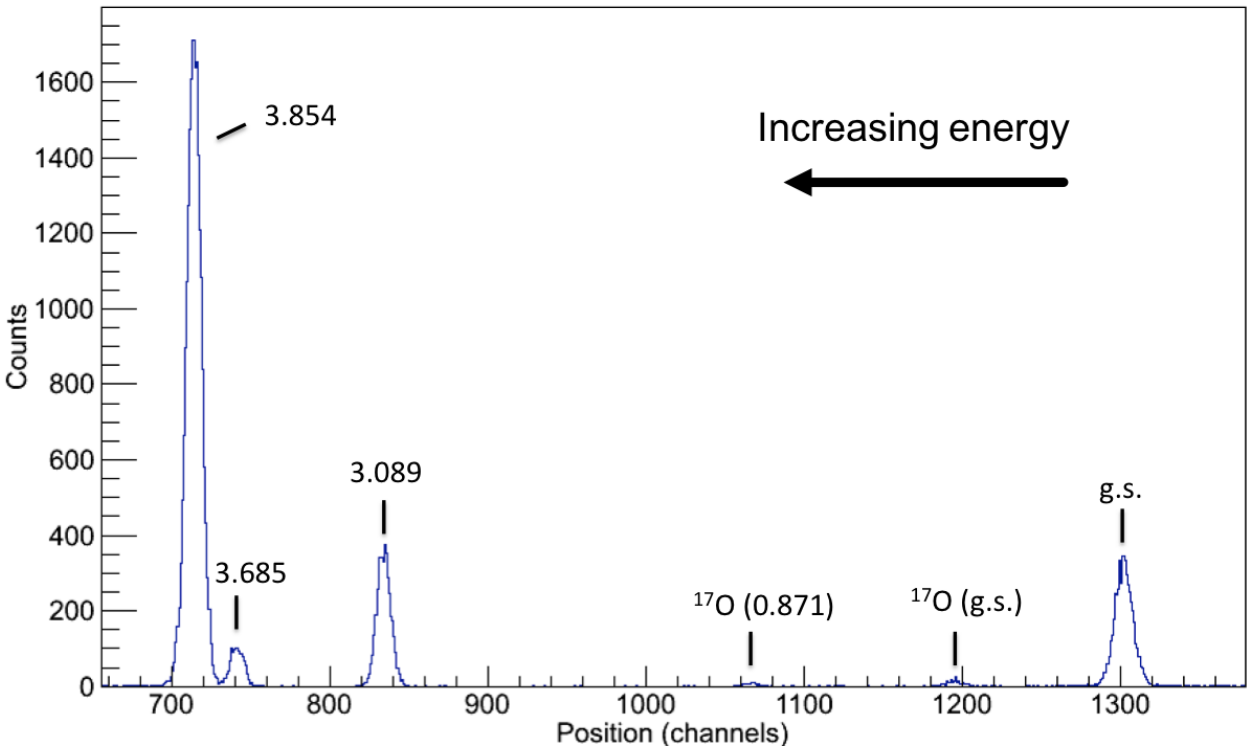

Figure 3.1. Spectrum from the focal plane detector's commissioning run with the ^{12}C$(d, p)^{13}$C reaction. Here the ground state and first three excited states of ^{13}C are shown and labeled as g.s. and their energy levels (in MeV), from right to left. The ground state and first-excited state of ^{17}O are also shown and labeled. This plot shows increasing excitation energy from right to left as the horizontal axis shows position in the focal plane detector, which has not been converted to energy.

SABRE array in coincidence with the alpha particles detected at the focal plane in order to measure branching ratios.

The triggering scheme for the SABRE boards described at the end of Chapter 2 had not yet been applied and was not required as the thresholds were set much higher than those required for the detection of decays from low energy states. The primary differences in the electronics setup were that the SABRE boards were allowed to self-trigger in the same way that the focal plane detector board operates as described in Chapter 2, and thus no external gate was used for triggering. Because there was no external gate, the boards were synchronized in a different configuration, with the TRG-OUT port of the first board being connected to the TRG-IN port of the next, and so on, with the SYNC-IN port not being used. Additionally, there was no external start signal required for this configuration; a software start was sufficient. This simpler configuration works well for runs that don't require low thresholds in SABRE, and is simpler to implement.

In order to identify the states of interest in the focal plane data, some preliminary cuts to reduce background are applied. First, focal plane delay-line times of zero are cut out to eliminate zero-value counts that appear from false triggering. Next, the front and rear wire positions are plotted against each other, as in Fig. 3.2. By gating around the diagonal line in the spectrum, a majority of the noise is eliminated. Alpha-particle reaction products associated with states of interest in ^{16}O can then be identified in the focal plane detector data by plotting front wire focal plane position versus front anode energy (i.e. energy loss), as shown in Fig. 3.3. By selecting the alpha-particle group, a spectrum of excited states populated in ^{16}O can be produced as they are directly related to the position (i.e. the magnetic rigidity) of the alpha particles along the focal plane (Fig. 3.4). One can then identify states of interest in this spectrum and integrate the counts in each peak to get the total number of times a state was observed during the experiment.

Integrating the counts in the peaks of interest in Fig. 3.4 also requires appropriate background subtraction methods. This background arises from broad states in ^{16}O (with widths of several hundreds of keV) in the region of interest, additional alpha particle breakup from the primary reaction (i.e. $^{19}\mathrm{F}(p,\alpha)^{16}\mathrm{O}$), and alpha particles emitted at forward angles from the ^{16}O alpha decay, which

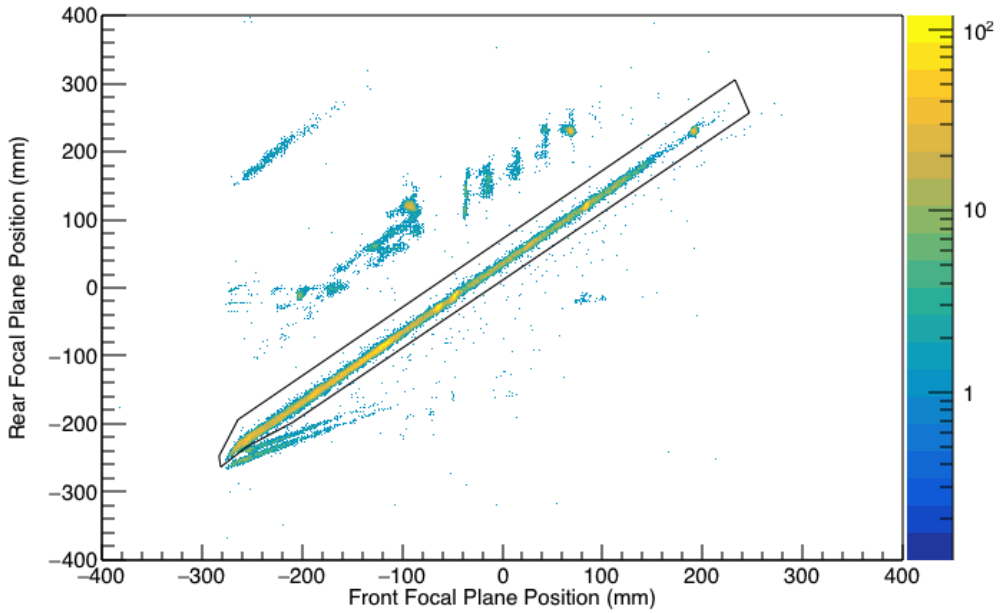

Figure 3.2. Front versus rear focal plane position. A gate around the diagonal line, shown in black, cleans up false triggering noise.

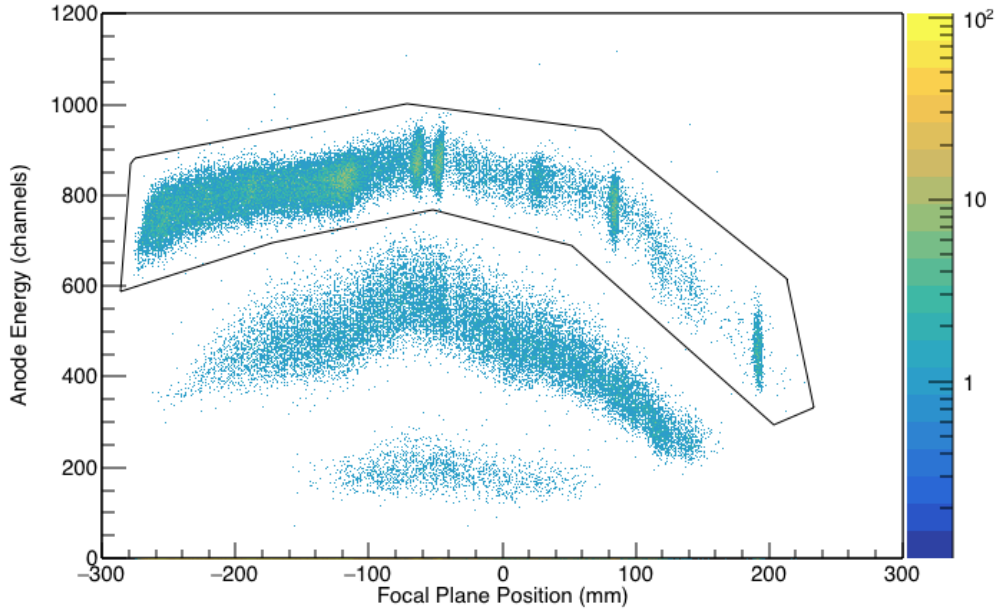

Figure 3.3. Focal plane front wire position versus front wire energy (ΔE). The particle groups shown here are alphas, deuterons, and protons, from top to bottom. A gate (black) is drawn around the alpha particles.

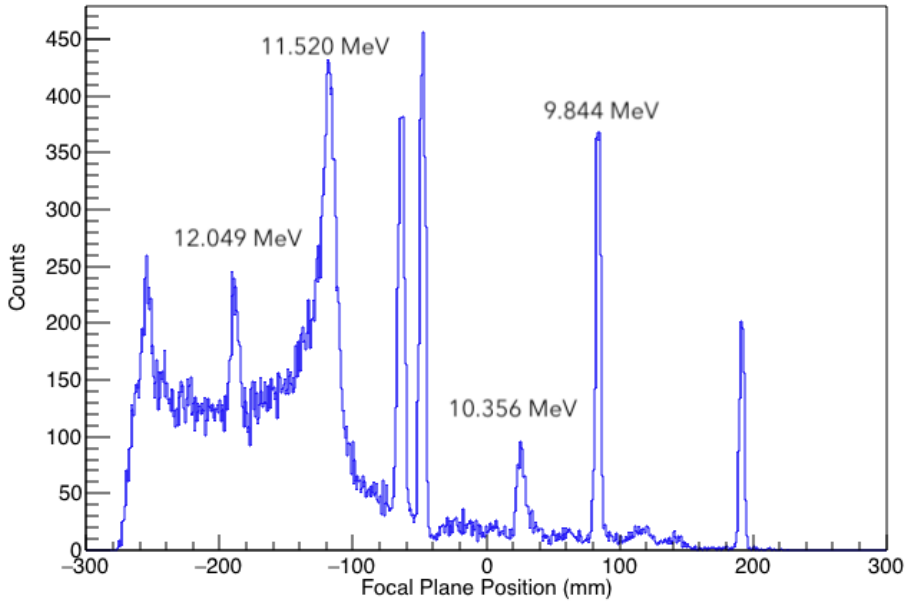

Figure 3.4. A projection of the gated alpha particles (from Fig. 3.3) in the focal plane onto the focal plane position axis. States of interest with 100% alpha branching ratios in ^{16}O are labeled by their energy.

creates a broad energy distribution. For the peaks at 9.844 and 10.356 MeV, this is a straightforward linear background subtraction: (1) integrate the area of the peak comprised of n channels; (2) integrate areas directly adjacent to the peak area on the left and right each comprised of $n/2$ channels; and (3) subtract the adjacent area integrals from the peak area integral. The total uncertainty in the final peak counts using this background subtraction method is calculated via $\sqrt{N + N_L + N_R}$, where N is the raw number of counts in the peak and N_L and N_R are the number of counts in the background on the left and right sides of the peak.

The peaks at 11.520 and 12.049 MeV require fitting the backgrounds to a function and then adding in the Gaussian peak to create a custom fit. First, the background is fit (usually a polynomial of some degree) without the Gaussian peak; the parameters from this fit are saved. Next, the peak itself is fit as a Gaussian distribution and those fit parameters saved. One then takes the background and Gaussian parameters to use as starting points in a combined fit (e.g. Pol2+gaus, etc. in ROOT nomenclature; see Fig. 3.5 for an example) to get the best parameters for the total fit. To evaluate

the best background fit, one can compare the chi-squared values of the different fits. Lastly, the custom fit parameters can be used to integrate the area under the peak: first, integrating a given area with the Gaussian portion of the fit and then integrating the same area with the polynomial portion of the fit. By subtracting the background area determined from the polynomial from the Gaussian area, a background subtracted integral can be found. Similarly to the calculation for a linear background, the uncertainty here is calculated via $\sqrt{N_{peak} + N_{background}}$.

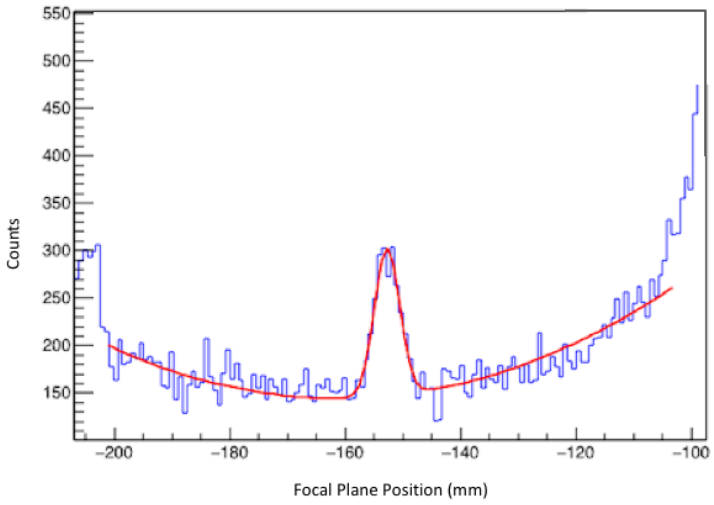

Figure 3.5. An example fit for background subtraction. Here a combined Pol2+gaus fit, in ROOT nomenclature, is shown, which was used to fit the 12.049 MeV state of interest. The red line is the fit as applied to the data.

To determine branching ratios, the position of the alpha particles from the $^{19}\mathrm{F}(p,\alpha)^{16}\mathrm{O}$ reaction along the focal plane is plotted versus the energy deposited in SABRE by the α-decay particles emitted from unbound states in ^{16}O, as shown in Fig. 3.6, and a gate is applied around the diagonal line corresponding to the alpha-decays to the ground state of ^{12}C. These counts can then be projected onto the focal plane position axis as in Fig. 3.7. Similarly to the focal plane data described in the previous paragraphs, these peaks must also be integrated and background subtracted appropriately. For the SABRE-gated focal plane spectrum, the only peak that cannot utilize linear background subtraction techniques is at $E_x = 11.520$ MeV; this is fit to a background function as described in the previous paragraph.

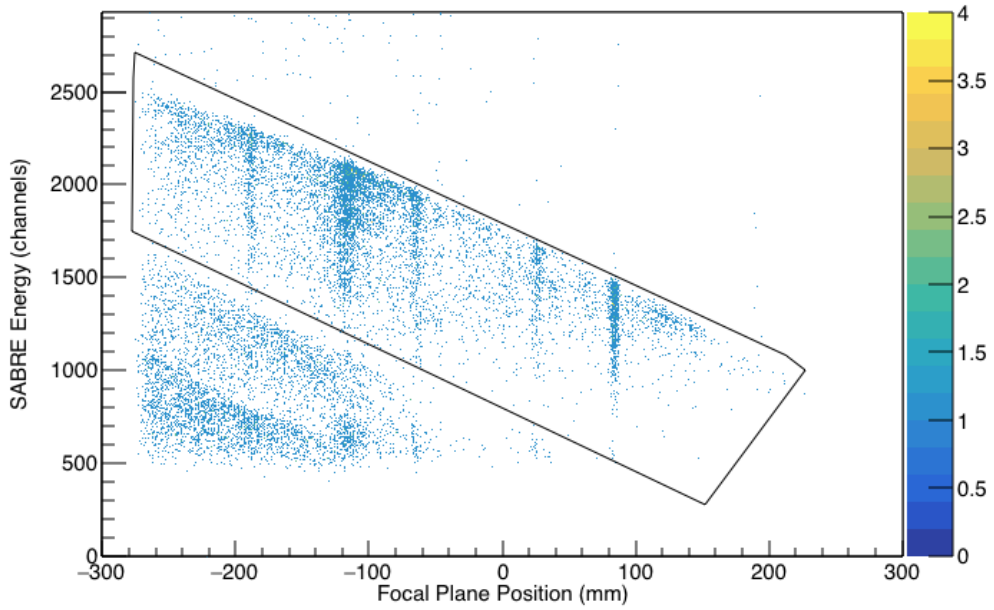

Figure 3.6. Focal plane position versus energy deposited in SABRE. Here a gate (black) is drawn around α-particle decays to the ground state of ^{12}C from excited states populated in ^{16}O; other diagonal lines represent other decay schemes from the reaction. The SABRE energy resolution appears poor due to varying energy loss of alpha particles in the target and the silicon.

By comparing the background-subtracted number of counts in peaks of interest in Figs. 3.4 and 3.7 and correcting for geometric efficiencies, the values for the branching ratios of each unbound state of interest can be found, which can then be compared to the known values of the branching ratios. One then compares two values that reflect the calculated geometric efficiency of the array and the known 100% branching ratio value, respectively.

Here, states in ^{16}O with 100% alpha-particle branching ratios have been measured to compare to a Monte Carlo simulation of the decays into the array. The simulation, discussed in detail in Appendix A, reproduces the reaction of interest into a mockup of SABRE, and allows for a calculation of geometric efficiency. The output also allows for the geometric efficiencies of individual detector strips to be determined, so if certain detectors were missing channels, they can be accounted for. The simulation for this experiment was run for one million events per state of interest and statistical uncertainties were determined by taking the square root of the number of counts. Additionally, the simulation was run four more times to independently vary the distance of the array from the target

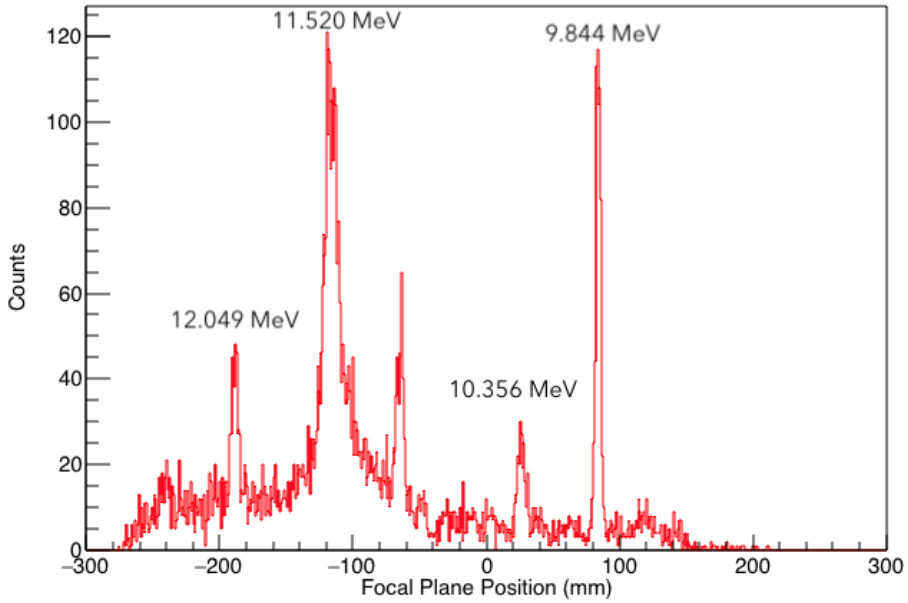

Figure 3.7. Focal plane position of states in ^{16}O gated on α-particle decays to $^{12}C^{g}$ measured in SABRE (as shown in Fig. 3.6). States of interest in ^{16}O with 100% proton branching ratios are labeled by their energy.

by ±5 mm (the variable known as z0 in Appendix A) and to vary the tilt angle of the detectors in the array by ±3 degrees (the variable is known as thetaYLSA or incline in Appendix A). This process was used to account for systematic uncertainties in measurements used by the simulation; the absolute value of the the largest differences of the tilt and z0 variation from the original were added to the statistical uncertainty of the calculation in quadrature to account for uncertainties in the simulation as described in the last section of Appendix B. These are the uncertainties given in column two of Table 3.1. The values of both the measurements and the Monte Carlo simulation findings are shown in Table 3.1. The uncertainties given for the measured values in column three are purely statistical.

Comparing the measured branching ratios of excited states in ^{16}O (not corrected for geometric efficiency) to the geometric efficiency of the array calculated in the simulation, seen in Table 3.1, one finds that there is generally good agreement between the values within uncertainties. The 11.520-MeV state does have the disadvantage of sitting on top of an 800-keV wide state at 11.6

Table 3.1. States in ^{16}O with 100% alpha branching ratios measured in this experiment. Here a Monte Carlo simulation of SABRE's efficiency (i.e. branching ratios reported in [47] not corrected for simulated geometric efficiency) is compared with the measured values of the branching ratios without corrections for geometric efficiency applied.

	Branching Ratio Not Corrected for Geometric Efficiency	
Excitation Energy	Calculated	Measured
9.844 MeV	27.2(32) %	31.5(14) %
10.356 MeV	25.7(19) %	25.6(33) %
11.520 MeV	25.0(26) %	28.7(14) %
12.049 MeV	30.2(31) %	31.5(46) %

MeV; this makes the background subtraction more difficult, and the simulation does not account for this state that also has a 100% branching ratio with a different spin parity.

As the branching ratio comparisons agree within uncertainties, SABRE is shown to perform as expected. Upon the successful completion of the commissioning experiments described here, the full experimental setup has been used for a variety of reaction measurements of interest for nuclear structure and astrophysics, including the ^{26}Al(^{3}He, t)^{27}Si*(p)^{26}Al^{g,m} measurement described below.

4 Data Analysis of ^{27}Al(^{3}He,t)^{27}Si*(p)^{26}Al

The study of ^{27}Si proton branching ratios for the $^{26}\mathrm{Al}^{g}(p,\gamma)^{27}\mathrm{Si}$ and $^{26}\mathrm{Al}^{m}(p,\gamma)^{27}\mathrm{Si}$ reactions was performed using the previously described experimental apparatus at FSU: the SPS with its associated detectors, SABRE and the focal plane detector. The experiment was performed using the $^{27}\mathrm{Al}(^{3}\mathrm{He},t)^{27}\mathrm{Si}^{*}(p)^{26}\mathrm{Al}$ reaction. This involved a 24-MeV ^{3}He beam impinging on a 150-$\mu g/cm^2$ natural aluminum target with a 20-$\mu g/cm^2$ carbon backing. Beam intensities for all runs averaged anywhere between 20 to 30 enA on beam stop 3 (BS3), the closest beam stop to the target. The spectrograph was set at an angle of 3 degrees, and the slits (which set the size the aperture into the SPS) were set vertically to 160 mrad (fully open) and to 60.4 mrad horizontally. The focal plane detector was filled with slowly flowing isobutane gas at 160 Torr. There were runs in late February and late March 2020. The SABRE detectors were installed as shown in Fig. 4.1, with the addition of a shield, not pictured, in front of the target ladder. Additionally, the SABRE mount and target ladder were positively biased at +500 and +350 V, respectively, in all runs.

The experimental data was taken over several runs due to tandem breakdowns during running. The parameters above were the same for all experiments while the parameters detailed below differed for each run.

The February run used the set of thin-deadlayer MMM detectors in SABRE each biased at -60 V, applied to the junction side of the detectors. The magnet was set to 12.63974(1) kGauss. In the camerabox, the scintillator PMTs were biased at -1800 V, the cathode was biased at -770 V, and the anode wires were biased at +1420 V.

The March run used the same set of MMM detectors in SABRE mounted with the ohmic side facing the target, which is the opposite of the February mounting scheme, but were still biased negatively on the junction side at -60V. The anode wires were biased at +1420 V and the cathode was biased at -700 V. It is likely that the scintillator PMTs were still at -1800V. The magnet was set to 12.64076(1) kGauss, which, while close to the previous magnet setting, shifted the location of states on the focal plane detector relative to the February data set.

While the analysis described below is similar to that described for the commissioning of

Figure 4.1. SABRE and target ladder as installed in the target chamber with the lid lifted. A shield is installed after the SABRE array and the target ladder and is not pictured here.

SABRE in Chapter 3, there are differences in the data sets that require different analysis techniques. In particular, the eventbuilding process was streamlined for the different data acquisition running mode and the implementation of low thresholds required additional cuts to clean out background.

4.1 Eventbuilding

The data was recorded using the CAEN CoMPASS software, which is designed to work with the CAEN digitizers, in a scheme described in Chapter 2.5. This is an event-recording software that saves the data into ROOT trees or binary data identified by board number and channel number corresponding to the digitizers. ROOT is a standard nuclear physics analysis program first developed for use by CERN [48]. Additionally, CoMPASS saves energy, short timing energy gate information for DPP-PSD firmware, timestamps, and flags, which indicate various settings and oc-

currences during data acquisition not used here. Correctly parsing this data structure and building events (i.e. grouping signals that originate from the same beam on target event together) is vital to understanding the data collected.

As discussed above, the data is initially recorded into a minimal, ungrouped structure. The process of transforming this structure into a time-sequenced, grouped format is called "eventbuilding." First, the fastest signals, the SABRE silicon detector signals and the scintillator signals, are shifted forward in time by a specified amount depending on the experiment. This is to make up for the relative delay in the other focal plane signals caused by the delay line chips and the drift time of particles through the gas.

After the data has been preprocessed in this way, the recorded signals are sorted using a built-in ROOT function called indexing. This orders all the recorded signals by their timestamps. Once the signals have been ordered in time, events are built using a coincidence window of 3 microseconds. This groups all signals in this window as a coincident event, and saves them as coincident events in a ROOT data tree that can then be further analyzed.

During the eventbuilding process, the recorded signals' identifiers are also converted from numbered channels on numbered digitizers to labeled channels for various focal plane detector signals and the rings and wedges of specific silicon detectors in SABRE. After this event builder process has occurred, one can start to analyze the physics of the data.

4.2 Focal Plane Analysis

Analysis of data is done by writing scripts processed in ROOT, described above. The first step in the analysis is to look at the focal plane detector signals. The signals associated with the particles of interest (here, the tritons) must first be identified and selected before looking at signals from SABRE. To find meaningful position data in the focal plane detector, which gives information about the excited states populated in the reaction, a position value is created using the left and right side delay line timing signals (which correspond to high and low magnetic rigidity in the focal plane, respectively) for both the front and rear anode wires. This is done by subtracting the low-rigidity side time from the high-rigidity side time and dividing by two. This value is then converted

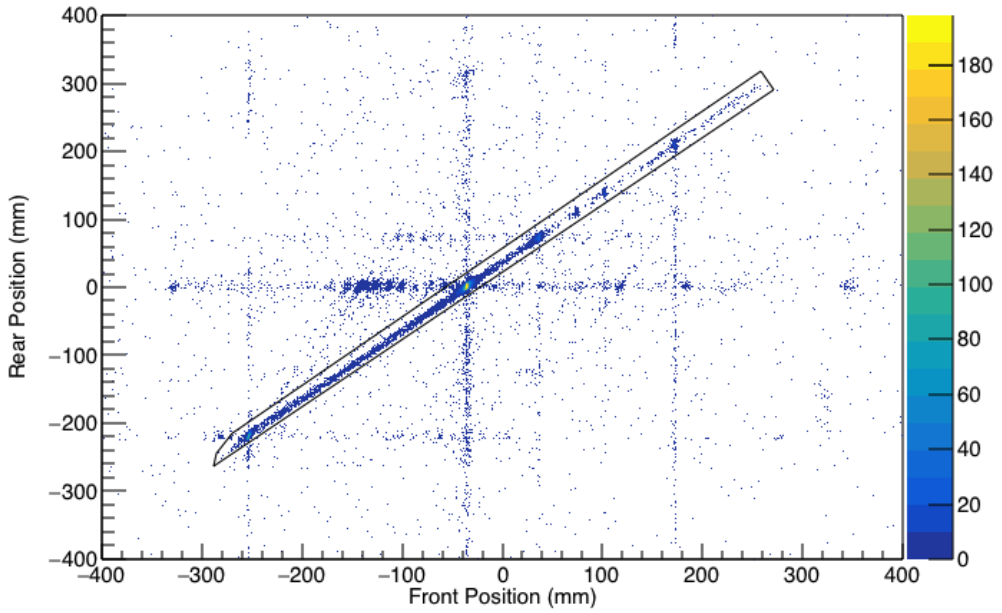

Figure 4.2. Front versus rear anode wire position with a gate (black) drawn around the events of interest for a subset of events. The color scale gives the number of events shown.

to millimeters based on a calibration determined by students at Florida State University that places the center of the focal plane detector roughly at 0 mm. The conversion from ns to mm on the front wire is 0.545 mm/ns and on the rear wire is 0.51 mm/ns. The difference between the two conversion factors is due to the use of different delay line chips in each wire housing; they should be equivalent but manufacturing tolerances allow for some variation.

By plotting the front anode wire position versus the rear anode wire position, many of the recorded signals produced by false triggering can be eliminated (false triggering is quite common on the delay lines due to the low thresholds required to capture the full range of the detector). Figure 4.2 shows the diagonal graphical cut used to eliminate a large portion of the noise recorded in the focal plane.

After the front versus rear anode wire cut has been made, a timing cut is made to select events of interest and eliminate false triggering in the focal plane. In Fig. 4.3 the left scintillator minus the front anode timing has a cut made from -460 to 300 ns to capture the events of interest. While these initial cuts reduce false background signals, the tritons in the focal plane must then be further

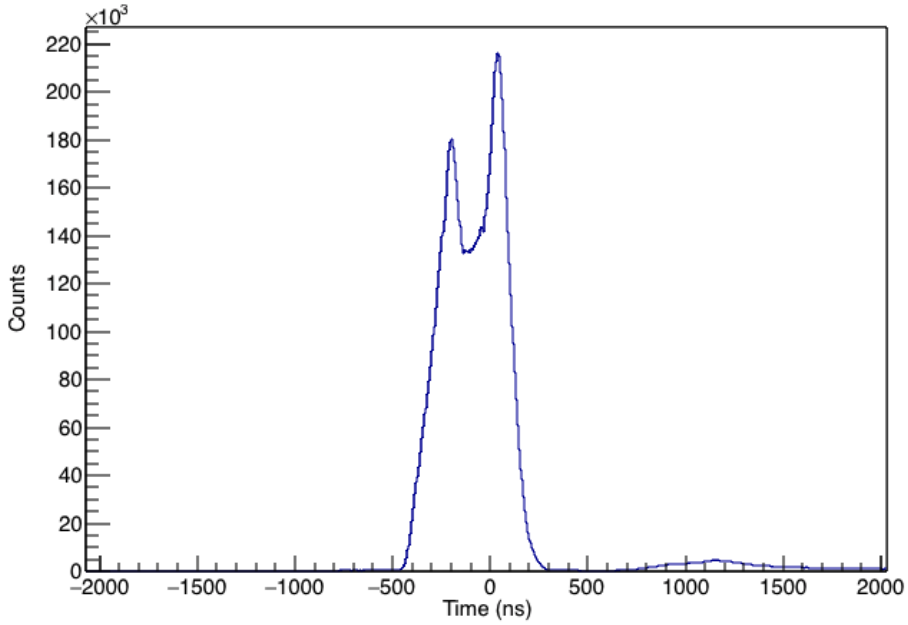

Figure 4.3. Left scintillator time minus front anode wire time. The events of interest are between -460 and 300 ns.

isolated from other reaction particles that are also detected. By plotting the left scintillator (i.e. residual energy) versus the energy loss detected by the rear anode wire, a gate is easily drawn around the triton particle group, as shown in Fig. 4.4. The left scintillator is chosen because the right scintillator PMT was not functioning properly, and the rear anode energy was chosen because the energy loss detected by that wire is relatively constant as a function of position along the focal plane (a large dependence on position was observed for the front anode signal, which is caused by defects in the detector wires).

Once this main triton cut is made, a second cut on a position versus energy loss plot is made to more cleanly discriminate the tritons from deuterons and other particles. Figure 4.5 shows the plot of the left delay line energy versus front wire position before and after the triton cut from Fig. 4.4 is made. A gate is again drawn around the tritons on the left delay line versus position plot, shown in the right of Fig. 4.5, to get a clean position spectrum.

After these gates have been applied, a clean focal plane position spectrum of the tritons in Fig. 4.6 can be seen; each peak in the triton spectrum represents an excited state populated in ^{27}Si by

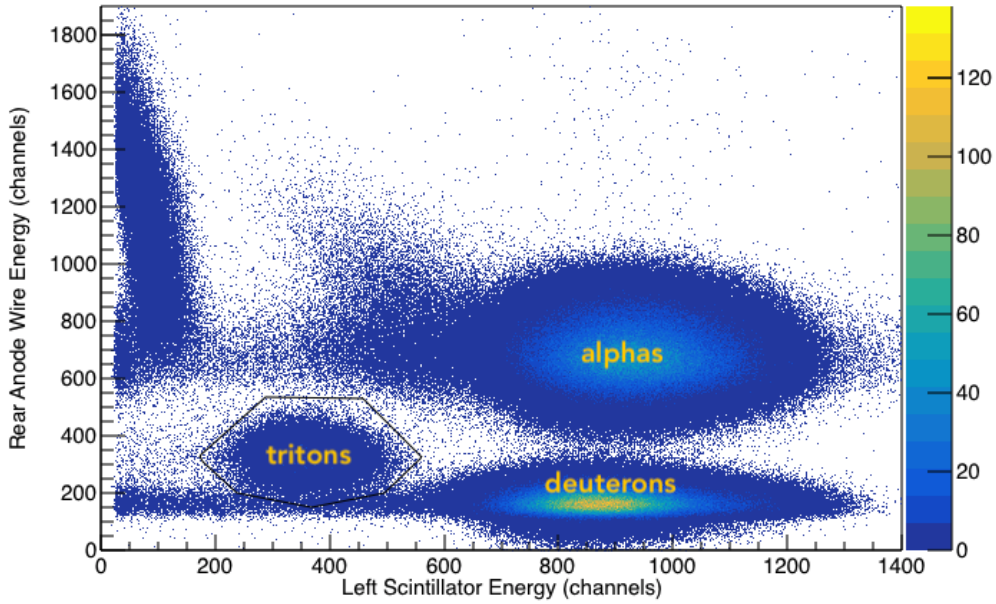

Figure 4.4. Left scintillator energy (i.e. residual energy) versus rear anode wire energy (i.e. energy loss detected by the rear anode wire). This creates one of many $\Delta E - E$ plots that can be used from the focal plane detector for particle identification. A gate is drawn around the tritons (black) and different particle groups are labeled.

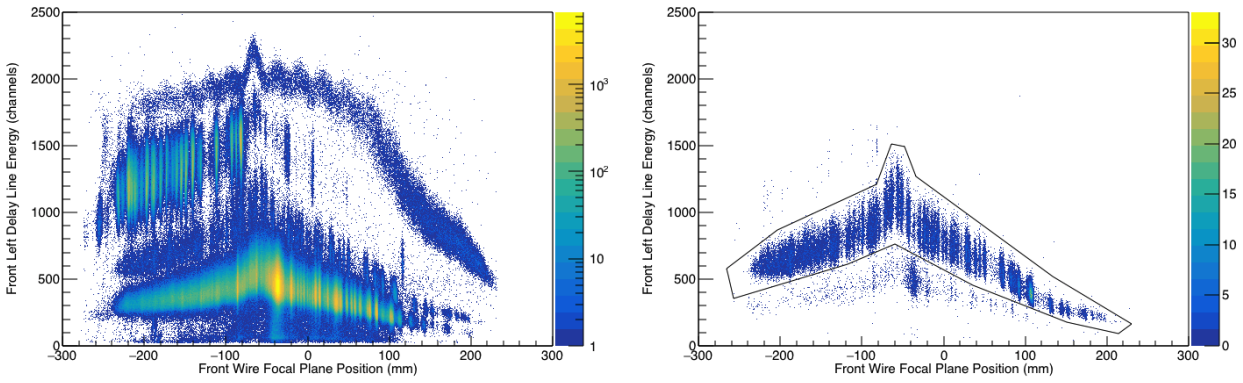

Figure 4.5. Front wire focal plane position versus front left delay line energy (another energy loss signal) in each plot. On the left, the plot is shown before the triton cut shown in Fig. 4.4 is made. On the right, the plot is shown after the triton cut from Fig. 4.4 is applied. The gate shown in the right figure is then applied to eliminate signals from other particle types (in this case, deuterons that are not well separated from the triton group in Fig. 4.4) in the final position spectrum.

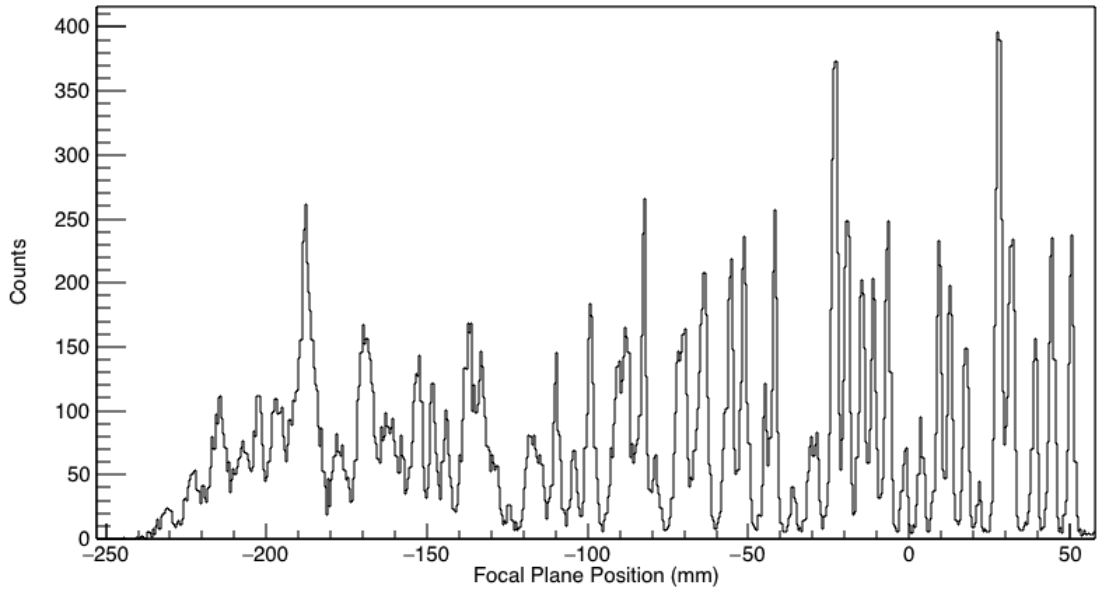

Figure 4.6. Triton spectrum (or equivalently, the ^{27}Si excitation energy spectrum) in the focal plane detector after all cuts have been made.

the ^{27}Al(^{3}He, t)^{27}Si reaction.

The focal plane was calibrated using the Java program Split Pole ANalysis Code (SPANC) [30]. SPANC takes the position centroids and excitation energies (with their respective uncertainties) of known peaks to create a calibration (between position and excitation energy) to calculate the energies of unknown peaks. The calibration was done using a 20-$\mu g/cm^2$ carbon target and the intrinsic oxygen contamination within it. The calibration peaks used were the the ground state of ^{11}C from the ^{12}C(^{3}He, α) reaction, the ground and first-excited state (E_x = 2.3649 MeV) of ^{13}N from the ^{12}C(^{3}He, d) reaction, and the ground and first-excited state (E_x = 0.4953 MeV) of ^{17}F from the ^{16}O(^{3}He, d) reaction. The fit from SPANC had a p-value of 0.9947 and was a third-order polynomial. The same spectrum as Fig. 4.6 with this calibration applied is shown in Fig. 4.7. This calibration was used to guide the excitation energy assignments of states with previously measured data from Ref. [29]. That reference also studied the ^{27}Al(^{3}He, t)^{27}Si reaction to assign energies to states in ^{27}Si, but did not use that reaction to study branching ratios as this work did. Because Ref. [29] had more calibration reactions, their determination of energy levels was used as opposed

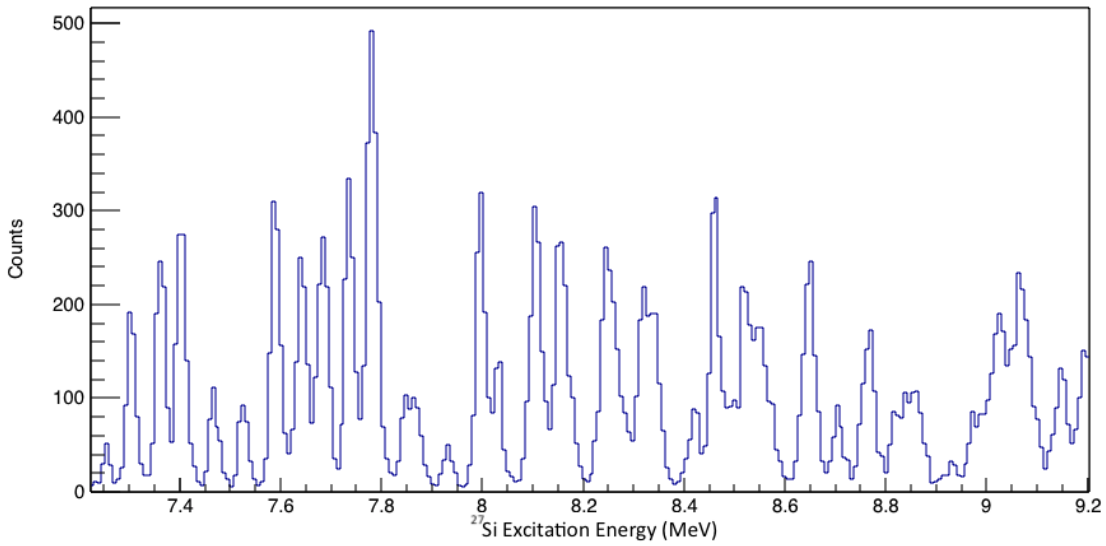

Figure 4.7. Calibrated ^{27}Si excitation energy spectrum in the focal plane detector after all cuts have been made.

to the calibration done from this work.

4.3 SABRE Analysis

After all the focal plane cuts have been applied to the data, SABRE analysis begins by calibrating the SABRE signals. The February run's SABRE signals were calibrated to the 5.846-MeV alpha-particle decay peak from a ^{241}Am source installed in the target chamber using a simple $E = x * [\text{channel}]$ equation, where x is the calibration factor. The March data was calibrated using the 5.423, 5.685, 6.288, and 6.778 MeV peaks from the alpha-particle decay of a ^{228}Th source. The highest energy peak above 8 MeV was cut off due to the choice of energy scale in the detectors. This calibration was completed using a linear fit, $E = a * [\text{channel}] + b$, for each detector channel, where a and b are calibration factors determined by the fit.

Once the calibration is applied, a cut is made on the coincidence time between signals in SABRE and the focal plane detector. In Fig. 4.8, the left scintillator time minus the SABRE ring (or junction side) time is shown; the events of interest are in the narrow peak which lies on top of a linear background coming from random coincidences.

Once this timing cut has been made, the front wire position of the focal plane versus energy

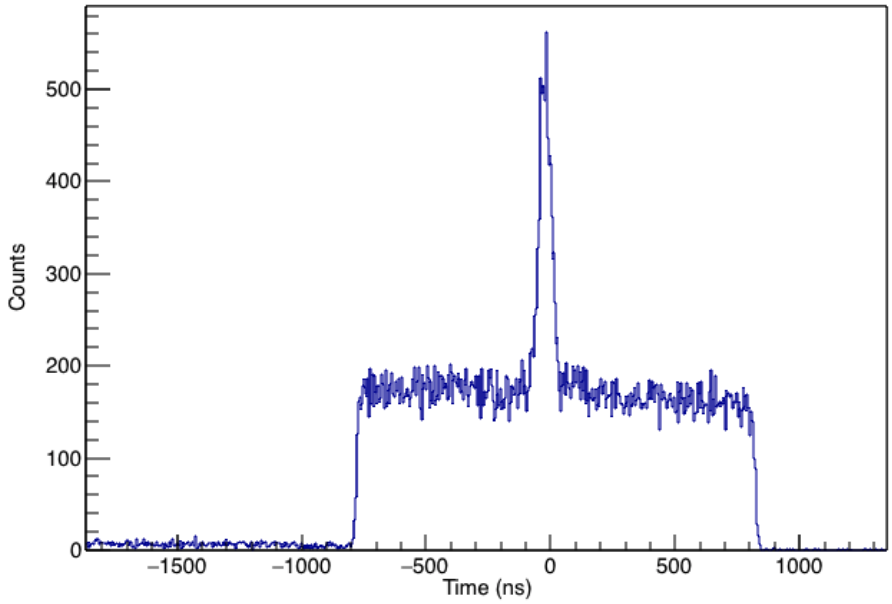

Figure 4.8. Left scintillator time minus SABRE ring channels time. A gate is made around events of interest from -100 to 40 ns, while the SABRE background is determined from channels -170 to -100 ns and 40 to 110 ns. Note that SABRE timing is calibrated in the eventbuilding process for individual digitizer boards and corrected with a constant offset.

measured in SABRE for each event selected is plotted (note that all the previously discussed focal plane detector cuts are still applied). This plot (Fig. 4.9) shows characteristic diagonal lines in the data, which represent different states that the protons decay to in ^{26}Al. Here the ground, isomer, and second-excited states are represented. By drawing a gate around the ^{26}Al state of interest and projecting the selected counts onto the x-axis, one can easily see which states of ^{26}Al are populated by decays from the different excited states of ^{27}Si, as shown in Fig. 4.10.

4.4 Data Set Combination and Branching Ratio Calculation

The March data had two different beam tunes which required two different focal plane position calibrations. The February data had a different magnet setting, and so also had to be calibrated separately. Combining these data sets required only aligning the front wire position of each data set together, which was relatively straightforward. Both sets of March data were aligned to the February data by adding a constant to the front wire position; Figs. 4.11 and 4.12 show the alignment of the first set of March data to the February data. Once these constants were applied to the March

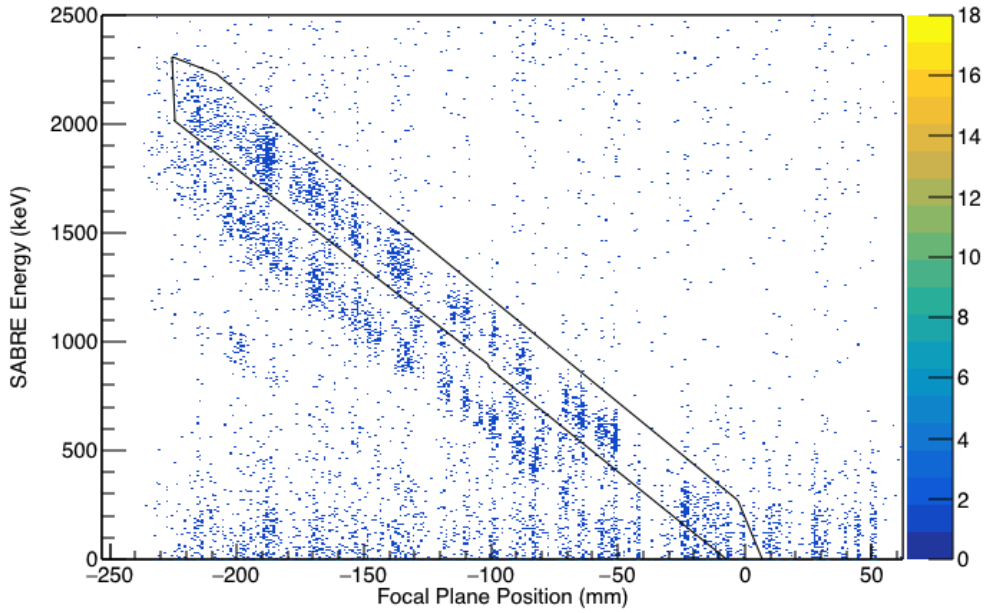

Figure 4.9. Focal plane position versus SABRE energy for the February run with previously discussed focal plane cuts and the timing cut from Fig. 4.8 applied. Note that there are different diagonal lines corresponding to the different states protons decay to in ^{26}Al. Here the ground state has a gate drawn around it. The isomer state is below the ground state and is much more sparsely populated, followed by the second-excited state (E_x = 416.852 keV) below that. The data shown is not background subtracted.

data sets, all the focal plane triton data sets were added as well as those including the SABRE data cuts.

All the data was combined for the ^{27}Si states of interest as well as the normalization data (discussed below). Once the data has been combined, the branching ratios for proton decays from excited states in ^{27}Si to states in ^{26}Al can be determined. The first step is to identify each peak of interest in the focal plane spectrum. The counts making up each peak fall within a specified range on the position axis. One then integrates the number of counts within this range for the triton peak of interest and subtracts background to find N_{FP}, the number of counts in the peak of interest in the triton spectrum without any SABRE cuts applied. N_{FP} is background subtracted but could not be straightforwardly linearly background subtracted. Because the peaks in the triton spectrum are so close together, a linear background subtraction was not feasible and so a number of sections

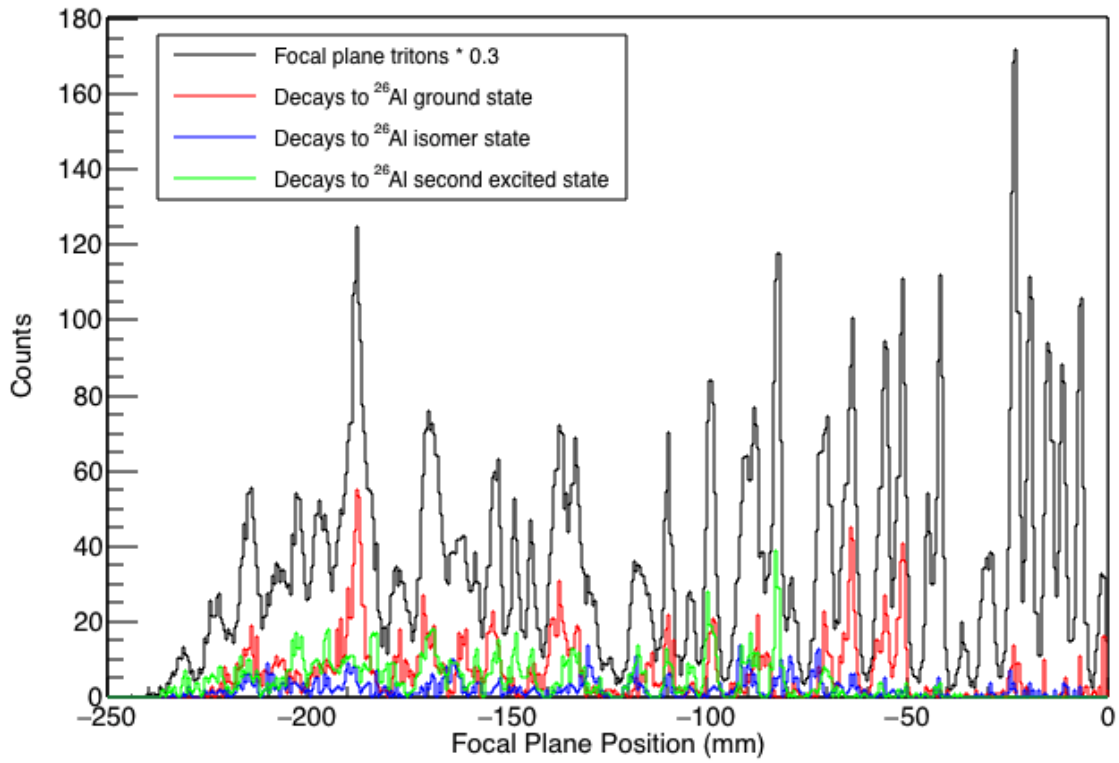

Figure 4.10. The focal plane tritons from Fig. 4.6 are plotted (black) along with those events corresponding to the proton decays to the ground, isomer, and second-excited state of ^{26}Al, in red, blue, and green, respectively. The red, blue, and green spectra were produced by applying diagonal gates to the data shown in Fig. 4.9 as described in the text. The focal plane tritons, in black, are scaled to 0.3 of the axis values for ease of viewing. This figure includes all the analyzed data, and the spectrum shows only those peaks which can be detected with SABRE.

of the focal plane detector without peaks were sampled and averaged to determine the average background per channel for the focal plane.

The integrated peak counts minus the background are also determined for the spectrum that includes the cuts on the SABRE data to find N_P, the number of proton decays detected in SABRE corresponding to that peak of interest. In this case, the background is subtracted via a linear background subtraction on the timing spectrum shown in Fig. 4.8. The number of channels in the peak is divided in two and background is taken to the left and right of the peak in the timing spectrum. The spectrum of this background is shown in Fig. 4.13. N_p is determined not for the entirety of

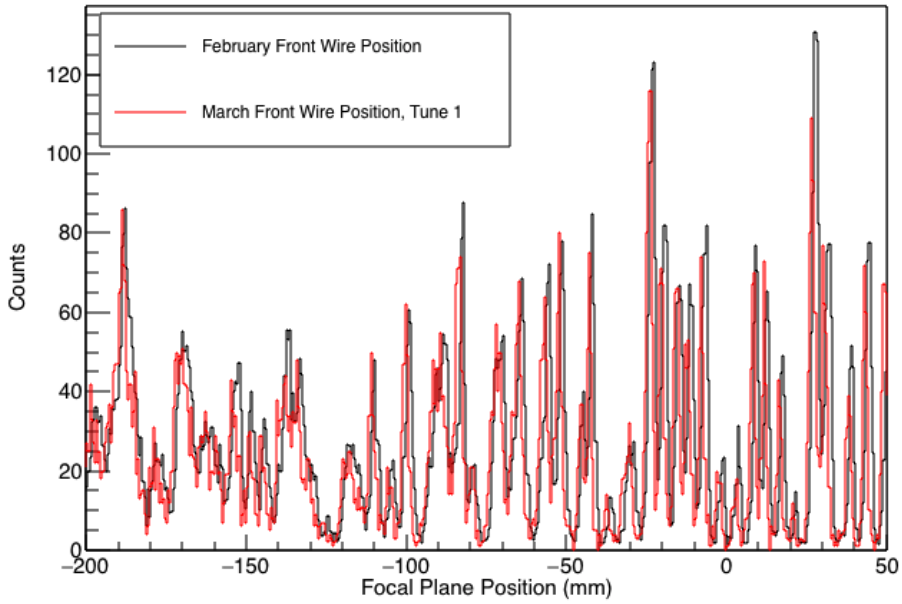

Figure 4.11. States populated in ^{27}Si, for both the February and first set of March data. The February data is scaled to 0.3 of its original value on the y-axis for easier comparison of the spectra. Here each set is shown without any position adjustment applied.

the SABRE data, but for groups of annular strips representative of theta angles. Here we divided the SABRE detector into four theta angular bins comprised of four adjacent annular strips on each detector. For each peak of interest, we find the value N_p four times, one for each angular bin in SABRE (these bins are contiguous about the phi angle in the array).

We then calculate the counts per solid angle, i.e. the effective branching ratio per solid angle, for each of the four angular bins in SABRE that decay to a specific state in ^{26}Al via

$$\frac{dn}{d\Omega} = \frac{N_p}{N_{FP}(\epsilon)(4\pi)}, \tag{4.1}$$

where for each specified peak of interest, ϵ is the efficiency of the four-strip bin of SABRE calculated by the previously described Monte Carlo simulation; here all decay efficiencies are calculated for $l = 0$ angular momentum transfers (i.e. an isotropic distribution) to describe the geometric efficiency as we will fit the angular distributions, to determine the l transfer, below.

The uncertainty for each $dn/d\Omega$ value is found via basic propagation of uncertainty, which

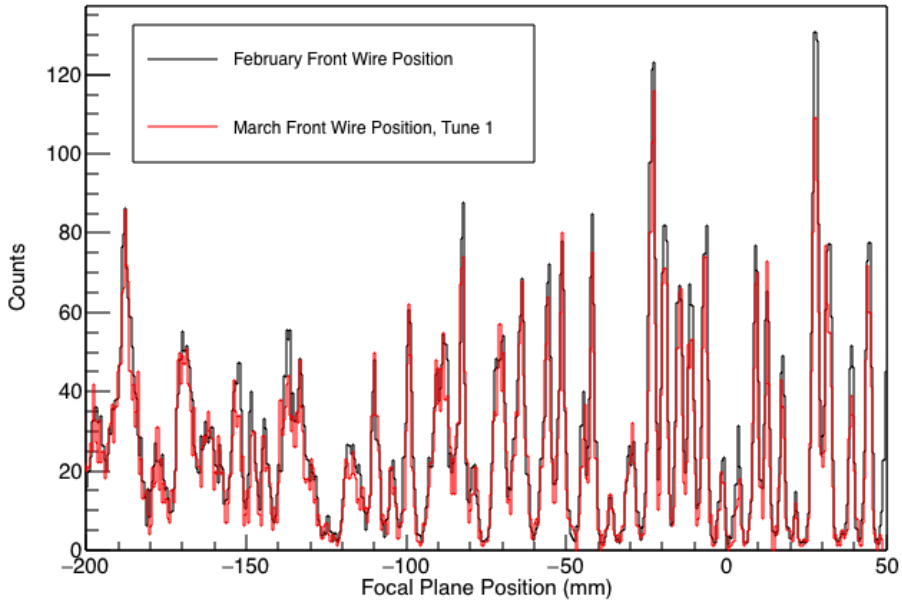

Figure 4.12. States populated in ^{27}Si, for both the February (black) and first set of March (red) data. The February data is scaled to 0.3 of its original value on the y-axis for easier comparison of the spectra. Here, a constant factor of 1 mm is added to the March data, which aligns the two data sets such that they can be added together without any loss of position resolution.

simplifies to

$$\sigma_f = |f| \sqrt{\left(\frac{\sigma_p}{N_p}\right)^2 + \left(\frac{\sigma_{FP}}{N_{FP}}\right)^2 + \left(\frac{\sigma_\epsilon}{\epsilon}\right)^2} \tag{4.2}$$

where f is the calculated branching ratio per solid angle $dn/d\Omega$. The error on the focal plane counts is calculated via $\sigma_{FP} = \sqrt{N_{counts} + N_{background}}$ and the errors in SABRE bin counts, σ_{N_P}, are calculated in the same way. The efficiency ϵ and its uncertainty σ_ϵ are calculated for each annular strip and then summed for each four-strip bin calculated. The uncertainty on σ_ϵ is also just a simple statistical error, summed for each strip in a given four-strip bin.

As each detector in SABRE has 16 annular strips on the junction side corresponding to divisions in theta, the four-strip bins described here will result in four values for counts per solid angle $dn/d\Omega$. We then plot these values versus the average center-of-mass angle for each bin (also calculated via the previously described Monte Carlo simulation for each different peak energy) and

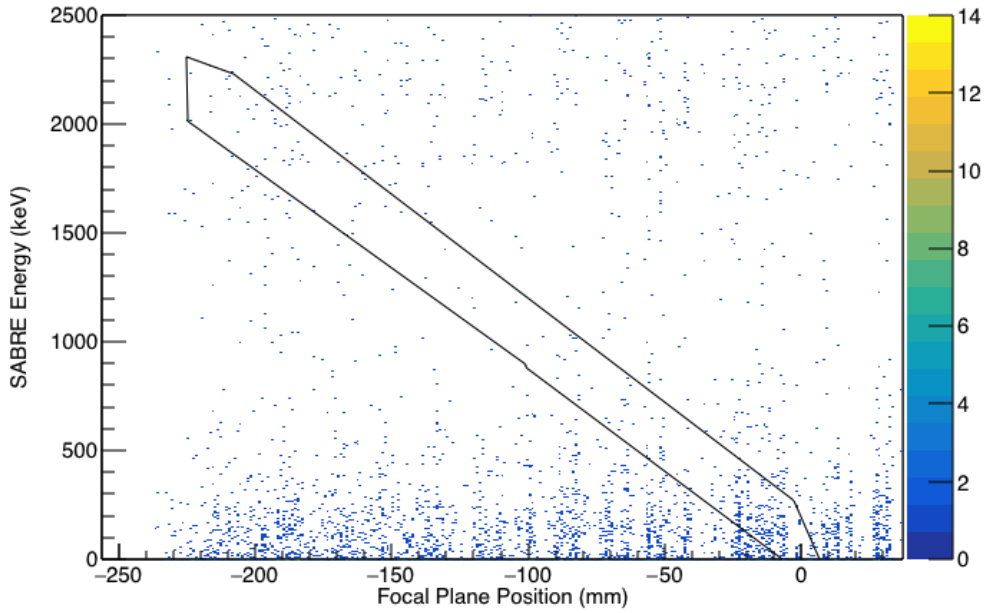

Figure 4.13. Background on the focal plane position versus SABRE energy plot for the February run with the previously discussed focal plane cuts applied. Here the ground state gate is shown as in Fig. 4.9. This plot shows the background from the adjacent cuts on the SABRE timing minus scintillator timing shown and discussed in Fig. 4.8. Note that the most background comes from noise near the threshold at low energies.

fit the data with the angular distribution function [49]:

$$W(\theta) = \sum_{k=0}^{2l} A_k P_k(\cos\theta) \tag{4.3}$$

where A_k are coefficients left free to vary and $P_k(\cos\theta)$ are the Legendre polynomials as a function of $\cos\theta$. The sum is taken over k, which runs from 0 to $2l$, with only even values of k being non-zero. As l is the angular momentum transfer of the proton decay, the l for the best fit of Eq. 4.3 determines the momentum transfer, which allows the determination of the J^π value for the state in ^{27}Si. Conveniently, the m substates of l do not need to be put into Eq. 4.3 due to the SPS magnet being very close to zero degrees, which eliminates the input of m substates.

This function is fit to the data using ROOT's MINUIT minimizer using various values of l to get the best chi-squared value. When this value is found, one integrates the best fit function $W(\theta)$ over 4π with the fitted A_k coefficients to find the branching ratio, where the error is the error in the

fit to this function. Example fits to two states in the ^{27}Si proton decay data for $l = 0$ and $l = 1$ are shown in Fig. 4.14. Plots of the angular fits for all states with enough statistics to make a fit can be found in Appendix C.

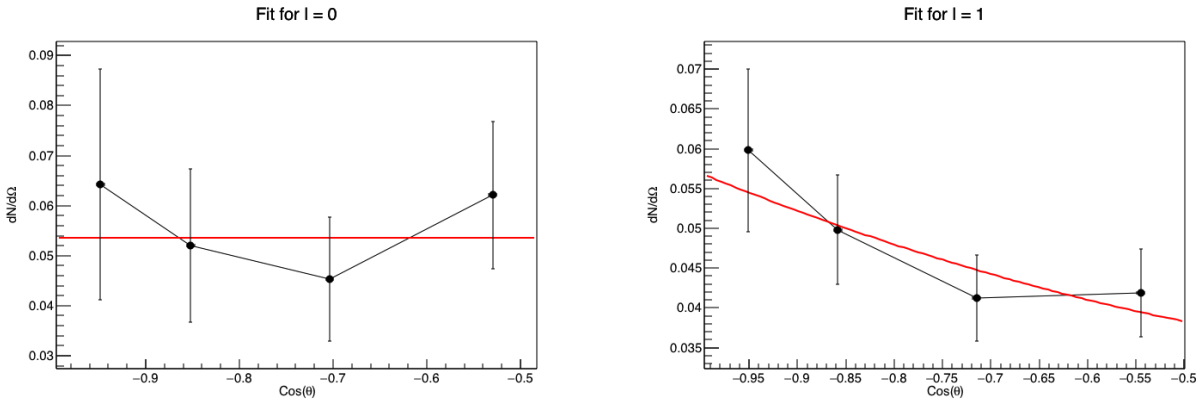

Figure 4.14. Here the angular fit for the 8.931-MeV state's decay to the ground state of ^{26}Al is shown on the left and the fit for the 8.354-MeV state's decay to the ground state of ^{26}Al is shown on the right. For 8.931 MeV, the A_0 coefficient of the fit is 0.0535(76) with a chi-squared value of 1.01. For 8.354 MeV, the A_0 coefficient of the fit is 0.0404(44) with a chi-squared value of 0.893.

After these branching ratios are calculated, they must be normalized to a known 100% branching ratio state to account for factors such as dead time in the data acquisition. The data was normalized using the ^{12}C(^{3}He, d)^{13}N reaction, which was measured concurrently with the ^{27}Al(^{3}He, t) reaction due to the carbon backing on the aluminum target, and can be seen in Fig. 4.15. The states used for normalization were the 3.502- and 3.547-MeV inseparable doublet in ^{13}N, both of which have 100% proton branching ratios. This reaction data was analyzed in the same way as the aluminum data above, selecting for the deuteron particle group in the focal plane data, and the branching ratio found by using the same fitting technique. The fit for this normalization data is shown in Fig. 4.16. Because there are two states of different spin parities in the doublet (3/2- and 5/2+, respectively), a choice was made for the l value needed to fit the angular distribution function. The value $l = 2$ was chosen because several studies [50] [51] showed that the 3.547-MeV, 5/2+ state was the dominantly populated state in the ^{12}C(^{3}He, d)^{13}N reaction, several varying DWBA calculations in DWUCK4 showed that it was also the dominantly populated state (see calculations in Fig. 4.17), and the fact that the $l = 2$ fit would still encapsulate any $l = 1$ information from the

decay of the 3.502-MeV state in this mix of a fit. It was found that the branching ratio measured for these two states is 56(2)%.

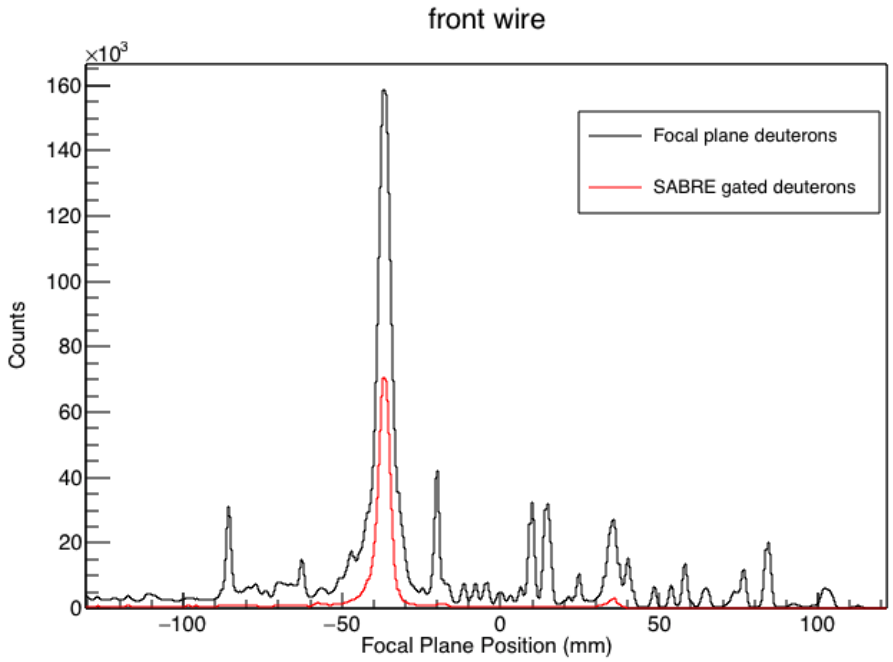

Figure 4.15. The spectrum from the ^{12}C(^{3}He, d)^{13}N reaction used for normalization. All deuterons detected in the focal plane are shown in black, while the subset of data from gated proton decays from ^{13}N into SABRE are shown in red. Here the deuteron values in black are scaled to 0.3 of their value. The doublet used for normalization is centered around -38 mm on this spectrum.

The Al data branching ratios were then normalized using this value via:

$$\frac{\Gamma_p}{\Gamma} = \frac{BR_{measured}}{0.56} \tag{4.4}$$

with the uncertainty determined by the uncertainty in the angular fits.

The final values of the ^{27}Si proton branching ratios to the ground and first two excited states of ^{26}Al are shown in Table 4.1; a labeled focal plane spectrum of all states in Table 4.1 can be seen in Fig. 4.18. The table gives the energies of the states, the minimum l value required for an acceptable angular fit l_{min} (here requiring a chi-squared value of less than 5), and the measured proton branching ratio Γ_p/Γ of the state. Any state with a measured branching ratio and no l_{min}

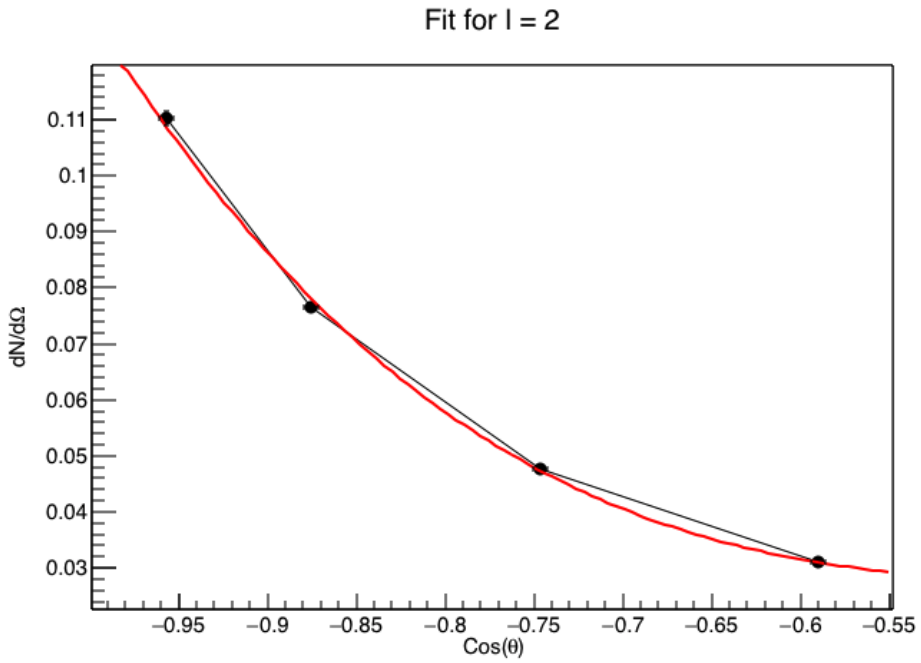

Figure 4.16. The angular fit for the normalization doublet states is shown. The A_0 coefficient of the fit is 0.0487(23) with a chi-squared value of 0.248.

value given was not fit with Eq. 4.3 but calculated via

$$BR_{measured} = \frac{N_p}{N_{FP}(\epsilon)} \tag{4.5}$$

due to low statistics, where ϵ is calculated via the Monte Carlo simulation assuming $l = 0$. It was then normalized using Eq. 4.4 to obtain Γ_p/Γ.

Note that the states in Table 4.1 below $E_x = 8.070$ MeV may have slightly higher efficiencies than those used in Eqs. 4.1 and 4.5 to calculate their branching ratios (which lowers the overall branching ratio values). The calculations for these lowest states used the 8.070 MeV efficiency as a small fraction of simulated particles stopped in the simulated target and thus froze the code below this energy level. However, the 7.6516 MeV decay to the ground state and both 7.832 MeV decays should be regarded as upper limits for this data because their measured branching ratios are also consistent with branching ratios of zero within error bars. The overall low statistics of this data set and the low energies of the proton decays from these states make it difficult to separate these

Table 4.1. Proton branching ratios and minimum angular momentum transfer for states in ^{27}Si up to 1.5 MeV above the proton threshold. Each state may decay to the ground, isomeric, and/or second-excited state in ^{26}Al as labeled in the first row. States with an l_{min} value were able to be fit to the angular distribution equation 4.3, while states with N/A were unable to be fit in that way due to low statistics and used Eq. 4.5. [a]This branching ratio was calculated to be 112%, but as that is unphysical, was renormalized to 100%, which is in agreement with its calculated error.

	Ground State		Isomer State		417 keV State	
E_x (MeV)	l_{min}	Γ_p/Γ	l_{min}	Γ_p/Γ	l_{min}	Γ_p/Γ
7.6516(1)	N/A	2(2)				
7.832(2)	1	6(6)	N/A	0.5(5)		
8.070(3)			N/A	0.5(3)		
8.162(2)	N/A	0.9(6)				
8.210(4)	0	95(7)				
8.299(5)	1	67(9)				
8.324(5)	N/A	38(10)				
8.354(3)	1	85(9)				
8.375(3)	1	77(12)				
8.446(3)	N/A	13(4)	0	36(6)		
8.486(3)			1	40(23)		
8.523(3)					N/A	24(5)
8.557(3)	0	54(6)			1	31(7)
8.586(3)	N/A	8(3)	0	46(6)	1	24(6)
8.668(3)	0	56(6)			2	37(21)
8.864(3)	1	91(21)			N/A	17(5)
8.931(4)	0	100(16)[a]				
8.984(3)			N/A	14(4)	0	83(10)
9.026(3)			N/A	26(8)		

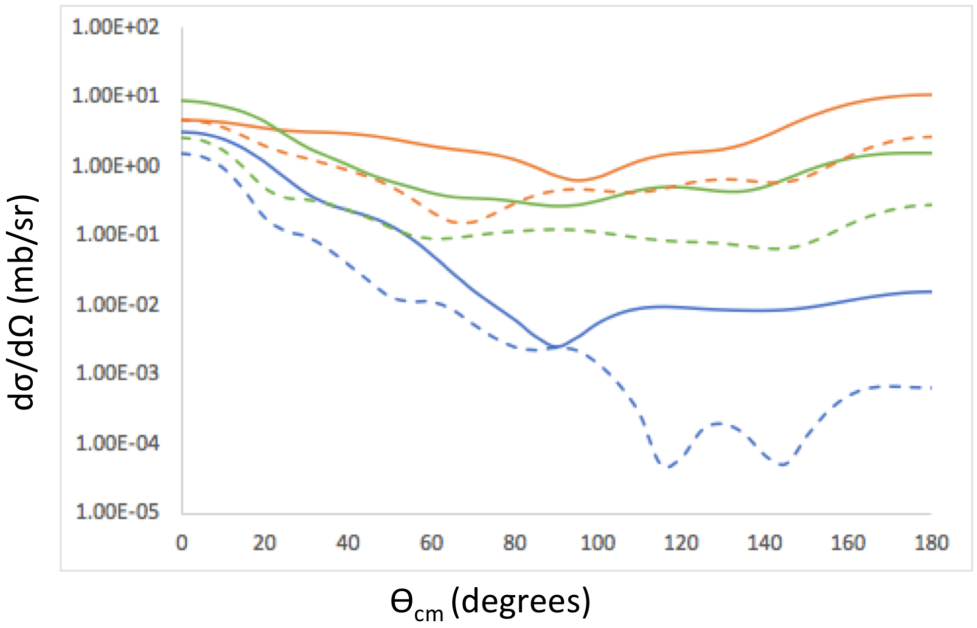

Figure 4.17. DWBA calculations for the 3.547-MeV (solid lines) and 3.502-MeV (dashed lines) states calculated in DWUCK4. The orange lines use optical model parameters from Ref. [52] for ^{12}C + *d*, Ref. [53] for ^{12}C + ^{3}He, and Ref. [54] for ^{13}N + *d*. The green lines use optical model potentials from Ref. [55] for ^{12}C + *p*, Ref. [56] for ^{12}C + ^{3}He, and Ref. [57] for ^{13}N + *d*. The blue lines use optical model potentials from Ref. [58].

real signals from the low energy background, and more statistics are needed to make a confident assignment of their proton branching ratios.

Additionally in Table 4.1, we used the energy assignments from Ref. [29] above 8.136 MeV and the NNDC below 8.136 MeV to assign the excitation energies as these data sets were better calibrated and the focal plane detector currently has some questionable behavior in position spectra due to deformed wires and other issues.

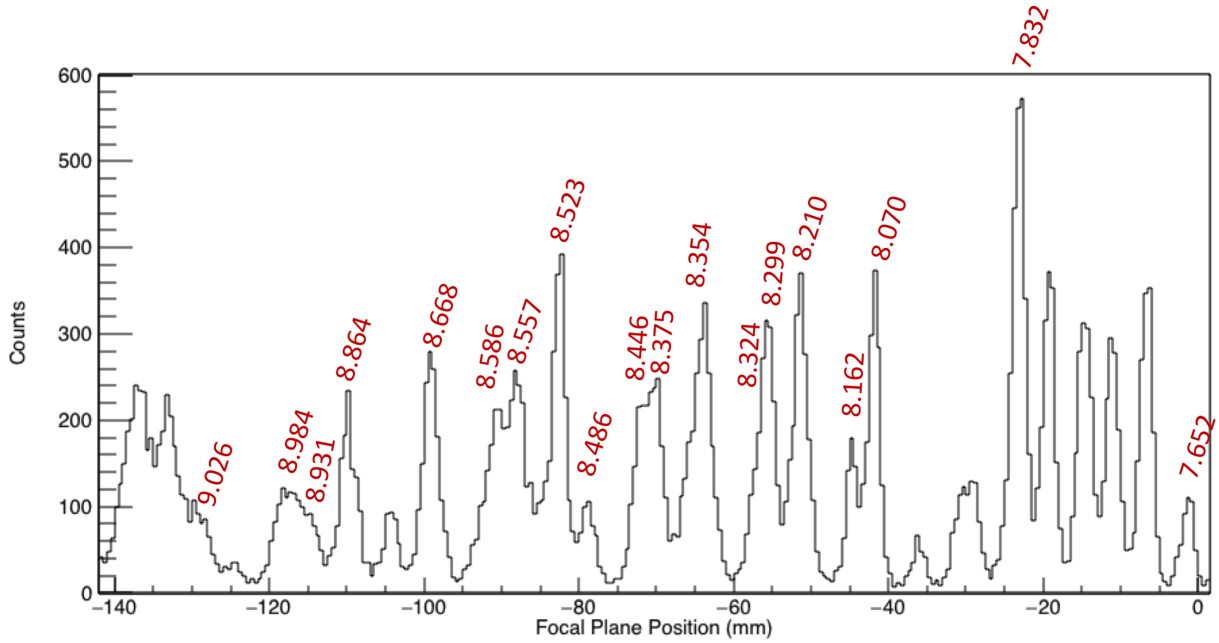

Figure 4.18. States populated in ^{27}Si that have measured branching ratios in Table 4.1 are labeled here with their energy values in MeV. States that are not labeled are not in the table.

5 Conclusions

In the previous chapter, the analysis and results for the ^{27}Si proton branching ratios measured via the ^{27}Al(^{3}He,t)^{27}Si*(p)^{26}Al reaction are discussed. This is the first time the ^{26}Al^{g,m}(p,γ) reaction has been studied in this way at ^{27}Si excitation energies below 8.136 MeV, and branching ratios determined via this reaction have never been published. As such, this study is a complementary approach to the previous studies discussed in Chapter 1.

5.1 Comparison with Previous Measurement

Branching ratios for seven states in ^{27}Si that have not been previously measured are presented here. These include the states at 9.026, 8.324, 8.299, 8.162, 8.070, 7.832, and 7.6516 MeV. Proton decays from the states below 8.136 MeV were undetectable with previous arrays, so those three states, with their very small branching ratios, are of particular interest to reaction rate calculations. It is also informative that many of the states below 8.136 MeV with proton decay energies above the energy threshold of SABRE did not appear to have a measurable branching ratio. This is not unexpected, as gamma partial widths are expected to remain relatively constant, while the proton partial widths are expected to decrease with decreasing excitation energy, and that is the general trend for states close to the proton threshold in Table 4.1. However, these states with low proton branching ratios are the most important to measure as in the resonance strength equation for this reaction:

$$(\omega\gamma)_r = \frac{(2J_r + 1)}{(2J_{^{26}\mathrm{Al}^m} + 1)(2J_p + 1)} \frac{\Gamma_p \Gamma_\gamma}{\Gamma} \tag{5.1}$$

if $\Gamma_p << \Gamma_\gamma$, then $\Gamma = \Gamma_\gamma + \Gamma_p \approx \Gamma_\gamma$ and the final width factor above reduces to just Γ_p. Therefore these lowest excitation energy branching ratios are of prime importance to calculating the reaction rate.

Of the states previously measured, six states agree with previous branching ratio measurements from Ref. [29]'s ^{28}Si(^{3}He, α) reaction and can be seen in Table 5.1. These states agree well within errors and the state at 8.557 MeV agrees for both decays to different states in ^{26}Al. Seven states do not agree within uncertainties, and several branching ratios are newly measured in this data set. Of the states that do not agree, it is possible that the branching ratios for the 8.210 and 8.354 MeV

Table 5.1. Branching ratios measured in this experiment and the ^{28}Si(^{3}He, α) reaction of Ref. [29] for states that were measured in both. A total of six states (seven branching ratios total), agree between these measurements.

	Ground State		Isomer State		417-keV State	
E_x (MeV)	Current	Ref. [29]	Current	Ref. [29]	Current	Ref. [29]
8.210	95(7)	15(4)				
8.354	85(9)	39(6)				28(4)
8.375	77(12)			31(8)		
8.446	13(4)		36(6)	47(7)		
8.486			40(23)			22(5)
8.523		39(12)			24(5)	
8.557	54(6)	36(20)			31(7)	35(17)
8.586	8(3)		46(6)	40(9)	24(6)	
8.668	56(6)	16(5)			37(21)	48(13)
8.864	91(21)					94(13)
8.931	100(16)	100(100)				
8.984			14(4)	28(10)		

states are higher in this measurement due to the lower thresholds our detectors were able to achieve compared to those in Ref. [29]. Of the higher lying states that do not agree, it is possible that some states were incorrectly assigned energies in this measurement as the calibration in this work was just used as a guideline to assign energies that were measured and calibrated in Ref. [29]. A more careful calibration with additional calibration reactions like those carried out in Ref. [29] would be useful in this pursuit.

5.2 Reaction Rate

As discussed above, the branching ratios for states at $7.6516 \leq E_x \leq 8.162$ MeV have been measured for the first time. To quantify their effect on the reaction rate, the reaction rate was calculated from Eqs. 1.23 and 1.24 for the typical temperatures of a classical nova. For those states where an angular momentum transfer could be determined, those values were used to determine the J^π of the states. For those states where an angular momentum transfer could not be determined, the NNDC J^π values were used if present. If not, a transfer of $l = 0$ was assumed, as the lowest angular momentum transfer is energetically preferred. The results of these calculations can be seen in Figs. 5.1 and 5.2. Figure 5.1 takes the Γ_γ width to be 1 eV for all states as in Ref. [29]

for a direct comparison between these two measurements. Figure 5.2 uses the Γ_γ widths listed in Table 5.2, which used existing experimental data from Ref. [28] to calculate realistic Γ_γ widths where available to get a best calculation for the reaction rate. In both cases the newly determined reaction rates are compared to the reaction rate calculated for the previous ^{28}Si(^{3}He, α) reaction measurement [29] as well as the rate from the NACRE collaboration in Ref. [27] that evaluated the thermonuclear reaction rate based on the existing nuclear data for the ground state reaction at the time, which was then scaled to determine the ^{26}Al$^m(p,\gamma)$ rate. As discussed in Chapter 1, these two states have very different properties, and as shown in this study, the ground and isomer states are populated by different ^{27}Si state decays. Thus, assuming the ground and isomer state reaction rates to be scaled versions of one another is not necessarily correct. Unfortunately, newer evaluations like those in Ref. [59] use the same technique as the two-decade-old NACRE evaluation (and get almost identical results) as the previous measurement from Ref. [29] did not measure low enough resonances to affect the previous evaluated rate. These low energy resonances are extremely important to the nuclear astrophysics community as the nuclear reaction rate depends most strongly on the lowest energy resonances.

Table 5.2. Values used in the calculation of the ^{26}Al$^m(p,\gamma)^{27}$Si reaction rate for Figs. 5.1 and 5.2. Each state lists the ^{27}Si excitation energy, the resonance energy E_r, and the l_{min} values fit during this measurement. The J^π values for each state assumed the lowest J^π for the allowed l transfer. The Γ_γ values for Fig. 5.1 were taken to be the same as those used in Ref. [29]. The Γ_γ values for Fig. 5.2 that are not 1 eV were calculated using Weisskopf estimates calculated with gamma ray energies and state assignments taken from Ref. [28]. $^a J^\pi$ values for these states were taken to be the lower of tentative spin assignments from the NNDC. ^{b}Angular momentum transfer l for these states was assumed to be 0.

E_x (MeV)	E_{res} (keV)	Fit l_{min}	J^π of state	Γ_p/Γ (%)	Γ_γ for Fig. 5.1 (eV)	Γ_γ for Fig. 5.2 (eV)
7.832(2)	141	N/A	$9/2^a$	0.5(5)	1	0.0611 (E2)
8.070(3)	379	N/A	$5/2^a$	0.5(3)	1	$2.185 \times 10^{-4}(E1)$
8.446(3)	795	0	3/2	36(6)	1	1
8.486(3)	832	1	1/2	40(23)	1	1
8.586(3)	977	0	3/2	46(6)	1	1
8.984(3)	1293	N/A^b	3/2	14(4)	1	1
9.026(3)	1383	N/A^b	3/2	26(8)	1	1

As seen in Figs. 5.1 and Fig. 5.2 , the ^{26}Al$^m(p,\gamma)^{27}$Si reaction rate is determined by the lowest

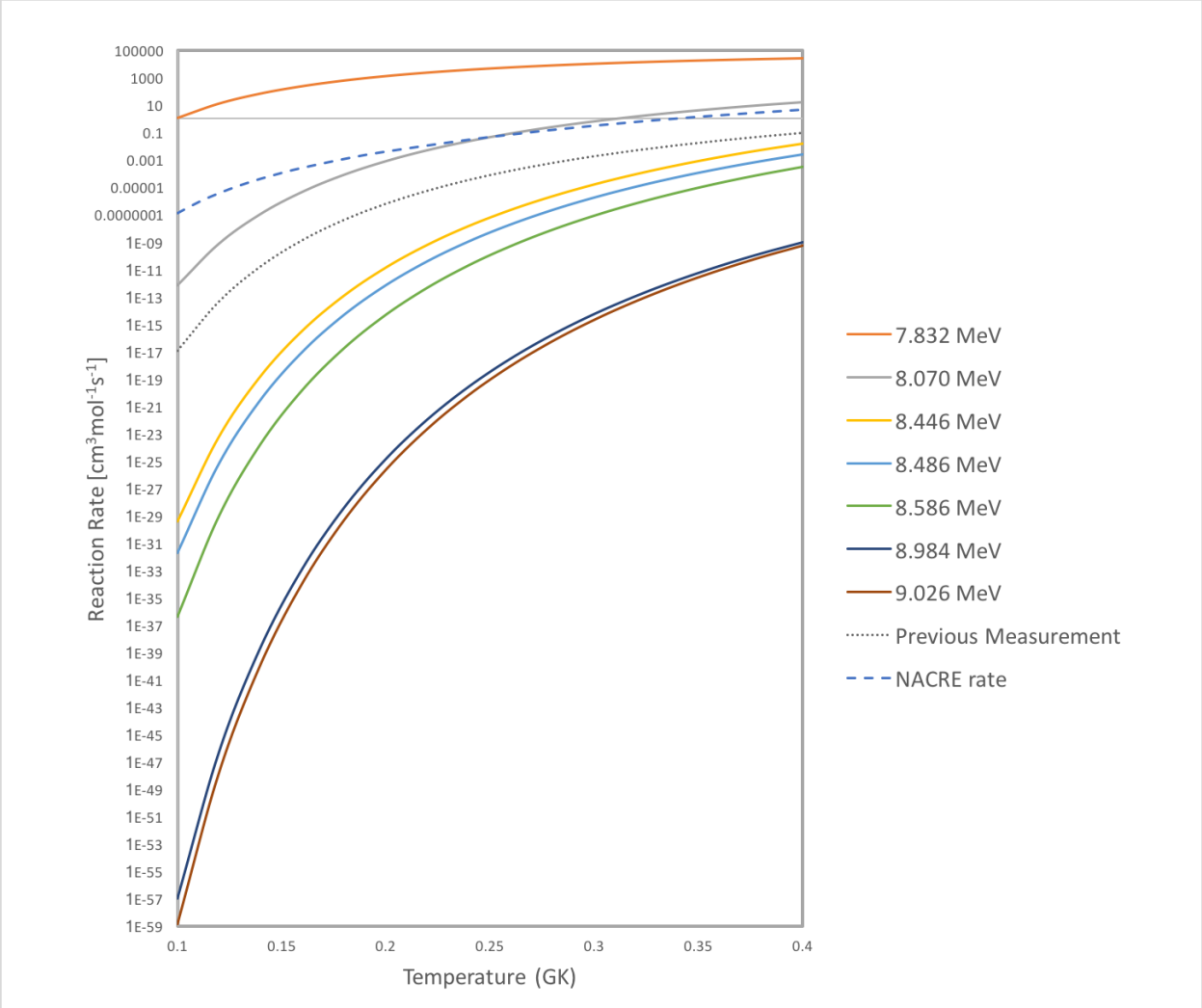

Figure 5.1. The $^{26}\mathrm{Al}^{m}(p,\gamma)^{27}\mathrm{Si}$ reaction rate calculated using the results of this work compared to the NACRE evaluated rate [27] and the reaction rate calculated in Ref. [29]. This work's calculations of the rate and the calculations from Ref. [29] assume a gamma partial width Γ_γ of 1 eV in order to make a direct comparison with rates calculated in Ref. [29]. Note the large contributions of the 7.832 MeV state as well as the 8.070 MeV state at higher temperatures; however, the 7.832-MeV contribution should be taken as an upper limit.

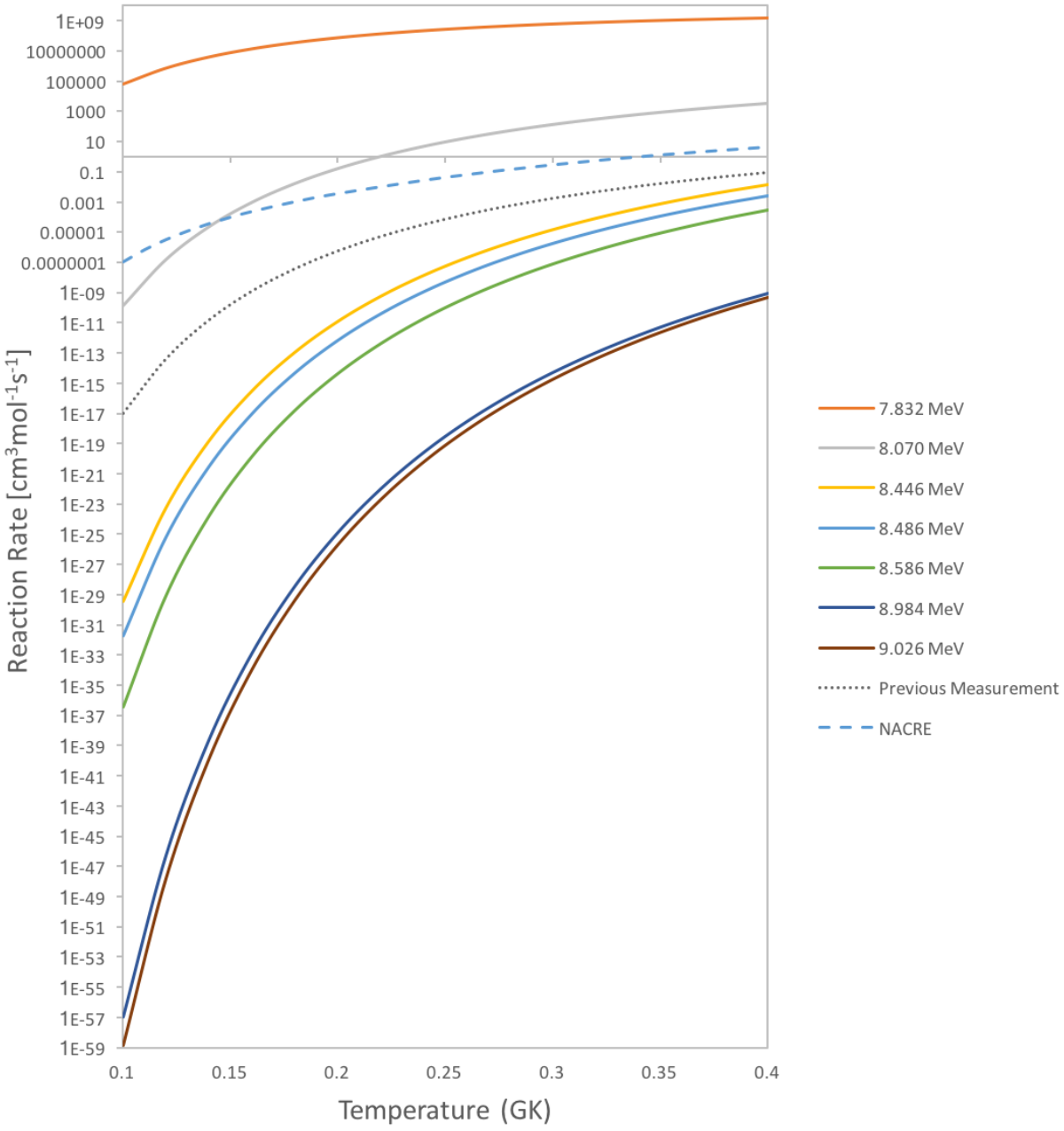

Figure 5.2. The $^{26}\mathrm{Al}^{m}(p,\gamma)^{27}\mathrm{Si}$ reaction rate calculated using the results of this work compared to the NACRE evaluated rate [27] and the reaction rate calculated in Ref. [29]. This work's calculations of the rate and the calculations from Ref. [29] use the gamma partial widths listed in Table 5.2. Note the large contributions of the 7.832 MeV state as well as the 8.070 MeV state at higher temperatures; however, the 7.832-MeV contribution should be taken as an upper limit.

energy states with proton decays detected in SABRE. When compared to existing evaluations of the reaction rate, it appears that the 7.832-MeV state has a large contribution to the rate. However, the measured branching ratio for this state ($\Gamma_p/\Gamma = 0.5(5)$) has an uncertainty consistent with a branching ratio of zero and thus must be taken as an upper limit on the rate. Additionally, a calculation of the Wigner limit for the proton width (which is typically much higher than the actual proton width) gives a value of 4.55×10^{-5} eV, which implies that the measured branching ratio is likely undetectable, meaning that this branching ratio is likely consistent with noise. The contribution from the 8.070 MeV state is also larger than the total rate determined in Ref. [29], but is likely to be a real measurement due to its smaller error and the fact that the Wigner limit of the proton width for this state is calculated to be 10.92 eV, while a Weisskopf estimate of the gamma width is calculated to be 2.185×10^{-4} eV from Ref. [28]. This Wigner limit proton width indicates that the branching ratio should be 100%, but because the width is usually a much higher upper limit, here it implies that a branching ratio should at least be detectable. Additionally, these states were indicated to be the largest contributors to the reaction rate for the isomer state as discussed in Chapter 1, so this work is consistent with and supports the previous work in Refs. [28] and [26].

The measured branching ratio and previous results discussed in Chapter 1 (Refs. [28] and [26]) indicate that the 8.070 MeV state is likely a large contributor to the reaction rate; however, a higher statistics data set is desirable to verify that this state indeed strongly contributes to the reaction rate. The gamma width also plays a role in the size of the reaction rate due to this state, and when an experimentally determined Weisskopf estimate is used to determine the rate, the contribution from this state increases, as seen in Fig. 5.2; thus, a theoretical determination or direct experimental measurement of the gamma width for this resonance would also be desirable.

Aside from these lower energy decays of interest to the $^{26}\mathrm{Al}^m(p,\gamma)^{27}\mathrm{Si}$ reaction rate, some of the other branching ratios from these experimental results are currently tentative due to low overall experimental statistics. These are the branching ratios that were calculated without fitting an angular distribution using equation Eq. 4.5 (and thus assuming an $l = 0$ decay). These states are the 7.6516, 8.162, 8.324, 8.446 (to ground state only), 8.523, 8.586 (to ground state only), 8.864 (to

417 keV state only), 8.984 (to isomer state only), and 9.026 MeV states with measured branching ratios. More statistics should allow an angular fit to these states.

The desired increase in statistics will come in a planned run to supplement the current data. This will result in more statistics in the low energy states of interest, allowing for better angular fits and increased confidence in current results. However, the agreement of the current results with previous measurements gives confidence that these data provide interesting insight into the current state of the $^{26}Al^{m}(p,\gamma)^{27}Si$ reaction rate. Specifically, the current results show that previous evaluations of the $^{26}Al^{m}(p,\gamma)^{27}Si$ reaction rate underestimate the rate. An increased reaction rate as suggested here by the 8.070 MeV measurement would mean that more ^{26}Al is destroyed in novae, which would impact the abundance ratios of $^{26}Al/^{27}Al$ seen in presolar grains. Overall, space-based observations of the 1.809-MeV gamma ray would not be affected by this rate, as only the ground state decay of ^{26}Al produces the gamma ray; this work's measurements of ^{27}Si proton branching ratios to the ground state for the most impactful resonances (the 184-keV resonance) are consistent with zero and thus do not affect this gamma ray's production. However, any observed abundance of ^{26}Mg in presolar grains (which implies an increased amount of ^{26}Al in the source of the presolar grain) would come primarily from the ground state decay of ^{26}Al and a minimal amount from the decay of the ^{26}Al isomer state, as the calculated reaction rate in this work implies a robust destruction rate of the ^{26}Al isomer state before it can β^{+} decay to ^{26}Mg.

5.3 Future Plans

The experimental results described here include the first time that SABRE has been used to measure branching ratios. This experiment allowed the capabilities of SABRE and its new digital electronics scheme to be quantified. SABRE will continue to be used for a variety of experiments at FSU and several upgrades to the detectors are being discussed and implemented, including the development of two new focal plane detectors (one for light reaction particles and another one for heavy reaction particles) and a gamma-ray detector setup around the target chamber.

With the ongoing development of more intense $^{26}Al^{m}$ beams, a future direct measurement of the $^{26}Al^{m}(p,\gamma)^{27}Si$ should one day be possible, with this work and previous works being used to

guide the direct measurement at the proposed major contributing resonances at 146 and 387 keV. A direct measurement of the isomer reaction will concretely determine the destruction rate of ^{26}Al in classical novae. Additional ongoing work on the production of a ^{26}Al^{g} target will allow for other complementary studies of the production and destruction of ^{26}Al in other stellar environments. The first of two proposed experiments with this target is a study of ^{26}Al^{g}(^{3}He, d)^{27}Si to measure angular distributions with the SE-SPS at FSU. This study would focus on determining a proton spectroscopic factor measurement to determine the resonance strength of the 127-keV resonance expected to dominate the ^{26}Al^{g}(p, γ)^{27}Si reaction rate in AGB and Wolf-Rayet stars. The second study with this target is a proposed measurement of the proton branching ratios in ^{26}Al via the ^{26}Al^{g}(^{3}He, t)^{26}Si*(p)^{25}Al reaction utilizing the setup discussed in this work. This study would be analogous to this work, but measuring proton branching ratios of interest to the ^{25}Al(p, γ)^{26}Al reaction, which is one of the only other reaction rates important to ^{26}Al nucleosynthesis in novae that still has relatively large uncertainties. These proposed future studies will greatly constrain the uncertainties in the production of ^{26}Al in our Galaxy.

With the current setup, additional experiments are planned to study both nuclear structure and astrophysics in addition to those discussed in the previous paragraph. These include a study of ^{19}F(^{3}He, t)^{19}Ne*(α)^{15}O for branching ratios of interest to the ^{15}O(α, γ)^{19}Ne reaction in Type I X-ray Bursts, a study of ^{35}Cl(^{3}He, t)^{35}Ar*(α)^{34}Cl^{m} for branching ratios of interest to the ^{34}Cl^{m}(p, γ)^{35}Ar reaction in nova nucleosynthesis, and a study of ^{24}Mg(^{12}C, ^{6}He)^{30}S to measure states in ^{30}S of interest to the ^{26}Si(α, p)^{29}P reaction. As SABRE is used for coincidence measurements, the array is also planned for use in a study of ^{10}B(^{3}He, α)^{9}B to tag on the breakup products of ^{9}B and clean up the focal plane spectra; this reaction will be used to study astrophysically relevant states of ^{9}B around 16.7 to 16.8 MeV as well as its elusive first excited state of interest to the nuclear structure community. The SABRE array coupled with the SPS has a variety of useful and interesting applications, and should be an asset to FSU's John D. Fox accelerator laboratory community for years to come.

Appendix A: Monte Carlo Simulation of Si Array Efficiency

Included here are the two files that explicitly define geometry for SABRE. This code was originally written by Dale Visser (Ref. [30]) and has been altered for the SABRE geometry.

MicronDetector.java

```
/**************************************************************
 * Nuclear Simulation Java Class Libraries
 * Copyright (C) 2003 Yale University
 *
 * Original Developer
 *      Dale Visser (dale@visser.name)
 *
 * OSI Certified Open Source Software
 *
 * This program is free software; you can redistribute it and/or
 * modify it under the terms of the University of Illinois/NCSA
 * Open Source License.
 *
 * This program is distributed in the hope that it will be
 * useful, but without any warranty; without even the implied
 * warranty of merchantability or fitness for a particular
 * purpose. See the University of Illinois/NCSA Open Source
 * License for more details.
 *
 * You should have received a copy of the University of
 * Illinois/NCSA Open Source License along with this program; if
 * not, see http://www.opensource.org/
 **************************************************************/
```

```
package dwvisser.monte;
import dwvisser.math.Matrix;
import java.io.FileWriter;
import java.io.IOException;

/**
 * This class represents the geometry of a Micron LEDA-type detector,
 * to use for deciding if an virtual vector will hit and which strip.
 *
 * @author  Dale Visser
 * @version 1.0 (7 March 2001) //Edited by Erin for SABRE 2016
 */
public class MicronDetector extends Object implements WeightingFunction {

    private double z0, theta;
    private Matrix rotate; //rotation matrix between lab and detector
    private Matrix xpd; //lab origin in detector frame
    boolean hit; //whether a strip was hit
    private double cosThetaInc; //cosine of incidence angle if detector hit
    private int strip; //if detector hit, contains strip that was hit
    boolean interstrip; //if interstrip event then true
    double distance; //distance to detector plane, in mm

    //Detector geometry from T. Davinson et.al. NIM A 454 (2000) 350-358
    //Inner radius for strip is 50.00 mm + 5.00 mm * strip number (0 thru 15)
    //Outer radius for strip is inner radius + 4.90 mm
    //phi extents in degrees are as follows
```

```
//private static final double [] PHI = {39.82, 40.00, 40.17, 40.30, 40.42,
//40.52, 40.61, 40.69, 40.76, 40.82, 40.88, 40.93, 40.98, 35.89, 28.75, 18.91};
private static final double phiLimit = Math.toRadians(27.2); // (this is half of
    the detector wedge in degrees) the SABRE wedges subtend 54.4 deg. total of
    active area NOT INCLUDING INTERSTRIP REGIONS.
private static final double[] rayDisplacement =
            {
                    0.0,
                    0.0,
                    0.0,
                    0.0,
                    0.0,
                    0.0,
                    0.0,
                    0.0,
                    0.0,
                    0.0,
                    0.0,
                    0.0,
                    0.0,
                    0.0,
                    0.0,
                    0.0};
private static double[] zDiff = new double[rayDisplacement.length];

/** It is assumed that the detector is centered about phi=90 degrees.
 * Unfortunately, the real array has detectors at -90 degrees, etc,
```

```
 * so some care is needed in using this. See the changePhi and getDetector
 * methods. This
 * constructor specified the location along the z-axis of the virtual center
 * of the detector.  Zero would be the target, and positive numbers mean upstream
 * of the target.
 * Theta is the angle the normal vector of the detector plane makes with the
 * beam axis (positive by definition).  Alternatively, it is the angle that
 * an initally flat array gets rotated forward to be in the lampshade
 * configuration.
 * @param z0 in mm
 * @param theta in radians
 */
public MicronDetector(double z0, double theta) {
    this.z0 = z0; //in mm
    this.theta = theta;
    double thetaP = (theta - Math.PI / 2.0);
    rotate =
        new Matrix(
            "1 0 0\n"
                + "0 "
                + Math.cos(thetaP)
                + " "
                + Math.sin(thetaP)
                + "\n"
                + "0 "
                + (-Math.sin(thetaP))
                + " "
```

```
                + Math.cos(thetaP)
                + "\n");
        Matrix temp = new Matrix("0; 0; " + z0 + ";"); //origin before rotating
        xpd = new Matrix(rotate, temp, '*'); //rotated to detector frame
        for (int i = 0; i < rayDisplacement.length; i++)
            zDiff[i] = rayDisplacement[i] / (Math.sin(phiLimit));
        System.out.println(
            "Initialized "
                + getClass().getName()
                + "("
                + z0
                + ","
                + theta
                + ")");
    }

    public boolean isHit(Direction dir) {
        hit = false;
        Matrix detDirMat = new Matrix(rotate, dir.getVector(), '*');
        //Direction detDir = Direction.getDirection(detDirMat);
        cosThetaInc = detDirMat.element[1][0]; //y (norm guaranteed to be 1)
        double s = -xpd.element[1][0] / cosThetaInc;
        //"distance" to detector plane
        distance = s; //distance in mm to detector plane
        double px = xpd.element[0][0] + s * detDirMat.element[0][0];
        //x position of hit
        double pz = xpd.element[2][0] + s * detDirMat.element[2][0];
```

```
//z position of hit
double pr = Math.sqrt(px * px + pz * pz); //radial coordinate of hit
//angular coordinate, zero equals center line of detector strips
//1.5 added to account for the fact that the 42 degree extent of the wafer is
    to one side of the pcb
//above theta is not the one we want...see below
hit = false;
if (pr <= 135.1 && pr >= 32.6) {
    strip = (int) Math.floor((pr - 32.6) / 6.4); //this sets the strip
        geometry. a possible strip is (hit radius-innermost radius)/strip pitch
    double truncR = pr - 32.6 - 6.4 * strip; //calculates strip number? unsure
        .
    /* excess radius from inner strip radius */
    if (strip < 16 && strip > -1) {
        double pzprime = pz - zDiff[strip];
        double pthprime = Math.atan2(px, pzprime);
        if (Math.abs(pthprime) <= phiLimit
            && truncR <= 6.30
            && cosThetaInc > 0.0) {
            hit = true;
            /* cTI > 0 eliminates forward hemisphere solutions */
        } else { //hit false...possibly interstrip though
            interstrip = (strip < 15); //false if not
        }
    }
}
return hit;
```

```
}

/**
 * If interstrip is true, then the event was between the returned strip and the
     returned strip + 1.
 */
public int getStrip() {
    return strip;
}

/**
 * Returns 1/cos(incidence angle).
 */
public double getIncidence() {
    return 1.0 / cosThetaInc;
}

/**
 * Returns distance to detector in mm.
 */
public double getDistance() {
    return distance;
}

public boolean getInterStrip() {
    return interstrip;
}
```

```
/**
 * Given a direction, returns a direction with modified phi so that
 * associated direction is in the correct 72 degree window to possibly hit
 * the detector(90–36 to 90+36, or 54 to 126).
 */
static public Direction changePhi(Direction dir) {
    double phi = Math.toDegrees(dir.getPhi()); //input phi in degrees
    phi -= 18;
    int n = (int) Math.floor(phi / 72);
    double x = phi - n * 72;
    return new Direction(dir.getTheta(), Math.toRadians(54 + x));
}

/** based on our convention of the bottom detector being det 4,
 * detector numbers going down as one goes counter clockwise
 * looking at the array from the target
 */
static public int getDetector(Direction dir) {
    double phi = Math.toDegrees(dir.getPhi());
    if (phi < 18)
        return 3;
    if (phi < 90)
        return 2;
    if (phi < 162)
        return 1;
    if (phi < 234)
```

```
        return 0;
    if (phi < 306)
        return 4;
    return 3; //must be >= 306 and <= 360
}

/**
 * Weighting for isotropic thetas in degrees.
 */
public double weight(double x) {
    return Math.sin(Math.toRadians(x));
}

static public void main(String[] args) {
    //String fileRoot = "d:\\simulations\\labEfficiency\\";
    String fileRoot = "/Users/eringood/Desktop/SPS_Code/mcSims/";
    Direction d;
    boolean hit;
    double z0 = 124.54;
    double incline = 40;
    String input =
        "z"
            + (int) Math.round(z0 * 10)
            + "th"
            + (int) Math.round(incline * 10);
    DataSet[] theta = new DataSet[16];
    DataSet[] inc = new DataSet[16];
```

```
DataSet[] dist = new DataSet[16];
MicronDetector md = new MicronDetector(z0, Math.toRadians(incline));
DetectorFrame df = new DetectorFrame(z0, incline);
for (int i = 0; i < 16; i++) {
    theta[i] = new DataSet();
    inc[i] = new DataSet();
    dist[i] = new DataSet();
}
int numberDone = 0;
int countsToBeDone = 900;
int eventCount = 0;
int hitCount = 0;
int updateInterval = 500;
int numEventsToSimulate = 100000;
while (eventCount < numEventsToSimulate) {
    d = changePhi(Direction.getRandomDirection());
    /* if (d.getTheta() < deg112 || d.getTheta() > deg166) {
        hit=false;
    } else {*/
    hit = md.isHit(d);
    //}
    eventCount++;
    if (hit) {
        hitCount++;
        int strip = md.getStrip();
        theta[strip].add(Math.toDegrees(d.getTheta()));
        inc[strip].add(md.getIncidence());
```

```
            dist[strip].add(md.getDistance());
            if (theta[strip].getSize() == countsToBeDone)
                numberDone++;
        }
        if (eventCount % updateInterval == 0
            || eventCount == numEventsToSimulate) {
            for (int strip = 0; strip < 16; strip++) {
                df.updateStrip(
                    strip,
                    theta[strip].getSize(),
                    theta[strip].getMean(),
                    theta[strip].getSD(),
                    inc[strip].getMean(),
                    inc[strip].getSD(),
                    dist[strip].getMean(),
                    dist[strip].getSD());
            }
        }
        df.updateEventCount(eventCount, hitCount);
    }
    int[][] thetaHists = new int[16][122];
    int[][] incHists = new int[16][82];
    int[][] distHists = new int[16][(110 - 75 + 1) * 5];      //just parameters for
        the file produced
    for (int strip = 0; strip < 16; strip++) {
        thetaHists[strip] = theta[strip].getHistogram(100, 170, 0.5); //likely
            more parameters
```

```
        incHists[strip] = inc[strip].getHistogram(0.8, 1.6, 0.02);
        distHists[strip] = dist[strip].getHistogram(75, 160, 0.2);
    }
    try {
        FileWriter incHist =
            new FileWriter(fileRoot + "\\incHist_" + input + ".dat");
        FileWriter thetaHist =
            new FileWriter(fileRoot + "\\thetaHist_" + input + ".dat");
        FileWriter distHist =
            new FileWriter(fileRoot + "\\dist_" + input + ".dat");
        FileWriter summary =
            new FileWriter(fileRoot + "\\monte_" + input + ".txt");
        summary.write(
            "z0 = " + z0 + " mm, incline = " + incline + " degrees\n");
        summary.write(
            "Done. All strips have at least "
                + countsToBeDone
                + " counts.\n");
        double p = (double) hitCount / (double) eventCount;
        summary.write(
            "Array Geometric Efficiency = "                    //part of
                output file
                + 2.5 * p
                + " +/- "
                + 2.5 * Math.sqrt(p * (1.0 - p) / (double) eventCount)
                + "\n");
```

```
for (int strip = 0; strip < 16; strip++) {
    summary.write(
        strip
            + "\t"
            + theta[strip].getSize()
            + "\t"
            + theta[strip].getMean()
            + "\t"
            + theta[strip].getSD()
            + "\t"
            + inc[strip].getMean()
            + "\t"
            + inc[strip].getSD()
            + "\t"
            + dist[strip].getMean()
            + "\t"
            + dist[strip].getSD()
            + "\n");
    FileWriter fw =
        new FileWriter(fileRoot + "\\monte_" + strip + ".dat");
    double[] angles = theta[strip].getData();
    double[] incid = inc[strip].getData();
    double[] distances = dist[strip].getData();
    for (int event = 0; event < angles.length; event++) {
        fw.write(
            angles[event]
                + "\t"
```

```
                + incid[event]
                + "\t"
                + distances[event]
                + "\n");
        }
        fw.flush();
        fw.close();
    }
    for (int bin = 0; bin < thetaHists[0].length; bin++) {
        thetaHist.write((110 + bin * 0.5) + "");
        for (int strip = 0; strip < 16; strip++) {
            thetaHist.write("\t" + thetaHists[strip][bin]);
        }
        thetaHist.write("\n");
    }
    for (int bin = 0; bin < incHists[0].length; bin++) {
        incHist.write((0.8 + bin * 0.02) + "");
        for (int strip = 0; strip < 16; strip++) {
            incHist.write("\t" + incHists[strip][bin]);
        }
        incHist.write("\n");
    }
    for (int bin = 0; bin < distHists[0].length; bin++) {
        distHist.write((75 + bin * 0.2) + "");
        for (int strip = 0; strip < 16; strip++) {
            distHist.write("\t" + distHists[strip][bin]);
        }
```

```
                distHist.write("\n");
            }
            thetaHist.flush();
            thetaHist.close();
            incHist.flush();
            incHist.close();
            distHist.flush();
            distHist.close();
            summary.flush();
            summary.close();
        } catch (IOException e) {
            System.err.println(e);
        }
        //Direction d=new Direction(Math.toRadians(41.7),Math.toRadians(96.5));
        //md.isHit(d);
    }
}
```

EngeSABRE_Simulation.java

```
    /*****************************************************************
 * Nuclear Simulation Java Class Libraries
 * Copyright (C) 2003 Yale University
 *
 * Original Developer
 *      Dale Visser (dale@visser.name)
 *
 * OSI Certified Open Source Software
```

```
 *
 * This program is free software; you can redistribute it and/or
 * modify it under the terms of the University of Illinois/NCSA
 * Open Source License.
 *
 * This program is distributed in the hope that it will be
 * useful, but without any warranty; without even the implied
 * warranty of merchantability or fitness for a particular
 * purpose. See the University of Illinois/NCSA Open Source
 * License for more details.
 *
 * You should have received a copy of the University of
 * Illinois/NCSA Open Source License along with this program; if
 * not, see http://www.opensource.org/
 ************************************************************/
/*
 * EngeYLSA_Simulation.java
 *
 * Created on July 2, 2001, 12:30 PM
 */

package dwvisser.monte;
import dwvisser.nuclear.*;
import java.io.*;
import java.util.Random;
import dwvisser.math.UncertainNumber;
import java.text.DecimalFormat;
```

```
/**
 * This class will produce a Monte Carlo simulation of the in-flight
 * decay of a nucleus in an excited state produced and (presumably)
 * tagged by the Enge SplitPole.  The code also determines if and where
 * the decay product interacts with YLSA.'
 *
 * Edited 6/9/15 for use with SABRE array by CMD.
 *
 * @author <a href="mailto:dale@visser.name">Dale W. Visser</a>
 * @version 1.0
 */
public class EngeSABRE_Simulation extends Object {
    static final double C_MM_PER_NSEC = 299.792458; //speed of light in the world's
        dumbest format.
    static final double DEAD_LAYER_THICKNESS = 0.5; //um. thick deadlayer are .5 um,
        the thin dead layer ones are .05 um.

    //Fields specified in constructor
    Nucleus target, beam, projectile, decay;
    double xtarg; //thickness in ug/cm^2
    double Ebeam; //beam kinetic energy in MeV
    double ExResid; //in MeV
    double ExUltimate; //in MeV
    double theta; //for spectrometer, in degrees
    String outFile;
```

```
//Fields set by calculation
Nucleus residual, ultimate;
double thetaR; //for spectrometer, in radians
FileWriter outEvn, outCounts, outDescription, outAngles;

/** Creates new EngeSABRE_Simulation */
public EngeSABRE_Simulation() {
    DataSet[] stripCMtheta = new DataSet[16];

    double[] ExResidValues = {12.049}; //value of state populated in excited
        nucleus BEFORE decay into sabre: MeV
    /*** Initial values put here ***/
    double fractionalErrorPerStrip = 0.1;
    int hitsWanted = 16 * (int) Math.pow(fractionalErrorPerStrip, -2);
    //hits wanted ~ (fractional error wanted per strip)^-2
    System.err.println(
        "Total hits wanted: "
            + hitsWanted
            + " to get "
            + (100 * fractionalErrorPerStrip)
            + "% error each strip");
    /**
     * numEvents will be expanded as needed so that hitsWanted
     * will be exceeded by approximately 20%
     */
    //int numEvents = (int) Math.round(hitsWanted * 1.2);
    int numEvents = 1000000;
```

```
//total events to simulate
double z0 = 124.54; //distance in mm to vertex of array
double thetaYLSA = 40; //angle of array detectors: back of array to detector
    face angle
try {
    target = new Nucleus(9, 19);
    beam = new Nucleus(1,1);
    projectile = new Nucleus(2, 4);
    decay = new Nucleus(2, 4);
} catch (NuclearException ne) {
    System.err.println(ne);
}

Ebeam = 10.0; //beam kinetic energy in MeV
xtarg = 120.0; //thickness in ug/cm^2
String starg = "Li_1_F_1"; //material specification for target: THE STOICH
theta = 15; //for spectrometer, in degrees
double thetaAcceptance = 0.0302;     // orig: 0.010
//choose "theta" of projectile <= +/- this
double phiAcceptance = 0.040; //choose "phi" of projectile <= +/- this
        //orig: 0.040 is maximum opening...
double randomAcceptanceMax =
    Math.sqrt(
        Math.pow(thetaAcceptance, 2) + Math.pow(phiAcceptance, 2));
ExUltimate = 0.0; //in MeV. Excited state in Final Nucleus.
int angularMomentum = 0;
//assumed orbital angular momentum for the decay
```

```
double AlThickness = 0;
//thickness of degrading foil in front of detector in mils
//at this time, simply added to dead layer thickness, assuming we would
//put the foils parallel to the detectors
double hit_threshold = 0.0;
//energy deposited in MeV to be considered a hit
int[] counts = new int[90];
double[] Emin = new double[90];
double[] Emax = new double[90];
boolean arrayForward = false;

/*** Calculation of some fields based on initial values ***/
for (int rEx = 0; rEx < ExResidValues.length; rEx++) {
    for (int i = 0; i < stripCMtheta.length; i++) {
        stripCMtheta[i] = new DataSet();
    }
    ExResid = ExResidValues[rEx]; //in MeV
    try {
        residual =
            new Nucleus(
                target.Z + beam.Z - projectile.Z,
                target.A + beam.A - projectile.A,
                ExResid);
        ultimate =
            new Nucleus(
                residual.Z - decay.Z,
                residual.A - decay.A,
```

```
                ExUltimate);
} catch (NuclearException ne) {
    System.err.println(ne);
}

String whetherForward = "_back";
if (arrayForward)
    whetherForward = "_front";
String outFileRoot =
      //System.getProperty("user.home")+File.separator+
      "/Users/eringood/Desktop/SPS_Code/mcSims/"
        + (int) Math.round(ExResid * 1000)
        + "_"
        + residual
        + "_"
        + (int) Math.round(ExUltimate * 1000)
        + "_"
        + ultimate
        + "_L"
        + angularMomentum
        + whetherForward
        + "_"
        + AlThickness
        + "mil"
        + (int) Math.round(Ebeam)
        + "MeV"
        + "_"
```

```
            + theta
            + "deg";
    thetaR = Math.toRadians(theta);
    System.out.println(
        target
            + "("
            + beam
            + ","
            + projectile
            + ") -> "
            + ultimate
            + "+"
            + decay);
    System.out.println("File root: " + outFileRoot);
    try {
        outDescription = new FileWriter(outFileRoot + ".txt");
        outEvn = new FileWriter(outFileRoot + ".csv");
        outCounts = new FileWriter(outFileRoot + ".sum");
        outAngles = new FileWriter(outFileRoot + ".ang");
    } catch (IOException ioe) {
        System.err.println(ioe);
    }

    Random random = new Random();
    double Mresid = residual.getMass().value;
    double Mdecay = decay.getMass().value;
    double Mdecay2 = Mdecay * Mdecay;
```

```
double Multimate = ultimate.getMass().value;
double excess = Mresid - Multimate - Mdecay;
try {
    if (excess < 0) {
        throw new NuclearException(
            "Mass of final system is "
                + (-excess)
                + " MeV above the state.");
    }
    double Multimate2 = Multimate * Multimate;
    double PcmDecay =
        Math.sqrt(
            Mresid * Mresid
                - 2 * (Mdecay2 + Multimate2)
                + Math.pow((Mdecay2 - Multimate2) / Mresid, 2))
            / 2;
    //MeV/c
    double EcmDecay =
        Math.sqrt(PcmDecay * PcmDecay + Mdecay * Mdecay);
    System.out.println(
        "Ex = "
            + ExResid
            + " MeV, CM K.E. for detected decay product = "
            + (EcmDecay - Mdecay)
            + " MeV");
    MicronDetector md =
        new MicronDetector(z0, Math.toRadians(thetaYLSA));
```

```
Solid deadLayer;
EnergyLoss deadLayerLoss;


outDescription.write(
    target
        + "("
        + beam
        + ","
        + projectile
        + ")"
        + residual
        + "("
        + decay
        + ")"
        + ultimate
        + "\n");
outDescription.write(
    "Ex(residual " + residual + ") = " + ExResid + " MeV\n");
outDescription.write(
    "Ex(final " + ultimate + ") = " + ExUltimate + " MeV\n");
outDescription.write(
    "Theta(projectile "
        + projectile
        + ") = "
        + theta
        + " degrees\n");
outDescription.write(
```

```
        "Target Thickness = " + xtarg + " ug/cm^2\n");
    outDescription.write("l = " + angularMomentum + " decay\n");
    deadLayer =
        new Solid(getThicknessAl(AlThickness), Absorber.CM, "Al");
    deadLayerLoss = new EnergyLoss(deadLayer);



    double[] p_CM = new double[4];
    double[] p_lab = new double[4];
    /*** work begins here ***/
    Reaction reaction;
    Boost labBoost;
    Direction directionCM;
    int angleBinning = 60;
    double divFactor = 180.0 / angleBinning;
    int[] thetaCM = new int[angleBinning];
    int[] thetaLab = new int[angleBinning];
    int hits = 0;
    outEvn.write(
        "hit,projTheta,projPhi,CMtheta,CMphi,labTheta,labPhi,inc.,Edep,tof
            ,det,strip\n");
    int _i = 0;
    /*for (int i=0; i < numEvents; i++)*/
    do {
        _i++;
        //System.out.println(_i + "made it here!");
```

```
double depth = random.nextDouble() * xtarg;
Solid targetMatter = new Solid(starg, depth);
EnergyLoss targetLossCalc = new EnergyLoss(targetMatter);
double targetLoss =
    0.001 * targetLossCalc.getEnergyLoss(beam, Ebeam);
double Tbeam = Ebeam - targetLoss;

//Direction _randomProjDir = new Direction(0,0);

//randomly select a direction into the spectrometer
//assuming its slits are centered on the beam axis
Direction projDir = null;
boolean directionAccepted = false;
while (!directionAccepted) {
    Direction _randomProjDir =
        Direction.getRandomDirection(
            0,
            randomAcceptanceMax);
    //"theta" for theta acceptance actually arcTan(x/z) or tan("
      theta")=
    //tan(theta)cos(phi)
    double tempTanTheta =
        Math.abs(
            Math.tan(_randomProjDir.getTheta())
                * Math.cos(_randomProjDir.getPhi()));
    double tempTanPhi =
        Math.abs(
```

```
                Math.tan(_randomProjDir.getTheta())
                    * Math.sin(_randomProjDir.getPhi()));
        directionAccepted =
            (tempTanTheta <= Math.tan(thetaAcceptance))
                && (tempTanPhi <= Math.tan(phiAcceptance));
        //directionAccepted = true;
        if (directionAccepted) {
            //rotate random direction to be about actual spectrometer
                location
            //theta = angle the spectrometer is set at
            projDir =
                _randomProjDir.rotateY(Math.toRadians(theta));
        }
        //else{System.out.println("problem here");}
    }



    //create reaction for theta from projDir
    reaction =
        new Reaction(
            target,
            beam,
            projectile,
            Tbeam,
            projDir.getThetaDegrees(),
            ExResid);
```

```
//determine direction residual nucleus is moving
//theta comes from reaction object, (taking absolute value, as the
    minus
//sign usually returned causes the new phi to be calculated wrong)
//phi is opposite the phi of the projectile
Direction residDir =
    new Direction(
        Math.toRadians(
            Math.abs(reaction.getLabAngleResidual(0))),
        Math.PI + projDir.getPhi());
//create boost object to convert CM 4-momentum to lab 4-momentum
labBoost =
    new Boost(reaction.getLabBetaResidual(0), residDir);
if (!arrayForward)
    labBoost = Boost.inverseBoost(labBoost);
//consider l=angularMomentum case:
//The assumption is theta = 0 degrees exactly for the projectile
//(not exactly true, of course) so that the correlation function
//is just a Legendre Polynomial (corresponding to only M=0
//being populated.
directionCM = Direction.getRandomDirection(angularMomentum);
//copy components of momentum into 4-vector
p_CM[0] = EcmDecay;
System.arraycopy(
    directionCM.get3vector(PcmDecay),
    0,
    p_CM,
```

```
        1,
        3);
    p_lab = labBoost.transformVector(p_CM);
    //extract direction of decay product in lab
    Direction directionLab =
        new Direction(p_lab[1], p_lab[2], p_lab[3]);
    //???rotating on this next line was the wrong thing to do, I think
    /*directionLab = directionLab.rotateY(
    Math.toRadians(reaction.getLabAngleResidual(0)));*/
    Direction queryDir = MicronDetector.changePhi(directionLab);
    boolean hit = md.isHit(queryDir);
    int strip, det;
    double Edep, tof;
    if (arrayForward) {
        directionLab =
            new Direction(
                Math.PI - directionLab.getTheta(),
                directionLab.getPhi());
        directionCM =
            new Direction(
                Math.PI - directionCM.getTheta(),
                directionCM.getPhi());
    }
    double thetaDlab = directionLab.getThetaDegrees();
    double thetaDcm = directionCM.getThetaDegrees();
    thetaCM[(int) Math.floor(thetaDcm / divFactor)]++;
    thetaLab[(int) Math.floor(thetaDlab / divFactor)]++;
```

```
if (hit) {
    //System.out.println(_i + "is hit");
    strip = md.getStrip();
    det = MicronDetector.getDetector(directionLab);
    int bin = strip + det * 16;
    double incidence = md.getIncidence();
    double Tinit = p_lab[0] - Mdecay;
    double Tflight =
        Tinit
            - 0.001
                * targetLossCalc.getEnergyLoss(
                    decay,
                    Tinit,
                    Math.PI - directionLab.getTheta());
    tof =
        md.getDistance()
            / (Reaction.getBeta(decay, Tflight)
                * C_MM_PER_NSEC);
    Edep =
        Tflight
            - 0.001
                * deadLayerLoss.getEnergyLoss(
                    decay,
                    Tflight,
                    Math.acos(1 / incidence));
    boolean energyHit = Edep >= hit_threshold;
    if (energyHit) {
```

```
stripCMtheta[strip].add(thetaDcm);
hits++;
counts[bin]++;
if (Emin[bin] == 0.0 || Emin[bin] > Edep)
    Emin[bin] = Edep;
if (Emax[bin] == 0.0 || Emax[bin] < Edep)
    Emax[bin] = Edep;
//time-of-flight in nsec
outEvn.write(
    "1,"
        + round(projDir.getThetaDegrees())
        + ","
        + round(projDir.getPhiDegrees())
        + ","
        + round(thetaDcm)
        + ","
        + round(directionCM.getPhiDegrees())
        + ","
        + round(thetaDlab)
        + ","
        + round(directionLab.getPhiDegrees())
        + ","
        + round(incidence)
        + ","
        + round(Edep)
        + ","
        + round(tof)
```

```
                + ","
                + det
                + ","
                + strip
                + "\n");
        } /*else {
            outEvn.write(
                "0,"
                    + round(projDir.getThetaDegrees())
                    + ","
                    + round(projDir.getPhiDegrees())
                    + ","
                    + round(thetaDcm)
                    + ","
                    + round(directionCM.getPhiDegrees())
                    + ","
                    + round(thetaDlab)
                    + ","
                    + round(directionLab.getPhiDegrees())
                    + ","
                    + round(incidence)
                    + ","
                    + round(Edep)
                    + ","
                    + round(tof)
                    + ","
                    + det
```

```
                    + ","
                    + strip
                    + "\n");
        }*/
    } /*else {
        outEvn.write(
            "0,"
                + round(projDir.getThetaDegrees())
                + ","
                + round(projDir.getPhiDegrees())
                + ","
                + round(thetaDcm)
                + ","
                + round(directionCM.getPhiDegrees())
                + ","
                + round(thetaDlab)
                + ","
                + round(directionLab.getPhiDegrees())
                + ",,,,,"
                + "\n");
    }*/
    if (_i % 1000 == 0) {
        System.out.println(_i + ":" + hits);
    }
    if (_i == numEvents && hits < hitsWanted) {
        numEvents =
            (int) Math.round(
```

```
                1.2 * (double) _i / (double) hits * hitsWanted);
        System.out.println(
            "Events so far = " + _i + ", " + hits + " hits.");
        System.out.println(
            "Changing total events to simulate to "
                + numEvents
                + ".");
    }
}



while (_i < numEvents);
outEvn.flush();
outEvn.close();
outCounts.write("bin\tdet\tstrip\tcounts\tEmin\tEmax\n");


for (int i = 0; i < 5; i++) {
    for (int j = 0; j < 16; j++) {
        int bin = i * 16 + j;
        outCounts.write(
            bin
                + "\t"
                + i
                + "\t"
                + j
```

```
                    + "\t"
                    + counts[bin]
                    + "\t"
                    + round(Emin[bin])
                    + "\t"
                    + round(Emax[bin])
                    + "\n");
        }
    }
    outAngles.write("Theta\tCMcounts\tlabCounts\n");
    for (int i = 0; i < angleBinning; i++) {
        outAngles.write(
            (i * 180 / angleBinning)
                + "\t"
                + round(thetaCM[i])
                + "\t"
                + round(thetaLab[i])
                + "\n");
    }
    outAngles.flush();
    outAngles.close();
    outCounts.flush();
    outCounts.close();
    System.out.println(
        "Done. "
            + hits
            + " detector hits for "
```

```
            + _i
            + "␣simulated␣decays.");
    outDescription.write(_i + "␣simulated␣events\n");
    outDescription.write(hits + "␣hits\n");
    double efficiency = (double) hits / (double) _i;
    double delEff = Math.sqrt((double) hits) / (double) _i;
    UncertainNumber uncEff =
        new UncertainNumber(efficiency, delEff);
    outDescription.write("total␣efficiency:␣" + uncEff + "\n");
    outDescription.write("\nStrip\tCMtheta\thits\tEff\tdelEff\n");
    for (int i = 0; i < stripCMtheta.length; i++) {
        int _hits = stripCMtheta[i].getSize();
        double _eff = (double) _hits / _i;
        double _deleff = Math.sqrt(_hits) / _i;
        outDescription.write(
            i
                + "\t"
                + round(stripCMtheta[i].getMean())
                + "\t"
                + _hits
                + "\t"
                + _eff
                + "\t"
                + _deleff
                + "\n");
    }
    outDescription.flush();
```

```
            outDescription.close();
        } catch (KinematicsException ke) {
            System.err.println(ke);
        } catch (NuclearException ke) {
            System.err.println(ke);
        } catch (dwvisser.math.MathException me) {
            System.err.println(me);
        } catch (IOException ioe) {
            System.err.println(ioe);
        }
    }
}

static private String round(double number) {
    DecimalFormat dm = new DecimalFormat("##.###");
    return dm.format(number);
}

/**
 * Returns thickness of Al in front of active region in cm (foil plus dead layer).
 * @param foilThickness in mils
 */
private double getThicknessAl(double foilThickness) {
    double detectorDeadLayer = DEAD_LAYER_THICKNESS * 1.0e-4;
    //in cm, i.e. 0.2 um
    double thicknessInCM = foilThickness / 1000 * 2.54;
    return thicknessInCM + detectorDeadLayer;
```

```
    }

    static public void main(String[] args) {
        new EngeSABRE_Simulation();
        //System.out.println(Math.toDegrees(0.160));
        //System.out.println(Math.toDegrees(0.080));
    }
}
```

Appendix B: How to Use the Monte Carlo Simulation

Files and Tools Required

The code was written in the java environment by Dale Visser for the YLSA array and is part of a larger suite of software designed for the SPS when it was at the WNSL; it has since been updated to work for the SABRE array. Typically Eclipse IDE is the platform used to run and edit the code. When opening Eclipse, select the folder that contains all required code as your workspace. This should open up all the files you need. A copy of the required code can be obtained from the LSU experimental nuclear physics group.

The code needed for these simulations is in the `Astro Code SABRE` folder in the eclipse environment, in the subfolder/package `dwvisser.monte`. The files needed are:

- `DataSet.java`
- `DetectorFrame.java`
- `Direction.java`
- `EngeSABRE_Simulation.java`
- `MicronDetector.java`
- `RandomNumbers.java`
- `WeightingFunction.java`

Files `DataSet.java`, `Direction.java`, `RandomNumbers.java`, and `WeightingFunction.java` remain unchanged from the earliest versions of the simulation. Files `DetectorFrame.java` and `MicronDetector.java` were edited to have the dimensions of the SABRE array and should not need to be changed.

The file that needs changes for different simulations is `EngeSABRE_Simulation.java`. Here, reaction information as well as some information about the setup is given as input.

Required Input to the `EngeSABRE_Simulation.java` File

a. Reaction Information

Line 70: `ExResidValues = {9.844};` This is the energy (in MeV) of the state populated in the excited nucleus BEFORE it decays into SABRE.

Lines 91 to 94: `target, beam, projectile, decay`. These are the (A, Z) values of the nuclei mentioned. The target and beam are self-explanatory, though if it's a combined target like LiF, use the nucleus the reaction is proceeding on. The projectile is the particle of interest detected in the focal plane detector, or the light reaction byproduct, and the decay is is the charged particle that decays into SABRE from the excited nucleus remaining in the target.

Line 99: `Ebeam = 10.0;` Beam energy in MeV.

Line 100: `xtarg = 100.0;` Target thickness in μg/cm^2.

Line 101: `starg = "Li 1 F 1";` This is the stoichiometry of the target.

Line 109: `ExUltimate = 0.0;` The energy of the (excited) state in the final nucleus—i.e. the daughter nucleus resulting from the charged-particle decay into SABRE.

Line 110: `angularMomentum = 2;` The assumed angular momentum of the decay particle detected in SABRE, or the *l*-value.

b. Setup and Detector Information

Line 50: `DEAD_LAYER_THICKNESS = 0.5;` This line describes the dead layer of the detectors in micrometers [μ m]. The thick (400 μm thick total) and thin dead layer (500 μm thick total) sets of MMMs have different deadlayer thicknesses. Be aware that the thicker dead layer detectors are actually thinner overall.

Line 102: `theta = 15;` This is the angle the spectrograph is set to.

Line 103: `thetaAcceptance = 0.0302;` This is the acceptance of the X-direction slits into the spectrometer in radians.

Line 104: `phiAcceptance = 0.040;` This is the acceptance of the Y-direction slits into the spectrometer in radians.

c. Numerical and Simulation Quantities

Line 72: `fractionalErrorPerStrip = 0.1;` This is the amount of efficiency error desired in each detector strip. Here 0.1 indicates 10% error in each strip.

Line 86: `numEvents = 40000;` This is the total number of events to be simulated.

d. File Output

Line 149: `outFileRoot = "Users/yourname/Desktop/"` This is where the simulation output files will be written. Write the full path or the code may give an error.

How to Run the Simulation

Go to the `EngeSABRE_Simulation.java` file and hit the green "play" button on the top Eclipse toolbar. A warning window will pop up with a message: `Errors exist in required project(s)`. The errors message is most likely due to errors in unused files. Hit the `Proceed` button and it should run. If not, check any altered files listed in the first section for errors.

The output files (described below) will be output to the directory specified above when finished.

Output Files

There are four output files created, which will be named identically based on the input parameters chosen except for their extensions: `*.ang`, `*.csv`, `*.sum`, and `*.txt`.

The `*.ang` file is not a useful file.

The `*.csv` file contains a record of every simulated event and information about every hit in the detector:

- `projTheta`, `projPhi`: theta and phi of the projectile
- `CMtheta`, `CMphi`: theta and phi in the center of mass frame
- `labTheta`, `labPhi`: theta and phi in the lab frame

- `inc.`: incidence angle (likely of projectile)
- `Edep`: energy deposited in the Si (MeV)
- `tof`: time of flight of decaying particle
- `det`: detector number in array
- `strip`: strip number in detector front

The `*.sum` file gives a record of all simulated events that hit the detectors for each strip of each detector in the array:

- `bin`: counts the number of total strips
- `det`: detector number (starts at zero; the bottom detector is detector 4 and it goes counter-clockwise around the circle in numerical order: 4, 0, 1, 2, 3)
- `strip`: strip number on the detector
- `counts`: counts in that strip during the simulation
- `Emin`: minimum energy detected in that strip (MeV) during the simulation
- `Emax`: maximum energy detected in that strip (MeV)

The `*.txt` file gives a brief summary of what you entered into the simulation as the reaction parameters and then outputs the total efficiency. Additionally, it gives you the following columns which apply to all five detectors:

- `Strip`: the strip number on the detectors
- `CMtheta`: angle of the strip in center of mass frame
- `hits`: total number of hits for all detector strips of that number

- `Eff`: efficiency for that strip in all detectors (one strip's efficiency would be this number divided by five)
- `delEff`: the uncertainty in the efficiency value from the previous column

Additional Notes

Be aware that the value `z0` in the `MicronDetector.java` and `EngeSABRE_Simulation.java` files is a measurement which has some associated uncertainty. I recommend varying this value up and down by 5mm to account for error in the measurement if you need a measure of the systematic uncertainty of the simulation. The same applies to the `thetaYLSA` variable on line 89 of the `EngeSABRE_Simulation.java` file and the `incline` variable on line 226 of the `MicronDetector.java` file. Similarly, I recommend varying this value up and down by 3 degrees to account for variation of the placement of the detectors if you need a measure of the systematic uncertainty of the simulation.

Appendix C: Angular Fits of Aluminum Data

7.832 MeV

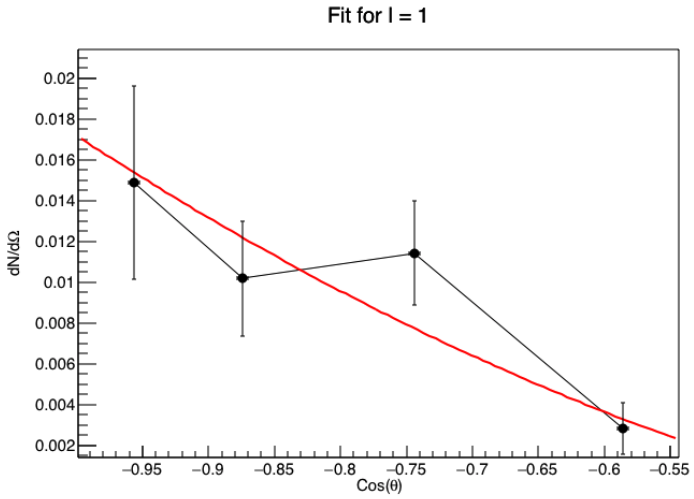

Figure C.1. The decay of the 7.832 MeV state to the ground state of ^{26}Al was fit with an $l = 1$ distribution with a chi-squared value of 2.72. The A_0 coefficient was 0.0031(13).

8.210 MeV

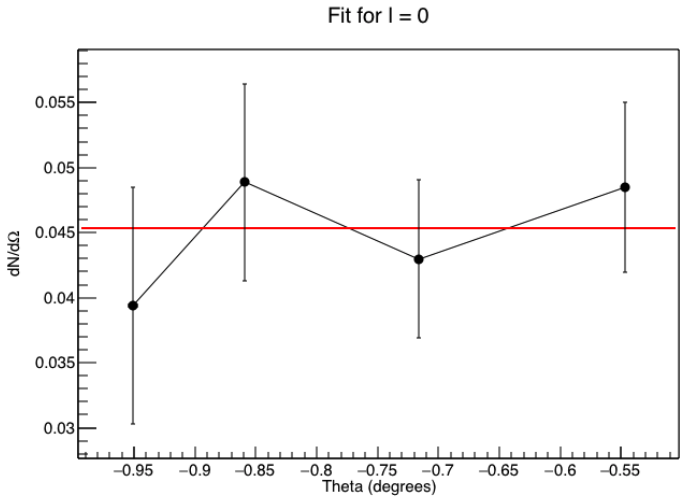

Figure C.2. The decay of the 8.210 MeV state to the ground state of ^{26}Al was fit with an $l = 0$ distribution with a chi-squared value of 1.03. The A_0 coefficient was 0.0453(35).

8.299 MeV

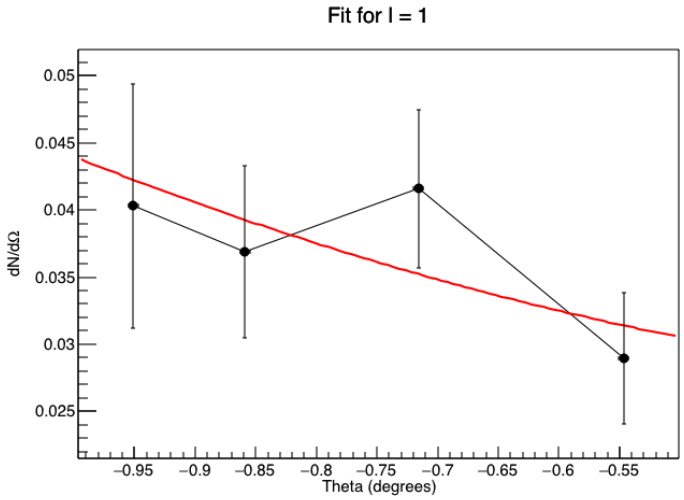

Figure C.3. The decay of the 8.299 MeV state to the ground state of ^{26}Al was fit with an $l = 1$ distribution with a chi-squared value of 1.61. The A_0 coefficient was 0.0320(41).

8.354 MeV

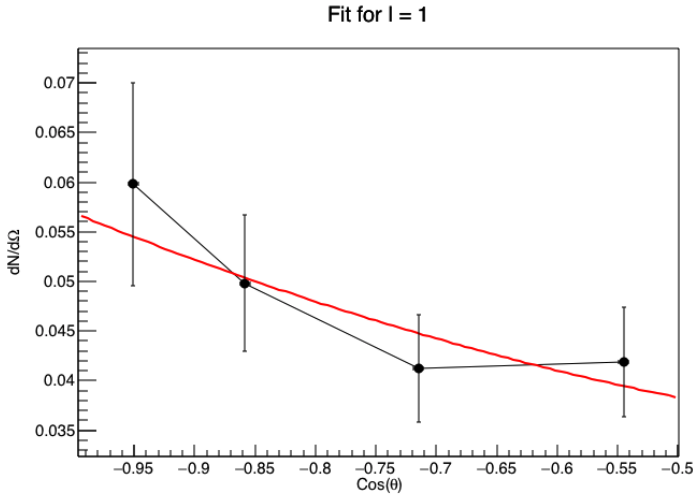

Figure C.4. The decay of the 8.354 MeV state to the ground state of ^{26}Al was fit with an $l = 1$ distribution with a chi-squared value of 0.893. The A_0 coefficient was 0.0404(44).

8.375 MeV

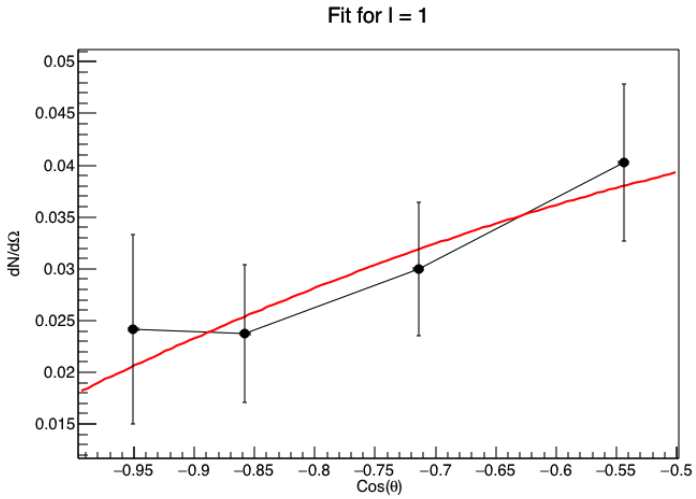

Figure C.5. The decay of the 8.375 MeV state to the ground state of ^{26}Al was fit with an $l = 1$ distribution with a chi-squared value of 0.383. The A_0 coefficient was 0.0369(58).

8.486 MeV

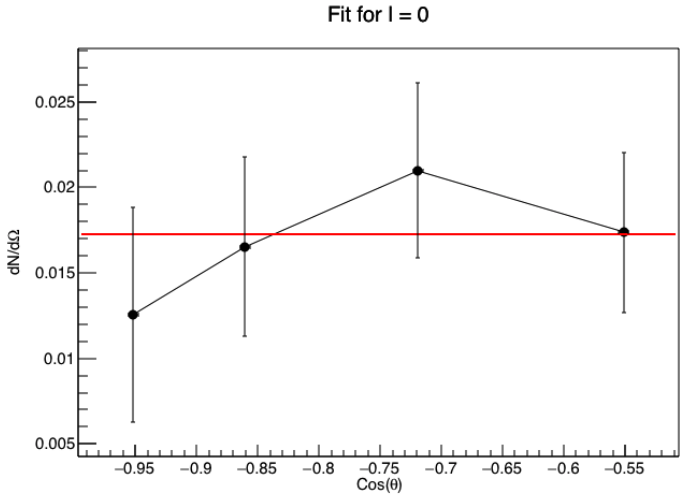

Figure C.6. The decay of the 8.486 MeV state to the isomer state of ^{26}Al was fit with an $l = 0$ distribution with a chi-squared value of 1.11. The A_0 coefficient was 0.0173(26).

8.486 MeV

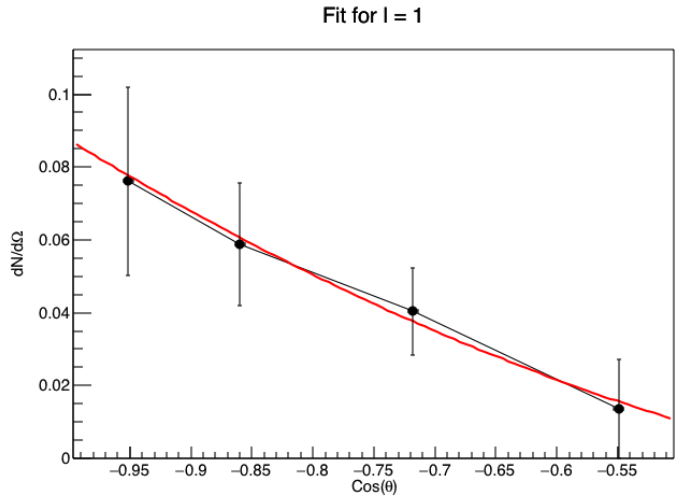

Figure C.7. The decay of the 8.486 MeV state to the isomer state of ^{26}Al was fit with an $l = 1$ distribution with a chi-squared value of 0.0936. The A_0 coefficient was 0.0189(11).

8.557 MeV

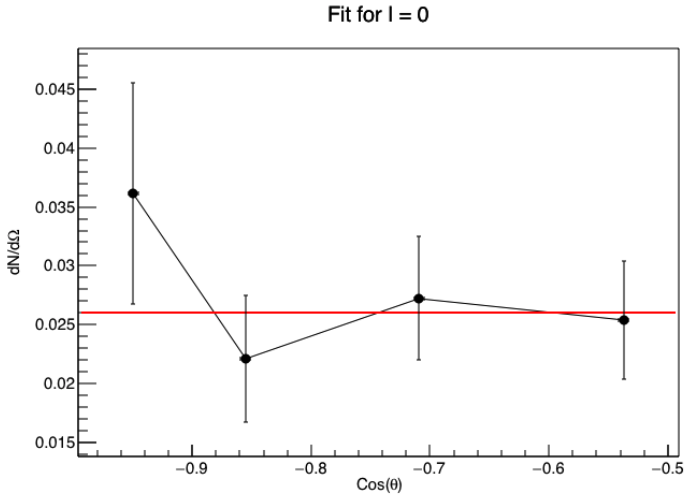

Figure C.8. The decay of the 8.557 MeV state to the ground state of ^{26}Al was fit with an $l = 0$ distribution with a chi-squared value of 1.77. The A_0 coefficient was 0.0260(29).

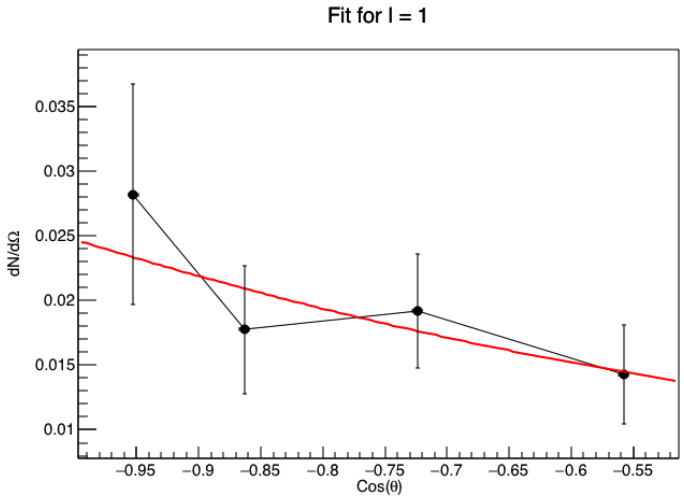

Figure C.9. The decay of the 8.557 MeV state to the second-excited state of ^{26}Al was fit with an $l = 1$ distribution with a chi-squared value of 0.861. The A_0 coefficient was 0.0148(33).

8.586 MeV

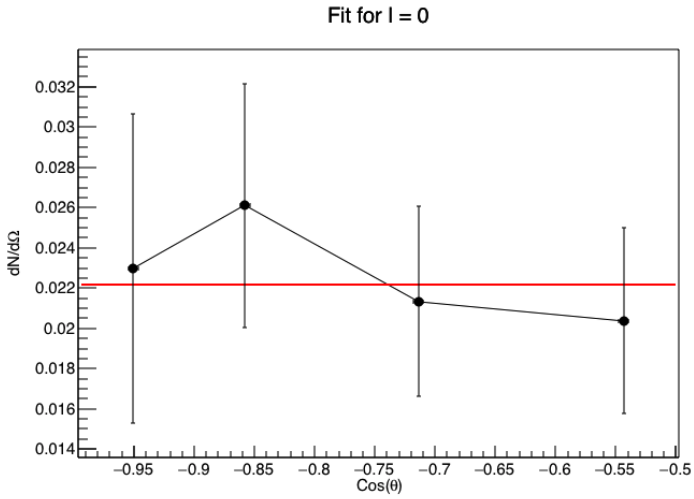

Figure C.10. The decay of the 8.586 MeV state to the isomer state of ^{26}Al was fit with an $l = 0$ distribution with a chi-squared value of 0.619. The A_0 coefficient was 0.0222(27).

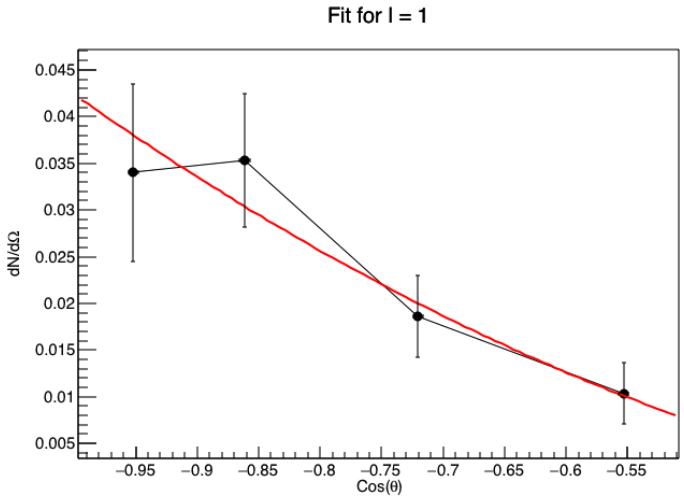

Figure C.11. The decay of the 8.586 MeV state to the second-excited state of ^{26}Al was fit with an $l = 1$ distribution with a chi-squared value of 0.749. The A_0 coefficient was 0.0114(29).

8.668 MeV

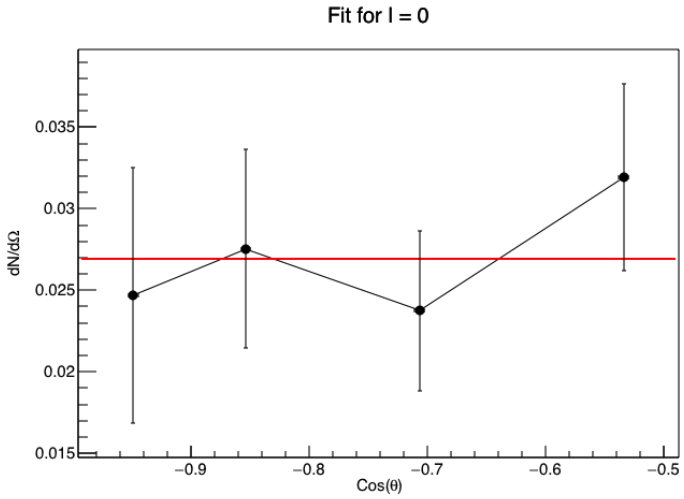

Figure C.12. The decay of the 8.668 MeV state to the ground state of ^{26}Al was fit with an $l = 0$ distribution with a chi-squared value of 1.28. The A_0 coefficient was 0.0269(30).

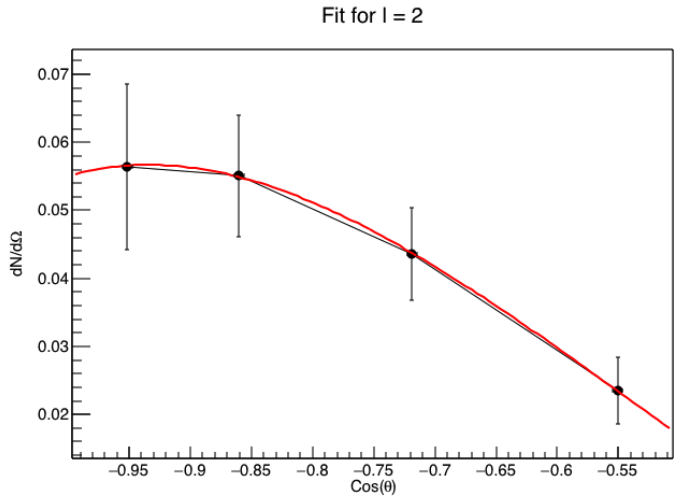

Figure C.13. The decay of the 8.668 MeV state to the second-excited state of ^{26}Al was fit with an $l = 2$ distribution with a chi-squared value of 0.000690. The A_0 coefficient was 0.0178(10).

8.864 MeV

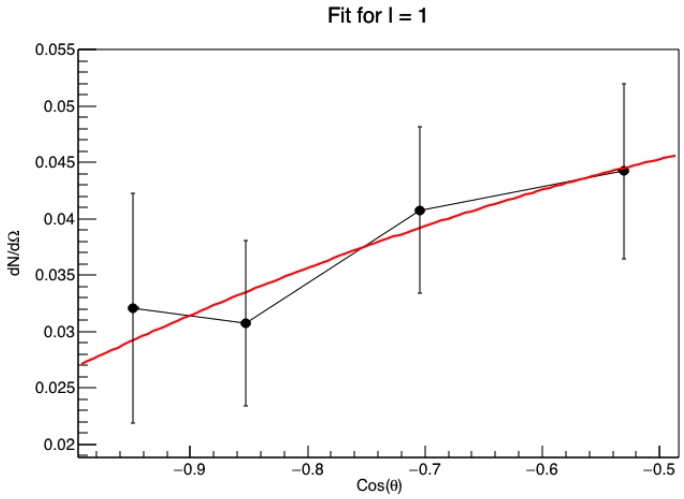

Figure C.14. The decay of the 8.864 MeV state to the ground state of ^{26}Al was fit with an $l = 1$ distribution with a chi-squared value of 0.267. The A_0 coefficient was 0.0432(59).

8.931 MeV

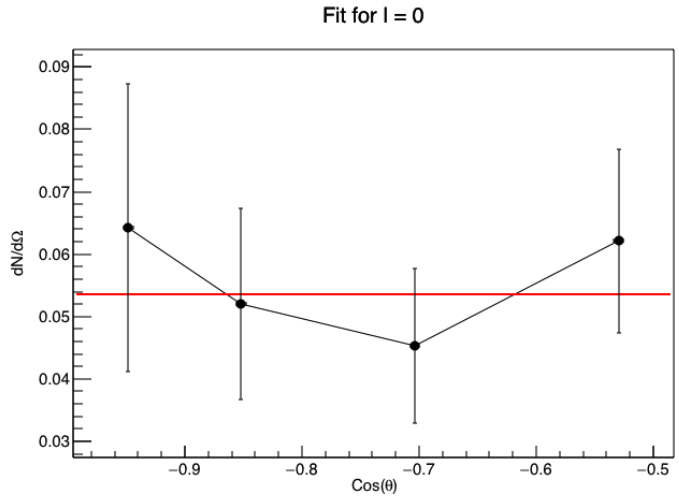

Figure C.15. The decay of the 8.931 MeV state to the ground state of ^{26}Al was fit with an $l = 0$ distribution with a chi-squared value of 1.01. The A_0 coefficient was 0.0535(76).

8.984 MeV

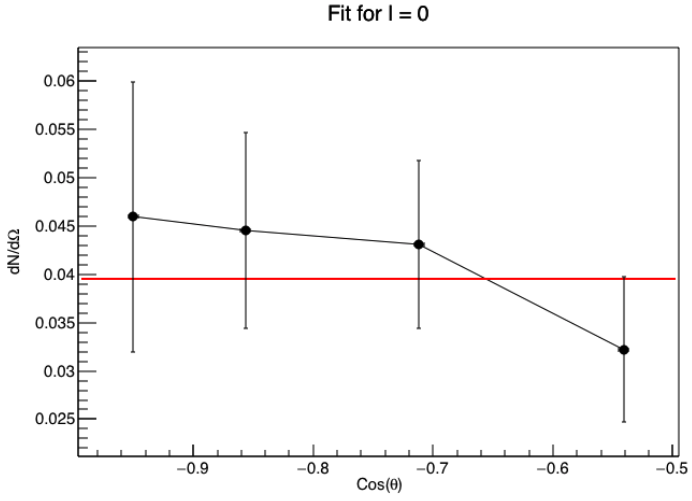

Figure C.16. The decay of the 8.984 MeV state to the second-excited state of ^{26}Al was fit with an $l = 0$ distribution with a chi-squared value of 1.57. The A_0 coefficient was 0.0395(47).

References

[1] Rudolf Kippenhahn, Alfred Weigert, and Achim Weiss. *Stellar Structure and Evolution*. Astronomy and Astrophysics Library. Springer Berlin Heidelberg, Berlin, Heidelberg, 2012.

[2] Francis Xavier Timmes. Burn hydrogen. `http://cococubed.asu.edu/code_pages/burn_hydrogen.shtml`. Accessed: 2020-05-08.

[3] Jordi Jos, Fermn Moreno, Anuj Parikh, and Christian Iliadis. HYDRODYNAMIC MODELS OF TYPE I X-RAY BURSTS: METALLICITY EFFECTS. *The Astrophysical Journal Supplement Series*, 189(1):204–239, July 2010.

[4] G.C. Anupama. Recurrent Novae: What Do We Know About Them? In *Binary Paths to Type Ia Supernovae Explosions Proceedings IAU Symposium No. 281*, pages 154–161, 2011.

[5] Jordi Jose and Margarita Hernanz. Nucleosynthesis in Classical Novae: CO versus ONe White Dwarfs. *The Astrophysical Journal*, 494(2):680–690, February 1998.

[6] Jordi Jose. Supplementary Material for Stellar Explosions: Hydrodynamics and Nucleosynthesis. `http://www.fen.upc.edu/users/jjose/CRC-Downloads.html`, 2016.

[7] C. Iliadis et al. The effects of thermonuclear reaction-rate variations on nova nucleosynthesis: A sensitivity study. *Astrophys. J. Suppl. S.*, 142(1):105, 2002.

[8] T. Lee, D.A. Papanastassiou, and G.J. Wasserburg. Aluminum-26 in the early solar-system: Fossil or fuel? *Astrophys. J. (Lett.)*, 211:L107 – 110, 1977.

[9] Jordi Jose, Margarita Hernanz, Sachiko Amari, and Katharina Lodders. THE IMPRINT OF NOVA NUCLEOSYNTHESIS IN PRESOLAR GRAINS. page 15.

[10] Jordi JOs and Margarita Hernanz. The origin of presolar nova grains. *Meteoritics & Planetary Science*, 42(7-8):1135–1143, August 2007.

[11] Larry R. Nittler and Peter Hoppe. Are Presolar Silicon Carbide Grains from Novae Actually from Supernovae? *The Astrophysical Journal*, 631(1):L89–L92, September 2005.

[12] E. Margaret Burbidge, G.R. Burbidge, William A. Fowler, and F. Hoyle. Synthesis of the Elements in Stars. *Reviews of Modern Physics*, 29(4), October 1957.

[13] W. A. Mahoney et al. HEAO 3 discovery of Al-26 in the interstellar medium. *Astrophys. J.*, 286:578–585, November 1984.

[14] R. Diehl et al. COMPTEL observations of Galactic ^{26}Al emission. *Astronomy and Astrophysics*, 298:445, June 1995.

[15] R. Diehl et al. ^{26}Al in the inner Galaxy. Large-scale spectral characteristics derived with SPI/INTEGRAL. *Astronomy and Astrophysics*, 449:1025–1031, April 2006.

[16] Roland Diehl. Massive-Star Nucleosynthesis and INTEGRAL. In *Proceedings of 8th INTEGRAL Workshop: The Restless Gamma-ray Universe PoS(INTEGRAL 2010)*, page 022, Dublin Castle, Dublin, Ireland, November 2011. Sissa Medialab.

[17] M. B. Bennett, C. Wrede, K. A. Chipps, J. Jos, S. N. Liddick, M. Santia, A. Bowe, A. A. Chen, N. Cooper, D. Irvine, E. McNeice, F. Montes, F. Naqvi, R. Ortez, S. D. Pain, J. Pereira, C. Prokop, J. Quaglia, S. J. Quinn, S. B. Schwartz, S. Shanab, A. Simon, A. Spyrou, and E. Thiagalingam. Classical-Nova Contribution to the Milky Way's ^{26}Al Abundance: Exit Channel of the Key ^{25}Al$(p,\gamma)^{26}$Si Resonance. *Physical Review Letters*, 111(23):232503, December 2013.

[18] Jordi José, Margarita Hernanz, and Alain Coc. New Results on ^{26}Al Production in Classical Novae. *Astrophys J. (Lett.)*, 479(1):L55, 1997.

[19] M. Hernanz et al. On the contribution of classical novae to the ^{26}Al content of the Galaxy. In *International Symposium on Nuclear Astrophysics - Nuclei in the Cosmos*, page 115.1, 2006.

[20] H. Schatz et al. rp-process Nucleosynthesis at Extreme Temperature and Density Conditions. *Physics Reports*, 294(4):167 – 263, 1998.

[21] Claus E. Rolfs and William S. Rodney. *Cauldrons in the Cosmos*. The University of Chicago Press, 1988.

[22] Christian Iliadis. *Nuclear Physics of Stars*. Wiley-VCH, 2015.

[23] A. Kankainen, P. J. Woods, F. Nunes, C. Langer, H. Schatz, V. Bader, T. Baugher, D. Bazin, B. A. Brown, J. Browne, D. T. Doherty, A. Estrade, A. Gade, A. Kontos, G. Lotay, Z. Meisel, F. Montes, S. Noji, G. Perdikakis, J. Pereira, F. Recchia, T. Redpath, R. Stroberg, M. Scott, D. Seweryniak, J. Stevens, D. Weisshaar, K. Wimmer, and R. Zegers. Angle-integrated measurements of the ^{26}Al$(d,n)^{27}$Si reaction cross section: a probe of spectroscopic factors and astrophysical resonance strengths. *The European Physical Journal A*, 52(1):6, January 2016.

[24] S.D. Pain, D.W. Bardayan, J.C. Blackmon, S.M. Brown, K.Y. Chae, K.A. Chipps, J.A. Cizewski, K.L. Jones, R.L. Kozub, J.F. Liang, C. Matei, M. Matos, B.H. Moazen, C.D. Nesaraja, J. Okorowicz, P.D. OMalley, W.A. Peters, S.T. Pittman, M. Pzoszajczak, K.T. Schmitt, J.F. Shriner, D. Shapira, M.S. Smith, D.W. Stracener, and G.L. Wilson. Constraint of the Astrophysical ^{26}Al$^{g}(p,\gamma)^{27}$Si Destruction Rate at Stellar Temperatures. *Physical Review Letters*, 114(21):212501, May 2015.

[25] C. Ruiz, A. Parikh, J. Jos, L. Buchmann, J. A. Caggiano, A. A. Chen, J. A. Clark, H. Crawford, B. Davids, J. M. D?Auria, C. Davis, C. Deibel, L. Erikson, L. Fogarty, D. Frekers, U. Greife, A. Hussein, D. A. Hutcheon, M. Huyse, C. Jewett, A. M. Laird, R. Lewis, P. Mumby-Croft, A. Olin, D. F. Ottewell, C. V. Ouellet, P. Parker, J. Pearson, G. Ruprecht, M. Trinczek, C. Vockenhuber, and C. Wrede. Measurement of the $E_{c.m.}$ = 184keV Resonance Strength in the ^{26}Al$^{g}(p,\gamma)^{27}$Si Reaction. *Physical Review Letters*, 96(25):252501, June 2006.

[26] S. Almaraz-Calderon, K.E. Rehm, N. Gerken, M.L. Avila, B.P. Kay, R. Talwar, A.D. Ayangeakaa, S. Bottoni, A.A. Chen, C.M. Deibel, C. Dickerson, K. Hanselman, C.R. Hoffman, C.L. Jiang, S.A. Kuvin, O. Nusair, R.C. Pardo, D. Santiago-Gonzalez, J. Sethi, and C. Ugalde. Study of the ^{26}Al$^{m}(d,p)^{27}$Al Reaction and the Influence of the ^{26}Al 0+ Isomer on the Destruction of ^{26}Al in the Galaxy. *Physical Review Letters*, 119(7):072701, August 2017.

[27] C. Angulo et al. A compilation of charged-particle induced thermonuclear reaction rates. *Nuclear Physics A*, 656:3–183, 1999.

[28] G. Lotay, P. J. Woods, D. Seweryniak, M. P. Carpenter, R. V. F. Janssens, and S. Zhu. γ-ray spectroscopy study of states in ^{27}Si relevant for the ^{26}Al$^m(p,\gamma)^{27}$Si reaction in novae and supernovae. *Physical Review C*, 80(5):055802, November 2009.

[29] C. M. Deibel et al. Toward an experimentally determined ^{26}Al$^m(p,\gamma)^{27}$Si reaction rate in ONe novae. *Phys. Rev. C*, 80:035806, Sep 2009.

[30] D.U. Visser. *Particle Decay Branching Ratios for States of Astrophysical Importance in ^{19}Ne*. PhD thesis, Yale University, 2003.

[31] John D. Fox Accelerator Lab. `http://fsunuc.physics.fsu.edu/`. Accessed August 2019.

[32] J.E. Spencer and H.A. Enge. Split-Pole Magnetic Spectrograph for Precision Nuclear Spectroscopy. *Nuc. Instr. Meth.*, 49:181–193, 1967.

[33] C.M. Deibel. Nuclear Astrophysics Prospects with the Yale Enge Splt-Pole Spectrograph at Florida State University. ARUNA Users Meeting, 2014.

[34] H.A. Enge. Magnetic spectrographs for nuclear reaction studies. *Nucl. Instr. Meth.*, 162(1):161 – 180, 1979.

[35] C.M. Deibel. *The ^{26m}Al$(p,\gamma)^{27}$Si Reaction Rate in ONe Novae*. PhD thesis, Yale University, 2008.

[36] Yale University. *Tedector User's Manual*, year unknown.

[37] R.G. Markham and R.G.H. Robertson. High resolution position-sensitive proportional counter. *Nucl. Instr. Meth.*, 129(1):131 – 140, 1975.

[38] Micron Semiconductor Ltd. 2018 catalogue, March 2018. Available at `http://www.micronsemiconductor.co.uk/wp-content/uploads/2018/03/2018-Micron-Semiconductor-Ltd-Silicon-Catalogue_Long-Form.pdf`.

[39] Micron Semiconductor, Ltd. personal communication.

[40] CAEN S.p.A. WP2081: Digital Pulse Processing in Nuclear Physics. White paper, CAEN Electronic Instrumentation, August 2011. Rev. 3.

[41] E. Koshchiy and others. ANASEN: The array for nuclear astrophysics and structure with exotic nuclei. *Nucl. Instrum. Meth. A*, 870:1–11, October 2017.

[42] B. Davin et al. LASSA: a large area silicon strip array for isotopic identification of charged particles. *Nuc. Instr. Meth. A*, 473:302–318, 2001.

[43] V.T. Jordanov and G.F. Knoll. Digital synthesis of pulse shapes in real time for high resolution radiation spectroscopy. *Nucl. Instr. Meth. Phys. Res. A*, 345(2):337 – 345, 1994.

[44] John Keightley, Christophe Bobin, Jacques Bouchard, Marco Capogni, Stefano Loreti, and Miguel Roteta. Recent advances in digital coincidence counting for Radionuclide Metrology. In *2013 3rd International Conference on Advancements in Nuclear Instrumentation, Measurement Methods and their Applications (ANIMMA)*, pages 1–7, Marseille, France, June 2013. IEEE.

[45] CAEN S.p.A. *UM2580: DPP-PSD: Digital Pulse Processing for Pulse Shape Discrimination*. CAEN Electronic Instrumentation, September 2016.

[46] CAEN S.p.A. GD2827: How to make coincidences with CAEN Digitizers. User guide, CAEN Electronic Instrumentation, March 2017. Rev. 3.

[47] D.R. Tilley, H.R. Weller, and C.M. Cheves. Energy levels of light nuclei A = 16-17. *Nuclear Physics A*, 564(1):1–183, November 1993.

[48] Rene Brun and Fons Rademakers. Root - an object oriented data analysis framework. *Nucl. Inst. & Meth. in Phys. Res. A*, 389:81–86, 1997.

[49] A.J. Ferguson. *Angular Correlation Methods in Gamma-Ray Spectroscopy*. John Wiley & Sons, Inc., 1965.

[50] S.L. Blatt, G.L. Marolt, and J.D. Goss. Widths of low-lying states of ^{13}N and the question of reaction dependence. *Phys. Rev. C*, October 1974.

[51] H.T. Fortune, T.J. Gray, W. Trost, and N.R. Fletcher. Reaction ^{12}C(^{3}He, d)^{13}N and stripping to unbound states. *Physical Review*, March 1969.

[52] M.B. Chadwick and P.G. Young. In *Proc.Int. Particle Therapy Mtg. and PTCOG XXIV*, Detroit, MI, April 1996.

[53] Takashi Fujisawa, Shuhei Yamaji, Kazuhisa Matsuda, Shoshichi Motonaga, Fusako Yoshida, Harutaka Sakaguchi, and Kuniaki Masui.

[54] Haixia An and Chonghai Cai. Global deuteron optical model potential for the energy range up to 183 MeV. *Phys. Rev. C*, 73:054605, May 2006.

[55] F. D. Becchetti and G. W. Greenlees. Nucleon-Nucleus Optical-Model Parameters, $A > 40$, $E < 50$ MeV. *Phys. Rev.*, 182:1190–1209, Jun 1969.

[56] D. Y. Pang, W. M. Dean, and A. M. Mukhamedzhanov. Optical model potential of $A = 3$ projectiles for $1p$-shell nuclei. *Phys. Rev. C*, 91:024611, Feb 2015.

[57] Y. Zhang, D. Y. Pang, and J. L. Lou. Optical model potential for deuteron elastic scattering with $1p$-shell nuclei. *Phys. Rev. C*, 94:014619, Jul 2016.

[58] R.J. Peterson and J.J. Hamill. Proton stripping to high spin states of ^{13}N. *Phys. Rev. C*, 22(6):2282–2286, 1980.

[59] R. Longland, C. Iliadis, A.E. Champagne, J.R. Newton, C. Ugalde, A. Coc, and R. Fitzgerald. Charged-Particle Thermonuclear Reaction Rates: I. Monte Carlo Method and Statistical Distributions. *arxiv*, 2010.

Vita

Erin was born in the bustling city of Harrisburg, Pennsylvania before the turn of the 21st century, and decided to attend LSU for graduate school after a very cold winter (think polar vortex). Her research interests include smashing nuclei together to see what happens, exploding stars, and breaking expensive experimental equipment. She hopes to continue studying two of these things in the future and to permanently cease the third.